UNIVERSITY OF OKLAHOMA

GRADUATE COLLEGE

ASSESSING IMPACTS OF PRECIPITATION AND PARAMETER UNCERTAINTY ON DISTRIBUTED HYDROLOGIC MODELING

A DISSERTATION

SUBMITTED TO THE GRADUATE FACULTY

in partial fulfillment of the requirements for the

Degree of

DOCTOR OF PHILOSOPHY

By

JONATHAN PAUL LOOPER

Norman, Oklahoma

2013

ASSESSING IMPACTS OF PRECIPITATION AND PARAMETER UNCERTAINTY ON DISTRIBUTED HYDROLOGIC MODELING

A DISSERTATION APPROVED FOR THE
SCHOOL OF CIVIL ENGINEERING AND ENVIRONMENTAL SCIENCE

BY

Dr. Baxter Vieux, Chair

Dr. Randall Kolar

Dr. Tohren Kibbey

Dr. S. Lakshmivarahan

Dr. K. Muraleetharan

For Sarah and Mason

Acknowledgements

This dissertation has grown out of the challenging problems that I have worked on both at the University of Oklahoma and at Vieux and Associates. The unique environment of academic and practical work experience has been rewarding and challenging. I am indebted and grateful to my friends at both places that have shaped my career, and allowed me to follow my intuition. The dual roles of teaching others and engaging in solving complex problems encountered during these last few years has been a fulfilling experience.

Many times we do not know the path our lives will take. However, one important moment was when I asked Dr. Strevett if he knew of any research jobs that would be available for an undergraduate. He introduced me to Drs. Vieux and Kolar who fortunately had funds available through the Undergraduate Research Opportunities Program. Over the next two years I was able to get my first taste of engineering research.

When I decided to return to graduate school I was only vaguely aware of the problems in hydrologic prediction. However, the practical challenges we have tackled at Vieux and Associates focused my research on precipitation uncertainty and parameter estimation. Dr. Vieux and Jean Vieux have provided me with so much over the years that has allowed me to follow my dreams. The enthusiasm they both have for helping others thru the application of engineering has been an inspiration.

I would also like to thank Drs. Kolar and Lakshmivarahan for the rigorous approach they have for solving complex problems. My first research experience

with Dr. Kolar showed me the excitement of research. His Water Resources Engineering course was the most challenging and exciting course I took as an undergraduate. As a graduate student, Dr. Lakshmivarahan's Scientific Computing 1 and 2 opened the world of applied linear algebra to me. The grand scope of these courses taught me how I could both build mathematical models and further enhance the predictive ability of these models thru data assimilation. Dr. Muraleetharan's advanced finite element course provided me with a deep understanding of this powerful technique for solving partial differential equations. I also greatly appreciate Dr. Kibbey's willingness to serve on my committee, and providing me with thoughtful comments that have shaped my dissertation.

There are far too many people that have helped me reach this point in my life. However, two that are especially dear to me are Sarah and Mason.They have provided both the support and fulfillment at crucial moments during this last part of my dissertation research. I know they have both sacrificed many Saturdays for me to complete this work. Last, I would like to thank my father for training me in mathematics from a young age. His support and encouragement helped me complete this dissertation.

Contents

List of Tables

List of Figures

Abstract

Distributed hydrologic models, based on conservation laws, simulate the flow of water over and through the land surface in response to forcing from precipitation, transpiration, and evaporation. Conservation laws provide a physical basis for runoff generation that are dependent on the accurate specification of initial conditions, boundary conditions, and representative parameter estimates which control the model's performance. The main objective of this dissertation is to develop and test a method for calibration of a distributed hydrologic model in the presence of rainfall input uncertainty that utilizes the physics of runoff generation processes.

The main hypothesis tested is that a model calibrated using spatially distributed (SD) parameter adjustments will have less prediction error than a model calibrated by a spatially averaged (SA) parameter adjustment. A Mann Whitney Wilcoxon (MWW) rank sum hypothesis test is used to test the statistical significance. The results of the MWW rank sum hypothesis test show the mean of RMSE from the model calibrated by SD adjustments is less than the RMSE from the model calibrated using the SA parameter adjustment. The Nash Sutcliffe Efficiency of the SD calibrated model is also consistently higher than the SA calibrated model. These results are consistent at both the calibration gauge and at the interior gauge point. Thus, a spatially distributed parameter adjustment technique leads to a reduction in prediction error compared with the spatially averaged parameter adjustment technique.

Chapter 1

Introduction

1.1 Motivation

Operational hydrologic predictions are required for the issuance of flood warnings and making operational decisions regarding reservoir storage. However, many basins are ungauged due to the cost of implementing and maintaining high-resolution hydrologic monitoring networks. Therefore, remote sensing and computer simulation to estimate hydrologic processes is an attractive alternative when direct measurement is not feasible. Understanding the level of detail required to characterize hydrologic processes has the potential to increase the predictability of streamflow in ungauged basins.

Considerable attention has been focused recently on radar hydrology, and its quantitative application in hydrologic modeling. Offline evaluation of hydrologic model prediction accuracy using archival radar and/or gauge data is a necessary step for improving operational use in real-time forecasting. These evaluations also provide opportunities to investigate the predictability of distributed hydrologic models used for decision making. The combination of distributed hydrologic modeling with high-resolution rainfall input derived from radar and gauge observations, offers the potential for gaining insight into how prediction accuracy scales with drainage area. Of particular importance is an understanding of how corrections made to radar rainfall input affect uncer-

tainty in hydrologic predictions, and how it scales with drainage area.

A workshop on predictability and limits to predictability discussed the frameworks necessary to characterize predictability in hydrologic systems (NRC, 2002). Recommendations by the NRC are that predictive system should include:

1. The fundamental system dynamics and propagation of perturbations,
2. Adequate characterization of model states, and
3. Procedures for generating model output with expected evolution of model states.

These three grand challenges are fundamentally at the source of increasing hydrologic predictability. My dissertation and research has focused on smaller components of each of these challenges. My particular research has been influenced by the importance of using accurate precipitation input for distributed hydrologic modeling. In addition, I have investigated the calibration of distributed hydrologic models and the impacts of precipitation bias on parameter estimation.

The objective of this dissertation is to develop and test a method for calibration of a distributed hydrologic model in the presence of rainfall input uncertainty that utilized the physics of runoff generation processes. Secondary objectives are:

1. Assess the influence of rainfall uncertainty on parameter estimation,
2. Develop a technique for propagating bias correction in rainfall through the model, and

3. Demonstrate that the Forward Sensitivity Method is capable of estimating spatially distributed parameters for a basin possessing heterogeneous model parameter spatial distributions.

1.2 Approach

The first objective is the characterization of rainfall to adequately simulate the hydrologic cycle (Ch. 3 and 4). The third chapter focuses on the impact of precipitation bias on the calibration of a distributed hydrologic model (Looper et al., 2012). The fourth chapter evaluates the impact of rain gauge adjustment on the operational performance of a distributed flash flood forecasting system (Looper and Vieux, 2012). My second objective is to develop a framework for propagating bias correction in radar rainfall through a distributed hydrologic model (Looper and Vieux, 2013). The third objective is to develop a technique that produces the expected evolution of a distributed hydrologic model using the Forward Sensitivity Method data assimilation technique (Lakshmivarahan and Lewis, 2010). This technique provides an evolution of forward sensitivities that addresses the dynamics and evolution of the sensitivities in time. In addition, the method provides an automatic calibration technique based on these sensitivities that can be used for parameter estimation.

The hypothesis is that a model calibrated using spatially distributed parameter adjustments will have less prediction error than a model calibrated by a spatially averaged parameter adjustment. The FSM method will be used to test for each case.

Chapter 2

Literature Review

This chapter focuses on the sources of uncertainty in distributed hydrologic modeling and the methods used to assess uncertainty.

2.1 Distributed Hydrologic Modeling

Whether lumped or distributed, watershed models are simplifications of complex processes responsible for runoff generation and routing, and may deviate from observed conditions. Distributed hydrologic modeling seeks to represent the spatially variable characteristics that control hydrologic response to forcing from precipitation and potential evapotranspiration. Physics-based distributed (PBD) hydrologic models generate runoff for each grid location and rely on the solution of the governing equations of conservation of mass and momentum to route runoff through a discrete representation of the watershed composed of channel and overland flow elements. Most PBD watershed hydrologic models solve a simplified flow analogy such as the kinematic or diffusive wave, rather than the full dynamic wave. Advances in computing and numerical methods such as the finite element method have led to the efficient mathematical representation of large areas at high resolution. The finite element approach is used by *r.water.fea* described by Vieux and Gauer (1994), and in V*flo* presented by Vieux et al. (2004a,b) and Vieux (2004a,b). Other PBD models that solve conservation equations include the CASC2D

(Julien and Saghafian, 1991; Ogden and Julien 1994); the GSSHA gridded diffusive wave model (Downer and Ogden, 2004); Systme Hydrologique Europen (SHE) (Abbott et al., 1986a;b); the Hydrologic Laboratory Research Distributed Model (HLRDM) participating in the DMIP and DMIP2 experiments (Koren et al., 2004); and the Distributed Hydrology Soil Vegetation Model (DHSVM) (Wigmosta et al., 1994). Of these PBD models, V*flo* and r.water.fea use the finite element method for spatial discretization of the watershed and solution of conservation equations.

Fully distributed models build the hydrologic response from the assembly of elements or grids representing the hydraulic drainage network, soils, imperviousness, and vegetative cover of the watershed. Digital terrain data describing overland slope and drainage direction commonly exists as gridded data, thus it is convenient to define the drainage network using a grid-cell scheme to connect overland flow and channel elements. The connectivity of the drainage network results in a system of equations that represent conservation of mass in the kinematic wave analogy (Vieux, 2004b). Coupling soil moisture tracking with the overland and channel components in V*flo* results in a distributed modeling system that is capable of continuous operation for online forecasting or offline hydrologic analysis.

Operational use of gridded PBD models for flood forecasting is a relatively recent development (Bedient et al., 2003; Vieux et al., 2003a; Todini, 1999). The NWS has expanded its efforts in distributed modeling with the HLRDM model, which is in use in the NWS Arkansas Red River Basin River Forecast and West Gulf River Forecast centers (Koren, 2004). To reduce manual adjustment of the Sacramento Model, a variational (VAR) approach is being tested that adjusts the ordinates of the unit hydrographs and input during operations

to force the simulated streamflow to match with the observed streamflow (Seo et al., 2003). Adjusting model input during operations may make it difficult to assess model performance independent of input uncertainty. A continuous model tracks soil moisture, providing proper initiation during real-time operations. Sensitivity to soil moisture can be larger than uncertainty due to uncalibrated radar estimates of precipitation, as shown by Vieux et al. (2009) where the model response is nonlinear and depends on storm magnitude. Uncertainties resulting from model input, parameters, and structure can confound streamflow simulation in both historical and operational forecast contexts.

2.2 Precipitation Uncertainty

Uncertainties in radar rainfall estimates used as input to hydrologic models can affect the accuracy of both offline prediction (post-analysis) and online forecast (real-time) applications, as observed by Carpenter and Georgakakos (2004) who considered ensemble streamflow forecasting in larger river basins where presumably there is less control over the radar bias and sparse rain gauge networks. The uncertainty inherent in precipitation derived from radar has been well established as having both random and systematic (bias) components, as described by Wilson and Brandes (1979), Doviak and Zrnic (1993) among others. It is also supposed that random error in the radar rainfall estimates, e.g. those caused by updrafts and downdrafts, should cancel out over catchment areas of sufficient size. Disparities in the representativeness of measurements of each sensor can cause disagreement between rainfall measurements made by gauges and radar, as found by Ciach et al. (2003, 2006), Chumchean et al. (2003), and Habib et al. (2004). Mandapaka et al. (2009)

estimated the spatial correlation distance to be about 20 km, which can increase uncertainty in rainfall estimates derived from combinations of gauge and radar. Effort expended on error separation to account for differences between rain gauge and radar measurements is important for understanding why observations from these sensors differ and where these errors come from. Beyond the uncertainty in point-area rainfall estimation, from a hydrologic perspective, understanding is needed on how these errors feed forward into hydrologic prediction and forecasting, whether they average out, or if there is scale dependency across catchment areas.

Conversion of reflectivity to rainfall rate is accomplished using a Z-R relationship that depends on the number and size of raindrops (Marshall and Palmer, 1948). However, among the many sources of uncertainty, error can be introduced due to differences between the assumed drop size distribution (DSD) in a given Z-R relationship and the actual storm DSD. Considerable reduction in radar rainfall uncertainty can be achieved through bias correction using rain gauges (Wilson and Brandes, 1979). The factors affecting radar rainfall accuracy, and the improvement achieved through bias correction using rain gauges are described by Chumchean et al. (2003), Morin et al. (1995), Rosenfeld et al. (1993, 1994), Smith et al. (1996), Seo et al. (1999), Sanchez-Diezma, et al. (2001), and Vieux and Vieux (2005a, 2005b).

Interest in characterizing radar adjustment techniques has accelerated with the advent of distributed hydrologic models that are capable of integrating the spatially distributed rainfall information (Gourley and Vieux, 2005, Habib et al., 2008). Use of gauge-adjusted weather radar for hydraulic modeling of sewer systems is becoming well established (Einfalt et al., 2005). An overview of the hydrologic requirements for weather radar used in urban drainage is

described by Einfalt et al. (2004), who identified the radar processing requirements for hydrologic applications of various weather radar systems in Germany and the United States. Vieux and Bedient (2004a) demonstrated the importance of gauge-correction of radar, and the achievable streamflow accuracy of distributed model predictions. In spite of point-area errors, it was found that gauge-corrected radar rainfall produced rainfall (input) agreed with measured streamflow (output) with a correlation coefficient of 0.94 for a single basin outlet location, i.e. the USGS stream gauge 08075000 in Brays Bayou, whereas, uncorrected radar produced much poorer agreement with streamflow. Even with high quality bias-corrected radar rainfall and a well characterized basin, uncertainty in the rainfall estimates can still persist and create prediction error. Looper et al. (2012a) performed a 10 yr continuous analysis of the impact of gauge adjustment on radar rainfall estimates. As a participating model in the second Distributed Model Intercomparison Project (DMIP2), V*flo* was applied to the Illinois and Blue River basins in Oklahoma. Streamflow prediction accuracy was enhanced when multi-sensor precipitation estimates (MPE) were bias corrected through re-analysis of the MPE provided in the DMIP2 experiment, resulting in gauge corrected precipitation estimates (GCPE). The reanalysis of rainfall input was one of the largest reasons for improved streamflow prediction accuracy.

Hydrologic prediction requires precipitation that is accurate and representative for the watershed area. While the method of adjustment depends on the hydrologic application and the spatial extent of the area of interest, the mean field bias (MFB) approach is useful for identifying gauges that are not consistent with the radar using a spatially constant adjustment factor and also reducing the single rain gauge error from corrupting the bias correction (Bedi-

ent et al. ,2008). The Local Bias (LB) approach to adjusting the radar rainfall applies a spatially-variable ratio of gauge to radar accumulations (G/R) from surrounding gauges with the closest gauge having the most weight (Seo and Breidenbach, 2002). The LB approach used here distributes the variation of bias over the area based on a 6-hour moving window that is updated every 15-minutes. The 6-hr moving window is an integration period updated every 15 minutes, which is similar to the window probability matching method (Rosenfeld, 1994). The LB uses the ratio between the sum of each gauge divided by the sum of the sampled radar values over each gauge. Gauge and radar accumulations were computed for each moving window. All radar/gauge (RG) pairs were then checked for statistical outliers. Exclusion of any gauge accumulation during a moving window is based on control limits of two standard deviations from the mean. After exclusion, remaining RG pairs are then distributed spatially over the analysis area using a Barnes objective analysis scheme (Barnes, 1964). The resulting LB value over each radar bin is the multiplicative factor that adjusts the radar. The Barnes objective analysis scheme is also used to perform the spatial interpolate the rain gauge data for the rain gauge only (RGO) input.

The rain gauge network density is important for characterizing rainfall variability alone or in conjunction with radar. Collier (1986) recommended a rain gauge spacing of 20 km to produce results as accurate as radar in Northwest England for all precipitation types, e.g. frontal, showers, and bright-band affected storms. Since then, many researchers and practitioners have employed rain gauge networks for validation of the quantitative precipitation estimates, evaluated inaccuracies in GARR on flood forecasting, and identified improvements needed for uniform reliability of rainfall measurements.

Errors in precipitation estimates derived from radar can lead to inaccurate stream flow predictions and miscalibration of hydrologic models (Winchell et al., 1998). To overcome this inaccuracy in post-event analysis, Bouilloud et al. (2010) developed an effective Z-R relationship through optimization using rain gauges to identify coefficients that minimized event-scale rainfall measurement differences. They found that an effective Z-R relationship could be optimized with respect to rain gauge accumulations measured at the event time scale, and that this approach could compensate for range dependent errors associated with radar. Coefficients of the Z-R relationship can vary significantly over time and space. Continuous updating of spatially variable radar bias correction factors is important for radar-based flood forecasting, especially where local downdrafts during storms can enhance rainfall rates that would otherwise go undetected by radar (Smith et al., 2007). Looper and Vieux (2012b) investigated the influence of rain gauge adjustment on the performance of a flash flood forecasting system for a significant flood event in Austin, TX. The distributed hydrologic model, V*flo*, was used for the study. A comparison of model forecast accuracy using the operational rain gauge-adjusted radar rainfall input (GARR) was made against rain gauge only (RGO) input. The use of GARR as input to the model not only increased the forecast lead-time accuracy, but also the accuracy of forecast peak stage across a range of basin sizes and with variable rain gauge densities used for radar bias correction. Rain gauge density over the forecast basins was one of the main determinants of forecast accuracy during the event. Input uncertainty can greatly affect the predictability of distributed hydrologic models. Looper (2012c) showed how rainfall input uncertainty propagated through a distributed hydrologic model. Identification of streamflow prediction accuracy using radar as input

to a distributed hydrologic model for a relatively impervious basin was performed using corrected and uncorrected radar input. Streamflow predictions are found to depend on: 1) the gauge correction of the radar-derived QPE; and 2) the non-linear scaling of gauge-correction with watershed area. Rainfall input was perturbed based on the PDF of bias correction factors for each event showing how gauge correction scales with drainage area. Across storm events, the difference between flow rates produced with corrected and uncorrected radar input consistently increased with drainage area, but at non-constant rates. The perturbation of inputs was used to confirm results obtained through comparison of forecast skill at two stream gauge locations. The model skill improved 3-fold when gauge-corrected radar is used over predictions obtained with the use of uncorrected radar. However, the technique requires a moving 6hr window to adjust the rainfall input. One hypothesis is that the data assimilation could be used to refine the Z-R relationship parameters. Using a data assimilation technique would lead to improved rainfall input estimates. The Z-R relationship parameters could be estimated using either the variational or ensemble Kalman filter approaches. A more robust picture of how input errors propagate through a distributed hydrologic model could be obtained by including the Z-R parameter estimation problem with the estimation of model parameters.

2.3 Parameter Estimation

Parameter estimation in distributed hydrologic modeling has been distinguished by methods that focus on the model either as a black box or uses the physical model structure to speed up model parameter estimation. Duan (1992) pro-

posed a framework for optimization of a hydrologic model called the Shuffled Complex Evolution (SCE) method. Duan identified five points concerning the optimization problem. This method assumes the model is a black box and can be slow to converge.

1. There may be several major regions of attraction into which a search strategy may converge.

2. Each major region of attraction may contain numerous (possibly uncountable) local minima (stationary points where the first derivatives are zero and the Hessian matrices are positive definite or positive semi definite). These local optima may occur both close to and at various distances from the best solution.

3. The objective function surface in the multi-parameter space may not be smooth and may not even be continuous. The derivatives may be discontinuous and may vary in an unpredictable manner through the parameter space.

4. The parameters may exhibit varying degrees of sensitivity and a great deal of interaction and compensation. Much of the interaction can be highly nonlinear.

5. The response surface near the true solution is often non-convex.

The ordered physics based parameter adjustment (OPPA) framework (Vieux and Moreda, 2003) is a guided calibration process for PBD models. The OPPA approach optimizes runoff volume parameters followed by the optimization of overland and channel hydraulic parameters. The OPPA method focuses first

on the parameters that influence runoff volume. The main parameters controlling runoff volume in V*flo* are soil depth and assumed porosity, and saturated hydraulic conductivity. Adjusting these parameters simultaneously includes both saturation excess and infiltration rate excess runoff-generating processes of the basin. The main steps in the OPPA method are:

1. Estimate spatially distributed parameters from physical properties.
2. Assign channel hydraulic properties based on measured cross-sections where available.
3. Study the sensitivity of each parameter
4. Determine the optimum parameter set, which minimizes the respective objective functions for runoff volume, timing, and peak discharge.
5. Perform continuous and event based simulations then re-adjust parameters to account for interactions as necessary.

Spatially uniform scalar multipliers adjust a-priori distributed parameter estimates derived from soil and channel parameters with the objective of minimizing a function composed of the differences between observed and simulated quantities, e.g. volume, peak stage, and timing.

Uncertainty estimation within the hydrologic community has been divided into less formal and more formal mathematical frameworks for uncertainty estimation. The less formal methods such Propagation of Perturbations and Generalized Likelihood Uncertainty Estimation (GLUE) have been derived out of generally only hydrologic concerns. Formal methods based on filtering theory have been derived based on a strict mathematical framework and then applied to hydrologic problems.

Wagener (2004) developed a simplified framework for assessing the sensitivity of model parameters using simple conceptual models. The framework uses Monte Carlo simulations with simple conceptual models to identify parameters that are critical to predictability. The lack of identifiably of model structure and parameters is a major restriction of current conceptual rainfall runoff models (RRM) applications. It introduces large uncertainties into model predictions and seriously limits the possibility of sensible parameter regionalization for the modeling of ungauged catchments. Beven and Binley (1992) developed a Monte Carlo technique to try and handle the cases where multiple parameter sets can generate generally acceptable results. A basic underpinning of the method is that we cannot assume we know exactly the model structure of a system. The method weights each model structure based on a likelihood function derived from how well each model performed during calibration.

Data Assimilation is the optimal combining of data and models to minimize a defined criterion. It can be divided into stochastic and deterministic techniques. Stochastic data assimilation has grown out of the linear Kalman Filter (Kalman, 1960) approach to combining observations and simulations. The Kalman Filter is a method of optimally combining a linear model with observations. It finds the state variables of a linear model that minimizes the analysis error covariance matrix. The Kalman Filter approach was extended to non-linear models using the Extended Kalman Filter (EKF). The EKF requires creating the tangent linear model around the mean of the state variables. The linearization is performed by using the first term of a Taylor's series expansion around the mean of the state variables. The inverse of the linearization is the adjoint which is used to propagate variations backwards in time. Higher order

non-linear filters can be derived by including more terms from the Taylor's series expansion. Another approach to linearizing the model is the Ensemble Kalman Filter with perturbed observations (EnKF). The EnKF uses an ensemble of model simulations to estimate the background error covariance matrix within the Kalman Filter. The background error covariance matrix is estimated from the ensembles. Perturbations are added to the observations and then each perturbed observation is used to calculate the analysis state variable. The perturbations are required due to spurious correlations due to small ensemble sizes. As the ensemble size increases to infinity the analysis covariance converges to the true variance (Evensen, 1994).

An alternative approach is the Local Ensemble Transform Kalman Filter (LETKF) data assimilation framework (Hunt, 2007). The LETKF data assimilation framework constrains the Kalman gain to a localized area. Covariance localization could help to alleviate the sampling error by restricting the influence of grids that are located a distance from the grid of interest (Houtekamer and Mitchell, 2001). This in turn reduces the complexity of the Kalman gain calculation. Usually the correlation structure is assumed, but for real cases this error correlation structure is seldom known. There has been little work in how to define the localized areas within distributed hydrologic modeling.

Deterministic data assimilation are usually based on the variational approach to combining data and models. Castaings et al. (2009) showed that error covariance matrix structure is related to the drainage network configuration. Thus if an initial estimate of the drainage network structure is well defined then the parameter estimated by data assimilation will be easier to find. He however used a simple model structure that did not take into account saturation excess runoff processes. The on/off switching behavior of runoff

generation can be problematic in calculating the adjoint model. He used automatic differentiation (AD) techniques that may need to be modified to handle discontinuities.

The 4D-Var technique has been used extensively in meteorology (LeDimet and Talagrand, 1986). One new deterministic method for data assimilation is the Forward Sensitivity Method (FSM) (Lakshmivarahan and Lewis, 2010). The FSM has been shown to be equivalent to the 4D-Var technique. However, FSM provides additional information about the impact of the time of each observation on the prediction error structure.

Comparing ENKF assimilation and 4D-Var approaches is necessary since hybrid techniques combining both methods have become attractive in Meteorology (Buehner et. al, 2009). A hybrid approach combining both methods uses the ENKF to calculate the background error covariance required for variational assimilation. This avoids the calculation of the linear model and adjoint usually required for variational assimilation. This hybrid technique would also be useful transition from infiltration rate excess to saturation excess runoff processes. This transition usually causes the adjoint to become unstable due to filling the soil profile.

Increasing prediction accuracy through incorporation of observations is important for a variety of hydrologic forecasting applications, e.g. streamflow, drought, flood, water supply, etc. The two general methods of deterministic and stochastic filtering (Lewis et al., 2006) have enhanced the application of strict mathematical frameworks for data assimilation.

Chapter 3

Assessing the Impacts of Precipitation Bias on Distributed Hydrologic Model Calibration and Prediction Accuracy

3.1 Abstract

[1] Physics-based distributed (PBD) hydrologic models predict runoff throughout a basin using the laws of conservation of mass and momentum, and benefit from more accurate and representative precipitation input. V*flo* is a gridded distributed hydrologic model that predicts runoff and continuously updates soil moisture. As a participating model in the second Distributed Model Intercomparison Project (DMIP2), V*flo* is applied to the Illinois and Blue River basins in Oklahoma. Model parameters are derived from geospatial data for initial setup, and then adjusted to reproduce the observed flow under continuous time-series simulations and on an event basis. Simulation results demonstrate that certain runoff events are governed by saturation excess, while in others, infiltration rate excess dominates. Streamflow prediction accuracy is enhanced when multi-sensor precipitation estimates (MPE) are bias corrected through re-analysis of the MPE provided in the DMIP2 experiment, resulting in gauge corrected precipitation estimates (GCPE). Model calibration identi-

[1] Adapted version of Looper, J. P., Vieux, B. E., and Moreno, M. A. (2012). Assessing the Impacts of Precipitation Bias on Distributed Hydrologic Model Calibration and Prediction Accuracy. *Journal of Hydrology*, 418, 110-122.

fied a set of parameters that minimized objective functions for errors in runoff volume and instantaneous discharge. Simulated streamflow for the Blue and Illinois River basins, has Nash-Sutcliffe efficiency coefficients between 0.61 and 0.68 respectively for the 1996–2002 periods using GCPE. The streamflow prediction accuracy improves by 74 percent in terms of Nash Sutcliffe efficiency when GCPE is used during the calibration period. Without model calibration, excellent agreement between hourly simulated and observed discharge is obtained for the Illinois, whereas in the Blue River, adjustment of parameters affecting both saturation and infiltration rate excess were necessary. During the 1996–2002 period, GCPE input was more important than model calibration for the Blue River, while model calibration proved more important for the Illinois River. Calibration proved more important than using GCPE input during the 2002–2006 in both the Blue and Illinois River basins.

3.2 Introduction

Uncertainties resulting from model input, parameters, and structure can confound streamflow simulation in both historical and operational forecast contexts. Whether lumped or distributed, watershed models are simplifications of complex processes responsible for runoff generation and routing, and may deviate from observed conditions. Distributed hydrologic modeling seeks to represent the spatially variable characteristics that control hydrologic response to forcing from precipitation and potential evapotranspiration. Among other objectives, the DMIP2 experiment explores distributed and lumped models performance, given the uncertainties in precipitation estimates used in river forecast operations. Further description of the NWS motivation for the DMIP2

experiment may be found in the overview paper (Smith et al., this issue).

Physics-based distributed (PBD) hydrologic models generate runoff for each grid location and rely on the solution of the governing equations of conservation of mass and momentum to route runoff through a discrete representation of the watershed composed of channel and overland flow elements. Most PBD watershed hydrologic models solve a simplified flow analogy such as the kinematic or diffusive wave, rather than the full dynamic wave. Advances in computing and numerical methods such as the finite element method have lead to the efficient mathematical representation of large areas at high resolution. The finite element approach is used by r.water.fea described by Vieux and Gauer (1994), and in V*flo* presented by Vieux et al. (2004a,b) and Vieux (2004a,b). Other PBD models that solve conservation equations include the CASC2D (Julien and Saghafian, 1991; Ogden and Julien 1994); the GSSHA gridded diffusive wave model (Downer and Ogden, 2004); Systme Hydrologique Europen (SHE) (Abbott et al., 1986a;b); the Hydrologic Laboratory Research Distributed Model (HLRDM) participating in the DMIP and DMIP2 experiments (Koren et al., 2004 and Smith et al. this issue); and the Distributed Hydrology Soil Vegetation Model (DHSVM) (Wigmosta et al., 1994). Of these PBD models, only V*flo* and *r.water.fea* use the finite element method for spatial discretization of the watershed and solution of conservation equations.

Fully distributed models build the hydrologic response from the assembly of elements or grids representing the hydraulic drainage network, soils, imperviousness, and vegetative cover of the watershed. Digital terrain data describing overland slope and drainage direction commonly exists as gridded data, thus it is convenient to define the drainage network using a grid-cell scheme to

connect overland flow and channel elements. The connectivity of the drainage network results in a system of equations that represent conservation of mass in the kinematic wave analogy. Coupling soil moisture tracking with the overland and channel components in V*flo* results in a distributed modeling system that is capable of continuous operation for online forecasting or offline hydrologic analysis.

Operational use of gridded PBD models for flood forecasting is a relatively recent development (Bedient et al., 2003; Vieux et al., 2003a; Todini, 1999). The NWS has expanded its efforts in distributed modeling with the HLRDM model, which is in use in the NWS Arkansas Red River Basin River Forecast and West Gulf River Forecast centers (Koren, 2004). To reduce manual adjustment of the Sacramento Model, a variational (VAR) approach is being tested that adjusts the ordinates of the unit hydrographs and input during operations to force the simulated streamflow to match with the observed streamflow (Seo et al., 2003). Adjusting model input during operations may make it difficult to assess model performance independent of input uncertainty. A continuous model tracks soil moisture, providing proper initiation during real-time operations. Sensitivity to soil moisture can be larger than uncertainty due to uncalibrated radar estimates of precipitation, as shown by Vieux et al. (2009) where the model response is nonlinear and depends on storm magnitude. Vieux et al. (2002) presents continuous V*flo* simulation of watershed response and soil moisture for three watersheds that include the island of Puerto Rico, a coastal watershed near Houston, Texas, and a partially urbanized watershed in Norman, Oklahoma. Current uses of V*flo* for continuous operations include the Flood Alert System (FAS) in Houston, Texas, (Bedient et al., 2003); distributed hydrologic monitoring for the Oklahoma Department of Trans-

portation where 149 bridges subject to scour are simulated; modeling for the City of Austin, Texas (Janek et al., 2006) in urban and rural basins prone to flash flooding; monitoring for the US National Weather Service in the OUN Forecast Office; and flood forecasting applications internationally (Vieux et al., 2003).

Understanding the source of uncertainty in historical simulations is important for improving the accuracy of real-time forecasts as well as offline model simulations. Real-time forecasts may use precipitation input that are biased due to an inappropriate Z-R relationship or a lack of reporting rain gauges. This differs from offline model simulations where the Z-R relationship can be adjusted and rain gauge data is more complete. Oudin (2006) showed that random errors in precipitation significantly decreased model performance. He also indicated that model parameters can be over calibrated to adjust for these errors in precipitation inputs. Prediction uncertainty may be due to model structure, parameter uncertainty, soil moisture, or precipitation inputs, any of which may confound efforts to identify physically realistic parameter values that are stable during seasonal or interannual periods. Our purpose is to: 1) participate in the DMIP2 experiment using a physics-based distributed model, 2) evaluate the model's sensitivity to input forcing, and 3) identify physically realistic parameters that are stable. Section 2 offers an overview of the Blue and Illinois River basins. Section 3 presents the theoretical physical laws for V*flo*. Section 4 describes the datasets and steps required to parametrize the model. Section 5 describes the DMIP2 experimental precipitation (MPE) and the gauge corrected precipitation estimate (GCPE). Section 6 explains the distributed model calibration procedure. Section 7 presents the baseline uncalibrated and calibrated model results and sensitivity to model input forcing.

Finally, a summary and conclusions are presented in Section 8.

3.3 Basin Characteristics

In our study, we considered two of the basins in the DMIP2 experiment, which are the Blue River and Illinois River basins shown in Figure 3.1. Due to the frequent occurrence of severe weather in Oklahoma, there is a large amount of archival radar and rain gauge observational data. Since 1993, the US NWS Arkansas-Red Basin River Forecast Center (ABRFC) has archived precipitation estimates for the region including the Blue and Illinois River basins using a combination of NEXRAD (WSR-88D) radars and rain gauge observations. The observational networks of radars, Mesonet rain gauges, and stream gauges that cover the Blue and Illinois basins are shown in Figure 3.2.

For the Blue River basin, two USGS gauging stations have observed streamflow for different periods of record. The Oklahoma Mesonet maintains a network of meteorological stations within the state of Oklahoma (Brock et al., 1995) that are apparently used operationally by the ABRFC along with other US NWS precipitation gauges located within the Arkansas-Red River basin. Within and surrounding the Blue River, there are eight Oklahoma Mesonet rain gauges with an average spacing of 40 km. The Twin Lakes radar (KTLX) is located 80 km away from the upper portion of the Blue River basin and 200 km away from the outlet, which can result in radar beam overshooting of precipitation in the lower atmosphere over the southern portion (Gourley and Vieux, 2006).

For the Illinois River basin, there are nine USGS gauging stations providing observed streamflow, and eight Oklahoma Mesonet rain gauges with an average

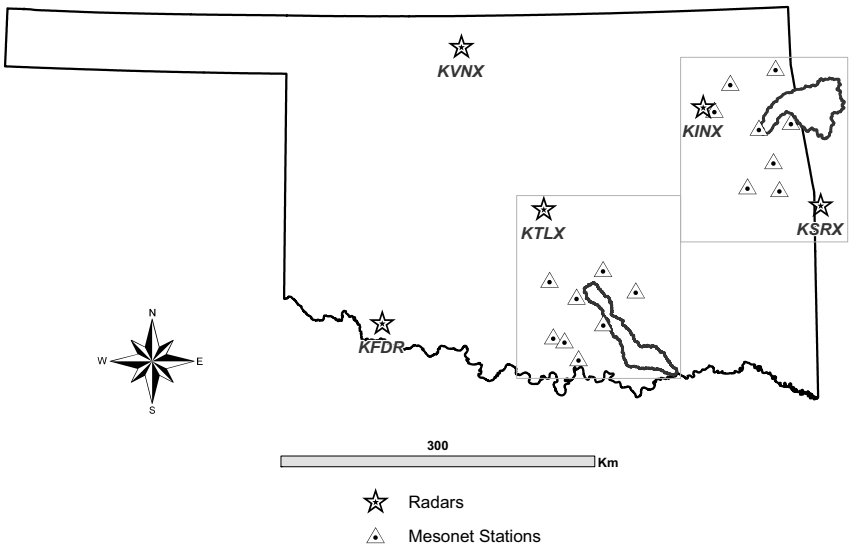

Figure 3.1: Study basin locations in relation to rain gauge and radar network observational networks

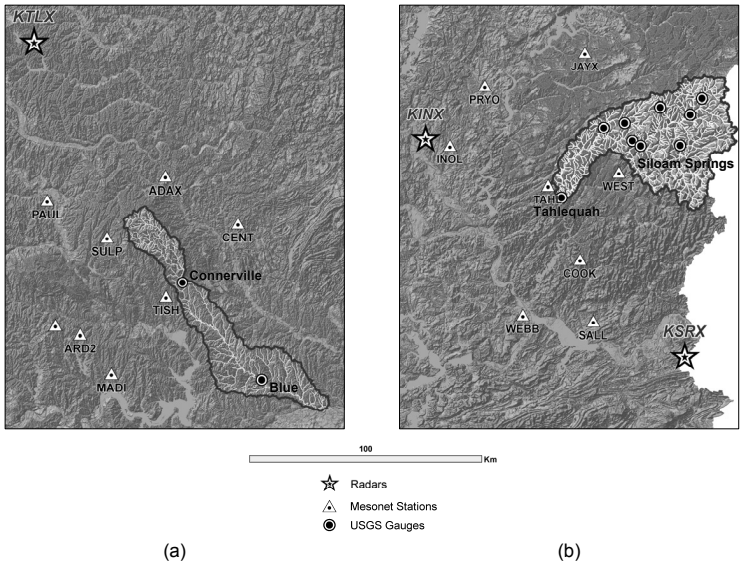

Figure 3.2: Basin locations and surrounding radar and rain gauge locations, and streamflow gauging stations for a) Blue River basin, and b) Illinois River basin

spacing of 30 km. Only three gauges are located near the basin and are distributed to the west of Tahlequah on the Oklahoma side of the border with Arkansas. The two radars covering the Illinois River basin are located in Tulsa, Oklahoma (KINX) and Fort Smith, Arkansas (KRSX). The KINX radar is located 63 km from the outlet and 130 km from the eastern portion of the Illinois River basin, and the KRSX radar is located 86 km from the outlet and 120 km from the northern side of the basin.

3.3.1 Blue River

The 1232 km^2 Blue River basin is located in south central Oklahoma and drains into the Red River that forms the border between Oklahoma and Texas (Figure 3.2a). Normal annual precipitation ranges between 972–1124 mm. Mean annual runoff generalized from climatological data ranges from 152–203 mm (Vieux et al., 2003b). In the Blue River, the mean annual evapotranspiration ranges from 762–822 mm based upon a simple water balance analysis (Garbrecht, 2004). The Arbuckle-Simpson aquifer underlies the upper Blue River basin, and contributes springflow to the local creeks and rivers. Baseflow upstream of Connerville is derived from the Arbuckle-Simpson aquifer. The aquifer has been the focus of an extensive study by the Oklahoma Water Resources Board (OWRB). Recharge in the upland areas of the Blue River affects runoff due to preferential flow through karsts. Subsequent discharge from the subsurface to the stream network may add additional complexity to the rainfall-runoff transformation. During the 2003–2006 period, average baseflow in the Blue River at Blue was 2.8 m^3/s; at Connerville the average baseflow was 1.5 m^3/s. The verification period, October 2002 to September 2006, was dominated by baseflow with only a few significant events that are less than

the 2-yr recurrence period.

The USDA-NRCS soil survey for Bryant County covers a portion of the Arbuckle-Simpson Aquifer. The survey identifies soil features that allow recharge to the aquifer. Soil series and rock outcrops prevalent above Connerville in the Blue River basin are the Talpa-Rock Outcrop and Lula-Talpa-Scullin association, which feature fractures or macropores allowing recharge. Rapid response of groundwater levels in this area during and immediately after rainfall, further supports the occurrence of recharge to the aquifer from exposed rock outcrops in the Blue River. However, not all rock outcrops communicate rainfall to the subsurface as recharge, such as those soils derived from granitic outcrops prevalent below Connerville in the Blue River. Hydrologic processes responsible for runoff generation including macroporosity and interflow are expected to be dominant processes in the upper reaches of the Blue River because of the connection between surface runoff, recharge, and baseflow.

3.3.2 Illinois River

The Illinois River basin is located in the Northeast portion of Oklahoma, and drains hilly terrain to Lake Tenkiller (Figure 3.2b). Forest and pasture are prevalent in areas with rock outcrops or rocky soils, whereas cropland is concentrated in the more fertile soil in the lowlands, floodplains, or flatter slopes in the watershed. The Illinois River typically receives measurable precipitation for 80–90 days annually, with 10–14 days of snow, on average. Normal annual precipitation ranges from 1066 to 1219 mm. Annual runoff for the East Central region of Oklahoma, where the Illinois River is located, ranges from 304–508 mm (Vieux and Moreda, 2003b). Average annual estimates of evapotranspiration range from 758–802 mm based on a simple water balance

analysis by Garbrecht (2004). Baseflow at Tahlequah is 28 m^3/s. At upstream locations dominated by springflow, baseflow represents a larger percentage of streamflow in the Illinois watershed.

3.4 Model Formulation

3.4.1 Runoff

V*flo* is a physics-based distributed hydrologic model that computes two state variables, soil moisture and direct runoff depth. Runoff generation and routing are an integrated continuous process modeled by the kinematic wave analogy applied to saturation and infiltration rate excess. The V*flo* model represents the watershed by means of a network of channel and overland flow grid cells connected by finite elements forming the drainage network. The kinematic wave analogy for overland and channel flow in this network is solved using the finite element method in space and finite difference in time (Vieux, 2004b). The fully turbulent Manning's equation is used to relate velocity to depth at each finite element node based on local land surface slope and hydraulic roughness (Vieux, et al., 1990). The flow depth, h, in each overland grid cell depends on runoff from upslope, infiltration, rainfall intensity, slope, and hydraulic roughness. The kinematic wave equation for overland flow in terms of depth, h, is,

$$\frac{\partial h}{\partial t} + \frac{S^{0.5}}{\eta}\frac{\partial h^{5/3}}{\partial x} = R - I \tag{3.1}$$

where S is the land surface slope, η is the Manning's roughness coefficient, R is rainfall rate, and I is infiltration rate. The dependent variable, h, is modified

depending on whether the flow is overland or within the confines of a channel.

3.4.2 Infiltration

Partitioning of precipitation into runoff and infiltration depends upon characterization of the soil and soil moisture conditions. The soil model applied here consists of a single layer with a restrictive boundary. Infiltration rate, I, is modeled using the Green and Ampt equation,

$$I = K_e \left[1 + \frac{\Psi_f \Delta\theta}{F(t)} \right] \tag{3.2}$$

where K_e is the effective saturated hydraulic conductivity; Ψ_f is the wetting front soil suction head; $\Delta\theta$ is the soil moisture deficit; and $F(t)$ is the cumulative infiltration depth. The Green and Ampt equation assumes a well-defined wetting front; therefore, the volume of infiltrated rainfall must be re-distributed as soil moisture after rainfall ceases. The model assumes that infiltrated water is redistributed on a daily basis so that the soil moisture deficit is uniform over the soil profile. Occurrence of rainfall in the radar QPE input superimposed over each grid cell is used to determine rain and non-rain periods. During periods of non-rain, evaporation is permitted subject to available soil moisture. A timeseries of climatological rates of potential evapotranspiration (PET) are input to the model. For each grid cell, the PET rate depletes the soil moisture until the wilting point is reached during non-rainfall periods. The available storage in the single layer soil model equals the effective porosity multiplied by the soil depth, which is accounted for in the $\Delta\theta$ term in (3.2). When the soil profile becomes saturated, rainfall becomes saturation excess runoff. The soil depth is a model constraint that provides a means

for simulating both infiltration-rate and saturation excess runoff processes to generate flow that is then routed downstream.

3.4.3 Streamflow Routing

Channel hydraulic representation and routing are important determinants of model prediction accuracy when applied to flood stage prediction in operational forecasting or historical simulation. Streamflow routing within the V*flo* model uses the kinematic wave analogy with lateral inflow,

$$\frac{\partial A}{\partial t} + \frac{\partial Q}{\partial x} = q \tag{3.3}$$

where Q is the discharge or flow rate in the channel; A is the wetted area of the cross section; and q is the rate of lateral inflow per unit length of the channel. The simplified momentum equation is used, where the friction gradient, S_f , is assumed to be parallel to the land surface or channel slope, So (Cunge, 1980). Solving for S_f using Mannings equation relating $Q = f(A)$ results in the first term in Eq. (6.1) as,

$$\frac{\partial A}{\partial t} = \frac{dA}{dQ}\frac{\partial Q}{\partial t} \tag{3.4}$$

The relationship $\frac{dQ}{dA}$ controls the speed of the flood wave through a channel cell and is defined by rating curves or by the channel cross section geometry. Channel cells are represented using trapezoids, surveyed cross-sections, or rating curves. The celerity of the kinematic wave depends on the flow rate and the geometry of the cross section, which poses a limit to explicit time-stepping algorithms used to solve the kinematic wave equations. Each channel grid is supplied with geometric information, bed slope, and a single roughness coef-

ficient representative of the entire cross-section. More complex hydraulics in channel and overbank areas such as floodplains may be modeled with rating curves imported from other hydraulic models.

3.4.4 Baseflow

Currently V*flo* does not have a baseflow component. For the upper portions of the Blue River basin this is an important component of the hydrologic system. To overcome these limitations, baseflow separation is performed on the observed hydrographs using USGS PART software (Rutledge, 1998). The PART program models aquifer discharge based on a master recession index derived from streamflow hydrographs during non-storm periods. After the direct runoff has been modeled using V*flo*, the baseflow component is added to the direct runoff hydrographs to produce the streamflow hydrograph. At interior ungauged points, baseflow is estimated as a fraction based on drainage areas and the closest downstream gauge where baseflow is recorded.

3.5 Model Parameterization

Distributed hydrologic models are parameterized using geospatial data sets representative of the basin; for example, hydraulic roughness parameters may be interpreted from land use/cover data. If the parameter estimates are uncertain, then some adjustment to the base estimate may be needed. Parameter estimation from watershed characteristics and predictable response to parameter adjustment are hallmarks of PBD models. Calibration is often required of any model because of imperfect knowledge of parameters or a model structure that does not accurately represent the watershed or runoff processes assumed

to be operating. The following sections describe the parameterization of infiltration processes and hydraulic routing within the V*flo* hydrologic model, which are setup at 500 and 250–m resolutions for the Blue and Illinois River basins, respectively. The Blue River comprises 4,926 cells while the Illinois has 20,265.

3.5.1 Infiltration

Use of the Green and Ampt model requires estimation of saturated hydraulic conductivity, wetting front suction, and effective porosity at each grid cell. The Green and Ampt soil parameter maps are determined from the Rawls and Brakenseik relationships developed for soil textural classifications (Rawls et al. 1983a, b). The soil textural classifications for the Blue River basin are obtained for this study from the Map Information Assembly and Display System (MIADS). MIADS is a soil database compiled at a 200-meter resolution by the United States Department of Agriculture (USDA)-Natural Resources Conservation Service (NRCS) for the State of Oklahoma from county-level soil surveys. Soil textural classifications for the Illinois River are obtained from the Soil Survey Geographic (SSURGO) soil database. The soil depth is derived using the depth to the bottom of the 'B' layer as an initial starting depth. Identifying the limiting layer (e.g. perched water table, bedrock) is important for continuous simulation of both saturation excess and infiltration rate excess runoff events. Soil depth and saturated hydraulic conductivity parameters are adjusted during model calibration.

3.5.2 Hydraulic Roughness

The overland flow is modeled using Manning's roughness, η interpreted from land use/cover maps of the watershed. For overland cells, roughness values are estimated using tabulated values reported by landuse type (Engman, 1986). Spatial datasets of landuse type are obtained from the National Land Cover Database (NLCD, 2001). Landuse classifications contained in the NLCD are then reclassified to maps of overland roughness coefficients using lookup tables based on Engman (1986). Channel cells are defined at locations in the watershed consistent with networks contained in the National Hydrography Dataset (NHD) GIS database. Roughness values for channel cells are estimated from lookup tables provided by Chow (1959), Barnes (1967), and from previous modeling studies (Vieux et al. 2004b).

Channel routing is affected by assumed cross-section geometry, slope, and roughness that control the wave velocity as it propagates downstream. Trapezoidal cross sections are assumed throughout except where surveyed cross-sections or rating curves are available. Trapezoidal channel bottom width is estimated from aerial photographs or surveyed cross sections. Rating curves provided by the USGS are used for gauged locations. The estimation of assumed trapezoidal channel properties at grid locations is accomplished by applying a geomorphic relationship between drainage area and the channel width. Drainage area is derived from the flow accumulation for selected locations. The channel width functions are $W(A) = 5.30A^{0.23}$ for the Blue River and $W(A) = 0.15A^{0.79}$ for the Illinois River (Figure 3.3 a, b) where, W is the channel bottom width in meters, and A is the drainage area in square kilometers. In the Illinois, the channel width is more sensitive to drainage

area: its exponent for drainage area is 0.79, whereas in the Blue River the exponent is only 0.23. Channel routing is relatively insensitive to channel side slope, and is assumed to be 1:1 vertical to horizontal throughout. Channel longitudinal slope is a smoothly varying parameter derived from topographic contours and is assigned to each grid in the channel network. Initial estimates of channel hydraulic roughness are provided from published values typical of channels within the two river basins (Vieux et al., 2004b). Other information on channel cross-sectional geometry is available in some locations for these two basins. Harmel (1997) established measured cross section data for the Illinois River basin for purposes of understanding aggradation and degradation of the channel. Selected cross-sectional information from Harmel (1997) was input to the Illinois River V*flo* model, particularly in the lower main channel reach from Watts to Tahlequah. Additional channel cross-sectional geometry in the form of width-height pairs was derived from an engineering study collected by Freeze and Nichols (1994), and provided as part of the DMIP experiment.

3.6 Hydrometeorological Inputs

Hydrologic prediction requires precipitation that is representative and accurate for the watershed area. Developments in radar technology have led to precipitation measurement that is high-resolution, both temporally and spatially. However, errors in precipitation estimates derived from radar can lead to inaccurate streamflow predictions and mis-calibration (Winchell et al., 1998). The initial use of MPE form model input and the use of gauge corrected precipitation estimates (GCPE) for input in re-analysis is described as follows.

3.6.1 Multi-sensor Precipitation Estimates

For the DMIP2 project, the organizers provided multi-sensor precipitation estimates (MPE). The MPE input is composed of a mosaic of Digital Precipitation Array (DPA), operational hourly rain gauge data, and forecaster adjustments (Fulton et al, 1998). The MPE used in this paper refers to the DMIP2 data supplied by the organizers. It does not refer to the NWS MPE system. The model input was calibrated using the MPE and then forced using the GCPE per the DMIP2 instructions. Young et al. (2000) documented inconsistencies in the MPE estimates, such as range dependent biases and bright banding. Additional sources of uncertainty in precipitation estimates include beam ducting, individual radar power differences, ground clutter, erroneously assumed drop size distributions, signal attenuation, overshooting cloud tops, and backscattering from hail (Doviak and Zrnic, 1993). Hail has considerably larger backscattering cross sections than water droplets, and leads to larger reflectivity values (Atlas et al., 1960). These larger reflectivity factors result in rainfall rate overestimates and can cause model over-prediction. In August 2002, an intense storm cell developed and passed over the Blue River basin near Wapanucka, Oklahoma; interpolated gauge data was used instead of radar in this event because hail was reported for the storm in the NCDC extreme storm event database. Another severe storm event within the MPE archive is October 1998, when an outbreak of 19 tornadoes and heavy precipitation showed possible hail contamination over the Illinois River basin. Even with gauge-correction, the effects of hail contamination may be difficult to remove or correct, and can lead to distortion of model parameters.

The MPE precipitation input is the primary data used as model input

in the DMIP2 experiment. The model simulations reported herein relied on MPE from the ABRFC and rain gauge data. Mesonet gauge data from the Oklahoma Mesonet is used to perform spatially-variable bias correction of the MPE input on a daily accumulation basis, referred to herein as gauge-corrected precipitation estimate (GCPE). While the NWS already performs bias correction, the resulting precipitation estimates may not be accurate for a particular river basin, such as the Blue River (1,232 km^2), because adjustment is performed on the entire Arkansas-Red River basin (538,717 km^2). The mean field bias correction over the ABRFC domain may not be appropriate to ensure the removal of bias near the subject basins. It should be noted that the area sampled by radar and rain gauges is significantly different. The MPE used in the study has an approximate pixel resolution of 4 km, while the standard rain gauge has a diameter of 20.3 cm. Both a local bias and mean field correction were tested, but for the rain gauge spacing near the subject basins, slightly better streamflow simulation results were obtained with mean-field bias correction. The GCPE uses a mean field bias correction factor, MFB, defined as,

$$MFB = \frac{\frac{1}{n}\sum_{i=1}^{n} G_i}{\frac{1}{n}\sum_{i=1}^{n} MPE_i} \tag{3.5}$$

where G_i and MPE_i are the ith gauge-MPE pairs of accumulation, respectively, and n is the number of pairs.

Figure 3.4 shows the MFB value from 1996 to 2006 for the Blue River basin. The daily MFB showed that there were periods with significant departures, but the central tendency of the MFB was 1.0. A comparison of hydrologic prediction results using GCPE and MPE is presented below in the results

section. The random error between radar and gauge rainfall accumulations is represented by the average difference, $\bar{D}$, defined as,

$$\bar{D} = \frac{100\%}{n} \sum_{i=1}^{n} \left| \frac{G_i - MPE_i}{MPE_i} \right| \tag{3.6}$$

where G is the observed gauge accumulation, MPE is the multi-sensor precipitation estimate, and n is the number of gauges with reporting data. For the Blue River basin, the average difference for MPE is 15.3%, while the average difference for GCPE is 12.9%. For the Illinois River basin, the average difference for MPE is 20.8%, while the average difference for GCPE is 15.8%. Through re-analysis, the average difference between rain gauge and radar estimates improves 2.4% and 5.0% for the Blue and Illinois River basins, respectively. While this enhancement in accuracy does not appear to be large, its impact on streamflow prediction accuracy proves to be significant, as shown in subsequent sections.

3.6.2 Evapotranspiration

While precipitation drives the hydrologic cycle, evapotranspiration (ET) is the largest output on an annual basis for the Blue and Illinois River basins. ET is a forcing input that depletes the available soil moisture of a basin. Actual evapotranspiration depends on the available moisture in the soil profile and is considerably less than potential rates of evapotranspiration. Potential evapotranspiration represents the amount of evapotranspiration that would occur if there were a constant supply of moisture. The model requires potential evapotranspiration (PET) rates, which can be input as climatological values or as a timeseries. Monthly PET estimates for our simulations are esti-

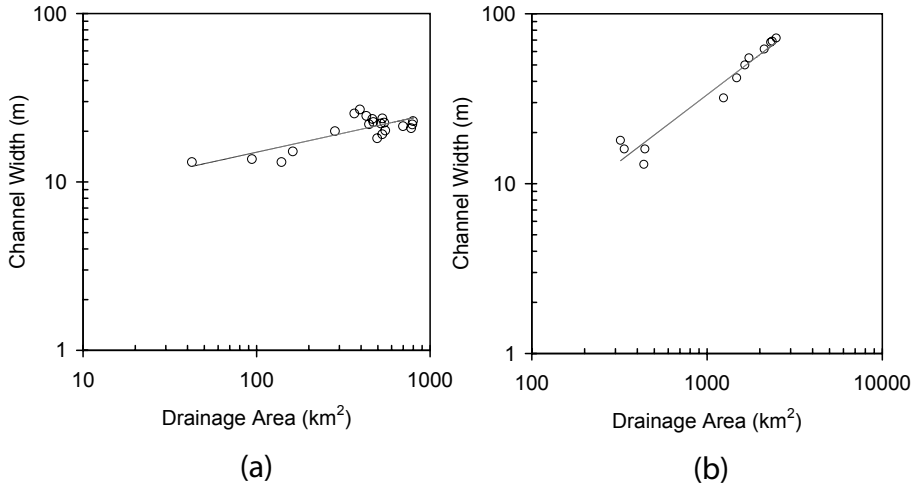

Figure 3.3: Channel width relationships for a) Blue River and b) Illinois River basins

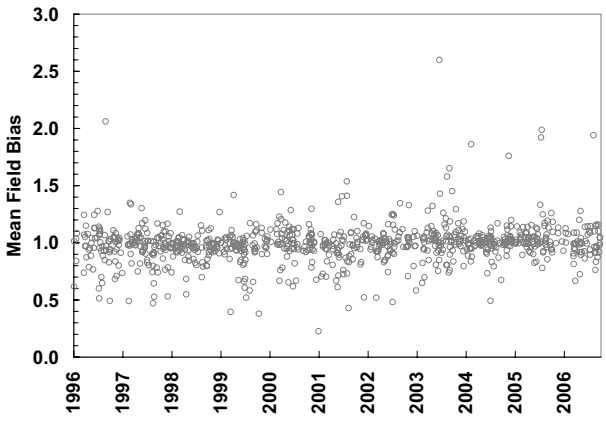

Figure 3.4: Time series of bias correction factors applied to MPE for Blue River basin from 1996–2006

mated from the Oklahoma Mesonet for the Blue River (Figure 3.5) and Illinois River basins based on meteorological observations. The Oklahoma Mesonet uses solar radiation, wind speed, air temperature, relative humidity, and pressure to compute PET using the Food and Agriculture Organization (FAO) Penman-Monteith equations (Allen et al., 1994). The NWS provided PET estimates for the Oklahoma basins (Koren et al., 1998); however, these values were lower than other estimates described below, and thus were discarded in favor of representative PET derived from the Mesonet stations located in and surrounding the basins. The NWS PET estimate for the Blue River basin is 1345 mm/yr, whereas, the Oklahoma Mesonet annual PET estimate is 1450 mm/yr. For the Illinois River, the NWS PET estimated 1066 mm/yr, while the Oklahoma Mesonet estimates accumulate to 1507 mm/yr. Carpenter and Georgakakos (2004) estimated similar PET of 1640 mm/yr for the Illinois River basin, which is closer to the Oklahoma Mesonet PET annual values than those provided in the DMIP experiment. The simulations presented herein are based on monthly PET derived from meteorological measurements at the nearby Oklahoma Mesonet stations that total to 1450 mm/yr and 1507 mm/yr, for the Blue River and Illinois River, respectively.

3.7 Distributed Model Calibration

Our approach to distributed model calibration seeks to estimate the magnitude and spatial distribution of model parameters that minimize differences between simulated and observed streamflow. Runoff-generating processes may vary from season to season, and may be occurring at the same time within a basin. Thus, a single objective function representing only one runoff process

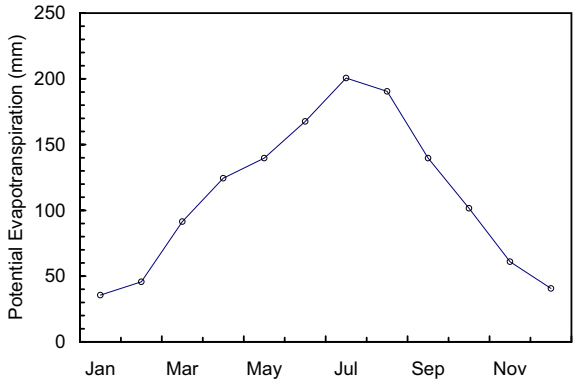

Figure 3.5: Monthly potential evapotranspiration for Blue River basin derived from climatological stations

or quantity may be inadequate to assess model performance (Gupta, 1998). Combining performance measures, e.g. peak and volume, that are representative of the dominant runoff process(es) may be more efficient at meeting project objectives (James and Burges, 1982). The approach used to calibrate V*flo* for DMIP2 is a multi-objective criteria composed of event scatter plots, two-dimensional objective function surfaces, and statistical performance measures.

Comparisons between the observed and simulated event volumes and event peak discharge are used to identify intra-storm biases. Analysis of simulated and observed streamflow scatter plots identifies groups of events that perform differently from other events, and if there is any bias in uncalibrated model performance.

Minimization of error between simulated and observed streamflow is critical to generating meaningful runoff results from a distributed hydrologic model.

A strength of physics based models is that the hydrologic cycle is formulated based upon intuitive physical laws. Vieux and Moreda (2003b) describe the Ordered Physics-Based Parameter Adjustment methodology (OPPA) for purposes of calibrating a distributed model. The OPPA approach balances optimization theory and the physics governing the hydrologic processes. In this method, spatially uniform scalar multipliers are used to adjust initial parameter map estimates derived from the geospatial data, with the intent of preserving spatial variability within physically realistic ranges. This approach takes advantage of predictable parameter interaction to optimize both volume and peak streamflow. Restating (3.1)(Vieux, 2004b) with adjustment factors for each of the model parameters results in,

$$\frac{\partial h}{\partial t} + \frac{S^{0.5}}{\beta\eta}\frac{\partial h^{5/3}}{\partial x} = \gamma R - \alpha I \tag{3.7}$$

where the three scalars α , γ , and β are the multipliers controlling infiltration rate(I), rainfall rate(R), and hydraulic roughness(η).

Because these scalars can be thought of as controls in optimal control theory, (3.7) may be used as the forward equation. When the inverse solution is obtained by using the adjoint formulation, the backward equation may be used to identify optimal values described in Vieux et al. (1998) and White et al. (2002, 2003). However, a manual adjustment of these scalar multipliers is applied in the optimization procedure as follows.

For our study, calibration of the model relies on the combination of the Nash-Sutcliffe efficiency coefficient for discharge and root mean square error (RMSE) in volume. The Nash-Sutcliffe efficiency, E_{Nash}, is defined as,

$$E_{Nash} = 1 - \frac{\sum_{i=1}^{n} \left(Q_{obs}^{i} - Q_{sim}^{i}\right)^2}{\sum_{i=1}^{n} \left(Q_{obs}^{i} - \bar{Q}_{obs}\right)^2} \tag{3.8}$$

where Q_{sim} is the simulated hourly streamflow, Q_{obs} is the observed hourly streamflow, and $\bar{Q}$ is the mean hourly observed streamflow. The minimization of the objective function for volume, J_v, is defined as,

$$minJ_v = \sqrt{\frac{\sum_{i=1}^{n} \left(V_{sim}^{i} - V_{obs}^{i}\right)^2}{n}} \tag{3.9}$$

where V_{sim} and V_{obs} are the simulated and observed event volumes. Identification of model biases between simulated and observed streamflow is necessary to guide the calibration process.

The first step in the OPPA method is to obtain volume agreement. To achieve this, we adjust hydraulic conductivity and soil depth to optimize J_v. Finally, channel hydraulic parameters are varied such that E_{Nash} is maximized. This procedure is carried out manually until the objective functions are optimized. Physically realistic parameters and predictable response and parameter interaction assist the manual method put into effect by a skilled operator. In Table 3.1 the a priori parameter values (uncalibrated) for the Blue River and Illinois River basins are given. Results of this calibration process for the Blue and Illinois River basins are given in the next section.

3.8 Results and Discussion

Comparisons are presented between uncalibrated and calibrated models using both the MPE and GCPE inputs. This allows for a systematic comparison between the effects of calibration and precipitation input. The simulations

Table 3.1: Average parameter values for Blue River and Illinois River basins

	Blue River		Illinois River	
Parameter	**Uncal**	**Cal**	**Uncal**	**Cal**
Sat. Hydr. Cond. (cm/hr)	0.66	0.94	7.26	6.53
Wetting Front Suction (cm)	14.83	14.83	27.1	27.1
Effective Porosity	0.423	0.423	0.376	0.376
Soil Depth (mm)	1080	430	711	1041
Overland Roughness	0.053	0.053	0.069	0.069
Channel Roughness	0.035	0.025	0.043	0.036
Channel Width (m)	14.384	14.384	11.163	9.935

performed were 1) MPE input with uncalibrated model parameters (MPE-Uncal); 2) MPE input with calibrated model parameters (MPE-Cal); 3) GCPE input with uncalibrated model parameters (GCPE-Uncal); and 4) GCPE input with calibrated model parameters (GCPE-Cal).

The calibrated simulation results are organized by the calibration and verification periods. Model performance for each period is evaluated in terms of 1) continuous time-series performance measures, 2) event scatter plots of peak discharge and volume, and 3) objective functions. Continuous time-series performance measures between simulated and observed stream flows are the mean, standard deviation, hourly root mean square error (HRMSE), the Nash-Sutcliffe efficiency coefficient, and the Pearson correlation coefficient. While these measures are not able to capture all of the information contained in a hydrograph, they do provide a quantification of model skill.

3.8.1 Uncalibrated Simulation Results

The baseline simulations using MPE-Uncal and GCPE-Uncal are presented in Tables 3.2 and 3.3. For the Blue River basin during the calibration period, E_{Nash} significantly increased from 0.34 for MPE-Uncal to 0.63 with GCPE-

Uncal. For the Tahlequah simulation point, there was a slight increase in E_{Nash} from 0.22 for MPE-Uncal to 0.23 with GCPE-Uncal. For Siloam Springs, there was a minor increase in E_{Nash} from 0.11 to 0.17. During the verification period, E_{Nash} for the Blue River increased from -0.38 using MPE-Uncal to -0.23 using GCPE-Uncal. There was no change in E_{Nash} between the MPE-Uncal and GCPE-Uncal for both the Tahlequah and Siloam Springs simulation points during the verification period.

The GCPE-Uncal Blue River event volumes during the calibration period are plotted in Figure 3.6a. Two distinct groups emerge in the Blue River scatter plot (Figure 3.6a) where the event volume is overestimated by a factor of 2.19, for the second group, the volume is underestimated by a factor of 0.28. The events that were overestimated could be produced from runoff processes that differ from the other events or are due to errors inherent in the MPE such as hail. The GCPE-Uncal Illinois River model produced relatively unbiased event volume, slope of 1.02, with minor random scatter as seen in Figure 3.6b.

Table 3.2: Uncalibrated streamflow statistics for calibration period (1996–2002)

BASINS	**Blue River (bluo2)**		**Tahlequah (talo2)**		**Siloam Springs (sloa4)**	
PRECIPITATION INPUT STATISTICS	MPE	GCPE	MPE	GCPE	MPE	GCPE
Observed mean (m^3s^{-1})	9.6	9.6	30.5	30.5	18.7	18.7
Simulated mean (m^3s^{-1})	11.4	10.8	50.6	52.5	30.3	31.7
Observed S.D. (m^3s^{-1})	31.4	31.4	55.9	55.9	42.2	42.2
Simulated S.D. (m^3s^{-1})	36.5	32.4	66.2	69.2	53	56.1
HRMSE (m^3s^{-1})	25.5	19.1	49.5	48.9	39.7	38.5
Pearson correlation coefficient	0.73	0.82	0.74	0.78	0.7	0.76
Nash-Sutcliffe efficiency	0.34	0.63	0.22	0.23	0.11	0.17

Table 3.3: Uncalibrated streamflow statistics for verification period (2002–2006)

BASINS	**Blue River (bluo2)**		**Tahlequah (talo2)**		**Siloam Springs (sloa4)**	
PRECIPITATION INPUT STATISTICS	MPE	GCPE	MPE	GCPE	MPE	GCPE
Observed mean (m^3s^{-1})	4.6	4.6	18.8	18.8	13.3	13.3
Simulated mean (m^3s^{-1})	6.6	6.6	37.1	37.2	23.9	23.9
Observed S.D. (m^3s^{-1})	13.5	13.5	44.1	44.1	35.5	35.5
Simulated S.D. (m^3s^{-1})	20.4	20	51.2	51.3	40.2	40.2
HRMSE (m^3s^{-1})	15.9	15	38.7	38.8	33.7	33.8
Pearson correlation coefficient	0.63	0.67	0.75	0.75	0.65	0.65
Nash-Sutcliffe efficiency	-0.38	-0.23	0.23	0.23	0.1	0.1

3.8.2 Calibration Results

Assumed processes are infiltration rate excess and saturation excess runoff that operate simultaneously. Both processes are handled by V*flo* where saturated hydraulic conductivity and soil depth (depth to a restricting layer) control infiltration rate excess and saturation excess runoff processes, respectively. Wetting front suction is another parameter in the Green and Ampt equation affecting the infiltration rate, but it is not adjusted. To handle the occurrence of the two runoff processes operating simultaneously in the watershed, the saturated hydraulic conductivity and soil depth are adjusted by spatially uniform scalar multipliers in order to optimize the objective functions for volume, J_v and E_{Nash}.

3.8.2.1 Optimal Parameter Values

Calibration of soil depth, S_d, and saturated hydraulic conductivity, K_{sat}, reduces the error in infiltration rate excess and saturation excess runoff generation . These two parameters primarily affect streamflow volume and indirectly, peak discharge because of the relationship between volume and peak. The objective functions for E_{Nash} and J_v are computed by adjusting the soil depth and saturated hydraulic conductivity calibration factors. Objective functions are shown in Figure 3.7 for a) E_{Nash} and b) J_v for the Blue River calibration period (1996–2002). There is a global optimum in each of the objective functions that are coincident. While a truly unique parameter set may not exist, given the shape of the objective function we would not expect a markedly different optimal parameter set. The a priori parameter set, as shown in Table 3.1, is $S_d = 1080$ mm and $K_{sat} = 6.6$ mm/hr. The objective function for E_{Nash}

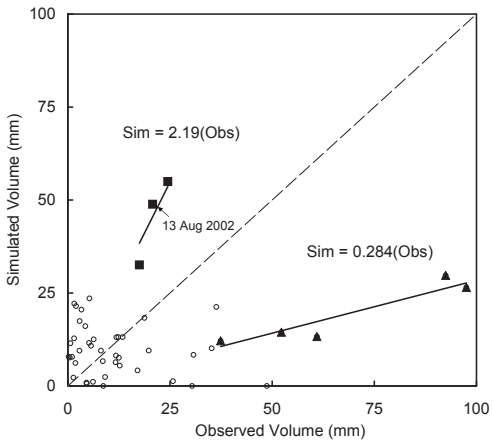

(a)

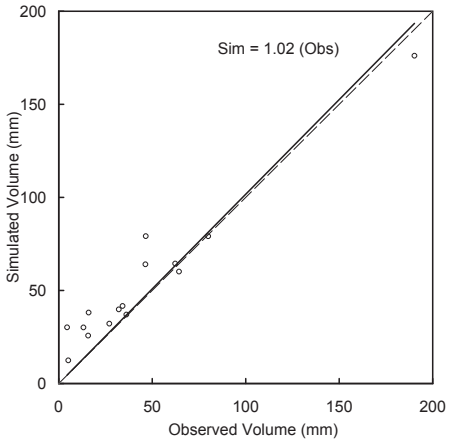

(b)

Figure 3.6: Uncalibrated simulated and observed direct runoff volume using GCPE input and Mesonet PET for a) Blue River and b) Illinois River basins. Solid squares show proposed infiltration rate excess events, circles are undetermined dominate runoff process events, and solid triangles are proposed saturation excess events.

has a global maximum at a S_d = 430 mm and K_{sat} = 9.4 mm/hr. There is a flat portion in the E_{Nash} function near the vicinity of S_d = 430 mm and K_{sat} between 8.7–11.4 mm/hr. That is, when K_{sat} varies between 8.7 and 11.4 mm/hr there is minimal change in the E_{Nash} objective function. The J_v objective function has a global minimum at a S_d = 430 mm and K_{sat} = 10.0 mm/hr and elongated contours that correspond to the flat surface in the E_{Nash} objective function. The trough and elongated contours imply that the Blue River basin responds more to S_d than K_{sat}, which suggests more runoff is generated from saturation excess as opposed to infiltration rate excess. However, there is some interaction between the two parameters because K_{sat} controls how fast the available porosity is filled and saturation achieved.

Consider for example, the event from December 1997 to February 1998 in the Blue River basin shown in Figure 3.8. The first hydrographs respond reasonably well, but discharge falls well below observed for subsequent events. It is hypothesized that the basin runoff response during this period is due to both saturation excess and infiltration rate excess operating together. Changing the soil depth from 1080 mm to 430mm improved the prediction of peak discharge and runoff volume. However, there was almost no change in the first peak of the event. Therefore, it is hypothesized that the first peak responds to infiltration rate excess runoff dominating at the beginning, and then later, the response is dominated by saturation excess.

3.8.2.2 Continuous Streamflow Performance

For October 1996 to September 2002, the V*flo* model was calibrated using hourly simulated and observed streamflow. The calibrated simulation results using MPE and GCPE inputs are provided in Table 3.4 for the main outlets

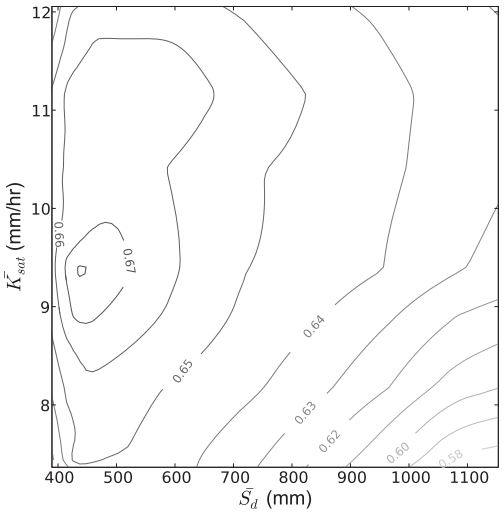

(a)

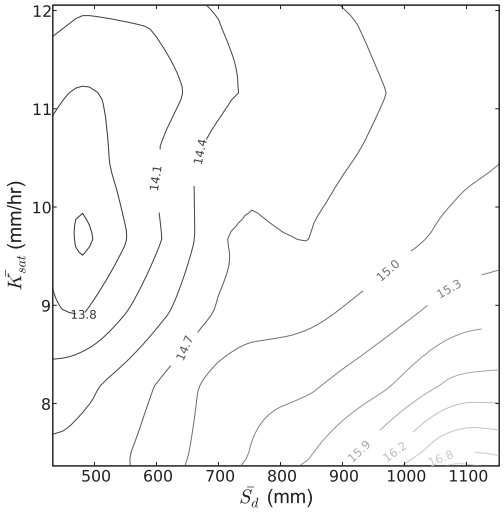

(b)

Figure 3.7: Objective functions for Blue River a) Nash-Sutcliffe efficiency, E_{Nash} and b) event volume error, J_v (mm)

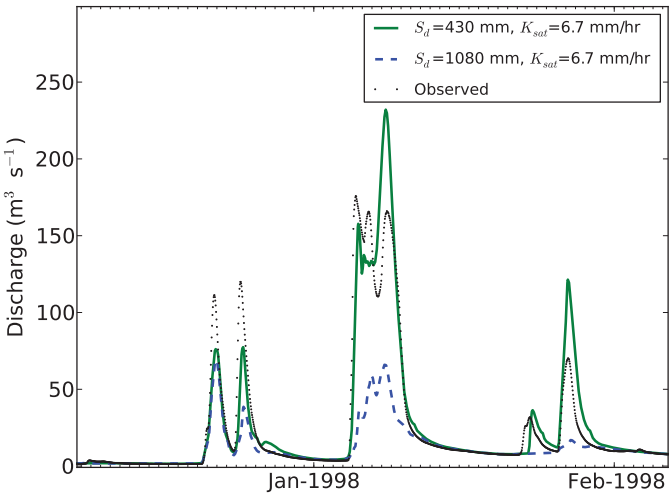

Figure 3.8: Hydrograph showing variable runoff generation process for the Blue River at Blue, January 1998

of the Blue and Illinois River basins. The model performance was relatively consistent among the stream gauge locations in the Blue and Illinois Rivers shown.

Using GCPE as input, calibration of the Blue River model increased E_{Nash} from 0.63 to 0.68 and improved the correlation coefficient from 0.82 to 0.83. In the Blue River for a selected period in 1997 (Figure 3.9a), good agreement is evident from the hourly streamflow, which has a comparable E_{Nash} of 0.81. For the Illinois River at Tahlequah calibration improved the E_{Nash} from 0.23 to 0.61, and improved the correlation coefficient from 0.78 to 0.80. Agreement between simulated and observed streamflow is achieved with a E_{Nash} of 0.69 computed on hourly discharge pairs at Tahlequah in the Illinois River during a selected period in 1999 as seen in Figure 3.9b. For the Illinois River at Siloam Springs, calibration improved E_{Nash} from 0.17 to 0.62, and improved the correlation coefficient from 0.76 to 0.80. Some adjustment of trapezoidal channel

width was needed to improve accuracy of peak discharge and arrival time at Tahlequah, which is presented in Table 3.1 along with the other calibrated parameter values.

Table 3.4: Calibrated streamflow statistics for calibration period (1996–2002)

BASINS	**Blue River (bluo2)**		**Tahlequah (talo2)**		**Siloam Springs (sloa4)**	
PRECIPITATION INPUT STATISTICS	MPE	GCPE	MPE	GCPE	MPE	GCPE
Observed mean (m^3s^{-1})	9.6	9.6	30.5	30.5	18.7	18.7
Simulated mean (m^3s^{-1})	10.6	9.6	35.7	36.5	21.3	22.1
Observed S.D. (m^3s^{-1})	31.4	31.4	55.9	55.9	42.2	42.2
Simulated S.D. (m^3s^{-1})	35.4	29.7	46.9	50	35.8	39.2
HRMSE (m^3s^{-1})	24.5	17.7	37.3	34.7	28.4	26.1
Pearson correlation coefficient	0.74	0.83	0.76	0.8	0.75	0.8
Nash-Sutcliffe efficiency	0.39	0.68	0.56	0.61	0.55	0.62

Comparisons have also been performed between each of the rainfall inputs during the calibration period for the main outlets. For the Blue River, the MPE-Uncal had a E_{Nash} of 0.34, and the MPE-Cal had a E_{Nash} of 0.39. The GCPE-Uncal input had a E_{Nash} of 0.63, and the GCPE-Cal had a Nash Sutcliffe efficiency of 0.68. A 74% increase in E_{Nash} for the calibrated model is obtained using GCPE input for the Blue River. For the Illinois River, the MPE-Uncal had a E_{Nash} of 0.22, and the MPE-Cal had a E_{Nash} of 0.56. The GCPE-Uncal had a E_{Nash} of 0.23, and the GCPE-Cal had a E_{Nash} of 0.61. For the Illinois River basin, model calibration improved prediction accuracy more than using GCPE as input.

For the Blue River basin, the event volumes obtained using MPE and GCPE inputs are shown in Figure 3.10 a) and b), respectively. GCPE improved accuracy in the Blue River. For the MPE-Cal input, the Blue River event volume has an RMSE of 11.7 mm. With the GCPE-Cal, the event volume accuracy improves with a decreased RMSE of 6.90 mm for the Blue River at Blue. The sensitivity of using GCPE precipitation input is also seen in the scatterplots of peak discharge using the MPE-Cal (Figure 3.11a) and GCPE-Cal (Figure 3.11b). The peak discharge using MPE-Cal at Blue has a bias of 1.05 with an RMSE of 97.6 $m^3 s^{-1}$. Using GCPE-Cal improves the results with a bias of 0.996, and an RMSE of 67.7 $m^3 s^{-1}$. The improvement in prediction accuracy gained from using GCPE input over the provided MPE in prediction accuracy is RMSE = 41% and 31% in volume and peak, respectively.

For the Illinois River basin using GCPE input, scatter plots for volume and peak streamflow (Figure 3.12 a, b) show that the simulated volume is greater than the observed for the low flow events, but less than observed for larger events. In the Illinois River, the accuracy for event volume prediction

(a)

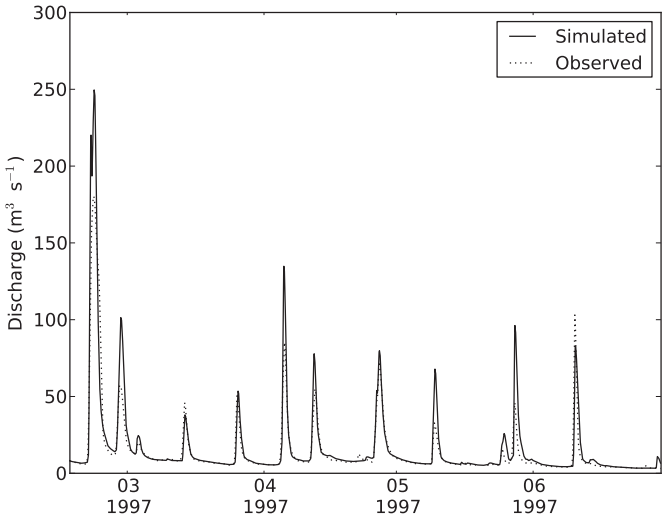

(b)

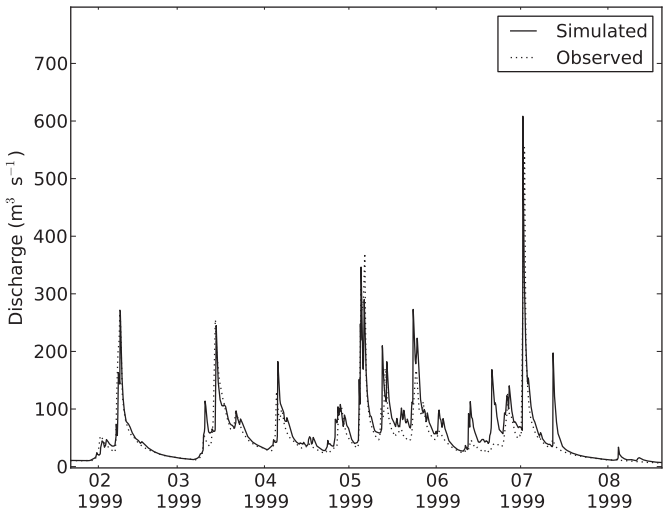

Figure 3.9: Continuous streamflow hydrograph with GCPE input and Mesonet PET for a) Blue River basin in 1997, and b) Illinois River basin in 1999

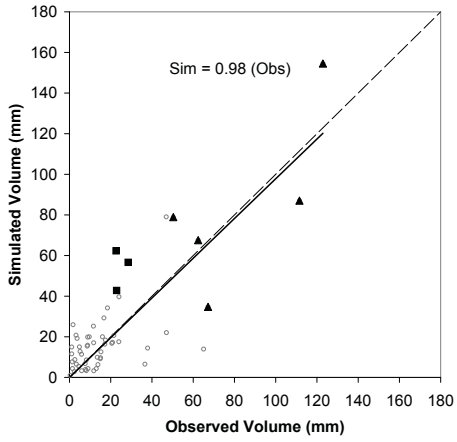

(a)

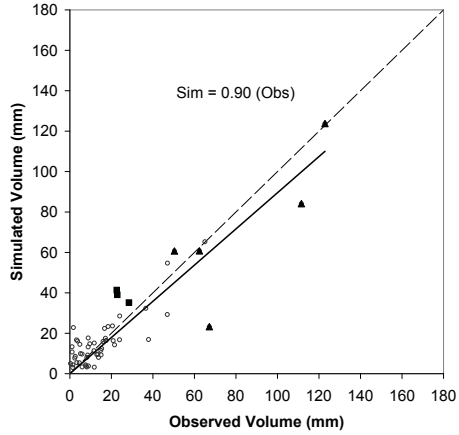

(b)

Figure 3.10: Calibrated event volume scatter plots for the Blue River using Mesonet PET with a) MPE input and b) GCPE input

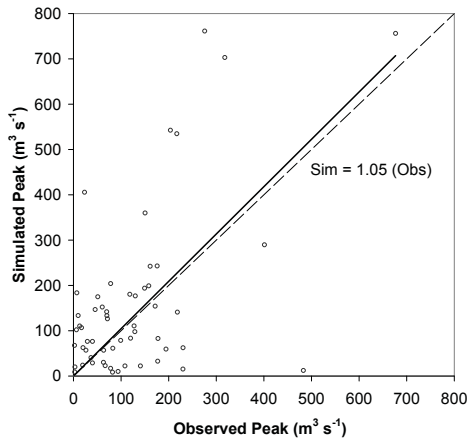

(a)

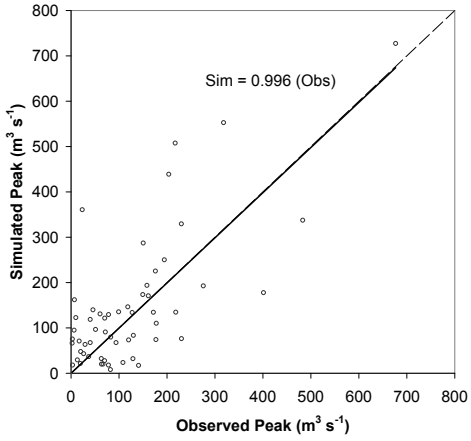

(b)

Figure 3.11: Calibrated event peak discharge scatter plots for Blue River using Mesonet PET with a) MPE input and b) GCPE input

is excellent with a bias of 1.16 and an RMSE of 10.1 mm. The peak discharge has a bias of 0.84 with an RMSE of 138 $m^3 s^{-1}$.

Continuous time-series performance measures for the Blue and Illinois River basins indicate the model is able to reproduce the observed streamflow with a Nash-Sutcliffe efficiency coefficient of at least 0.59 with the highest efficiency of 0.68 during the calibration period in the Blue River basin. Gauge correction of MPE rainfall lead to a 74% increase in the Nash-Sutcliffe efficiency for the Blue River basin.

3.8.3 Verification Results

Model verification assesses the calibrated model predictive ability using an independent dataset. The verification period is from October 2002 to September 2006, when the Blue river basin showed the most improvement due to calibration during the verification period. The calibrated simulation results using MPE and GCPE inputs are provided in Table 3.5 for the main outlets of the Blue and Illinois River basins. The GCPE-Uncal had an E_{Nash} of -0.23, whereas, GCPE-Cal improves E_{Nash} to 0.18. The MPE-Cal had an E_{Nash} of only 0.01, but GCPE-Cal improves E_{Nash} to 0.18.

For the Illinois River at Tahlequah, GCPE-Cal performed best during the verification period. E_{Nash} for the GCPE-Uncal was 0.23 while the E_{Nash} for GCPE-Cal was 0.58, which is essentially the same performance obtained during the calibration period. Using GCPE instead of MPE during this period, E_{Nash} improved slightly, i.e. 0.57 to 0.58.

The Illinois River at Siloam Springs also had the most improvement due to calibration during the verification period. E_{Nash} using the GCPE-Uncal was 0.10 while E_{Nash} for GCPE-Cal was 0.45. E_{Nash} slightly improved from

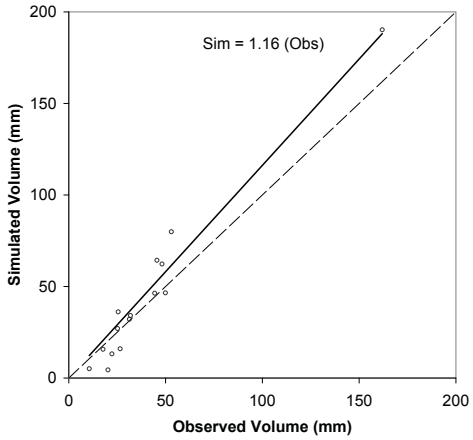

(a)

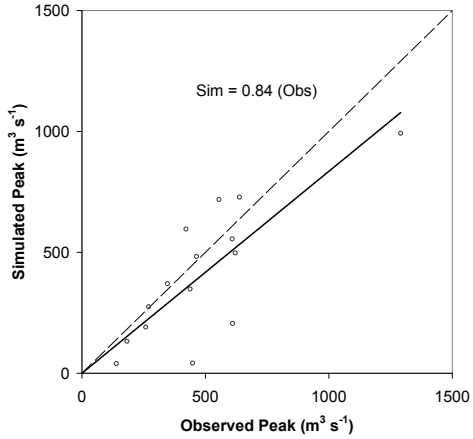

(b)

Figure 3.12: Calibrated event scatter plots with GCPE input and Mesonet PET for the Illinois River a) volume, and b) peak discharge

0.44 for MPE-Cal to 0.45 GCPE-Cal. Recall that Oklahoma Mesonet gauges are not located in or around the drainage area contributing to Siloam Springs Arkansas, which may suggest why little prediction improvement is obtained using GCPE as input for the Illinois River.

Prediction accuracy during verification is nearly equivalent to calibration period for the Illinois River regardless of precipitation input, i.e. GCPE or MPE. Within the Blue River, the prediction accuracy during the verification period was considerably less than the calibration period, but improved with GCPE and calibration.

Table 3.5: Calibrated streamflow statistics for verification period (2002 - 2006)

BASINS	**Blue River (bluo2)**		**Tahlequah (talo2)**		**Siloam Springs (sloa4)**	
PRECIPITATION INPUT STATISTICS	MPE	GCPE	MPE	GCPE	MPE	GCPE
Observed mean (m^3s^{-1})	4.6	4.6	18.8	18.8	13.3	13.3
Simulated mean (m^3s^{-1})	5.8	5.5	23.9	24.4	15.5	15.8
Observed S.D. (m^3s^{-1})	13.5	13.5	44.1	44.1	35.5	35.5
Simulated S.D. (m^3s^{-1})	17.3	16.2	33.3	34.5	24.6	25.7
HRMSE (m^3s^{-1})	13.4	12.2	29.1	28.6	26.5	26.4
Pearson correlation coefficient	0.65	0.68	0.76	0.77	0.67	0.68
Nash-Sutcliffe efficiency	0.01	0.18	0.57	0.58	0.44	0.45

3.9 Summary

The fully distributed physics-based model, V*flo*, operated in an offline continuous simulation mode produces acceptable accuracy for both continuous streamflow and event peak discharge as evidenced by various performance measures. While the transformation of rainfall into runoff is a complex process, hydrologic modeling provides a means of assessing how well these varying runoff processes are represented. Calibration provides insight as to which model parameters and hydrologic processes are likely controlling runoff. Realistic parameters were identified through calibration that in most cases changed slightly from assumed a priori values. The largest change was soil depth controlling saturation excess. For the Blue River, soil depth was reduced from the 1080 mm estimated from the soil survey to 430 mm through calibration; the saturated hydraulic conductivity changes from 0.66 to 0.94 cm/hr through calibration; and channel roughness is decreased from 0.035 to 0.025, whereas other parameters are unchanged as shown in Table 3.1. For the Illinois River, the saturated hydraulic conductivity is decreased from 7.26 to 6.53 cm/hr; soil depth increases from 711 to 1041 mm; channel roughness is reduced from 0.043 to 0.036, and channel width is decreased on average from 11.2 m to 9.9 m, whereas other parameters are unchanged (Table 3.1). Calibration showed the Blue River basin responds more to soil depth than to hydraulic conductivity. Use of GCPE and the calibration procedure that treats saturation excess and infiltration rate excess as operating simultaneously improves continuous and event-based prediction accuracy. Model calibration improved the Nash-Sutcliffe efficiency coefficient from 0.63 to 0.68 for the Blue River, while the GCPE input improves the Nash-Sutcliffe efficiency coefficient from 0.39 to 0.68

for the Blue River during the calibration period.

The major findings of this study may be summarized as follows:

1. Continuous and event-based calibration and verification identified an optimum parameter set that minimized the objective function based on Nash-Sutcliffe efficiency coefficient.

2. The Blue River exhibits both saturation excess and infiltration rate excess runoff processes. However, the Illinois River did not show distinct differences between the two runoff processes.

3. There was more improvement in model accuracy from gauge correcting the MPE input (GCPE) than from model calibration for the Blue River basin during the calibration period.

4. Prediction accuracy during the verification period was lower than the calibration period in the Blue River, where streamflow was dominated by baseflow.

5. For the Illinois River basin, the model was able to reproduce the observed streamflow with a Nash-Sutcliffe efficiency coefficient of 0.61 and 0.58 for the calibration and verification periods respectively using GCPE.

Model results demonstrated that varying runoff processes may be occurring within the Blue River basin. These processes could be accurately simulated if both saturation and infiltration-rate excess runoff processes are accounted for using accurate input. The identified optimal parameter set produced good results in both continuous and event-based comparisons when using the more accurate and representative precipitation input. The distributed model is sensitive to uncertainties in model input, but not uniformly for all periods. During

the 1996-2002 period, GCPE input was more important in achieving accurate results than model calibration for the Blue River, while model calibration proved more important in the Illinois River. During the 2002-2006 period, calibration proved more important than using GCPE input during the 2002-2006 in both the Blue and Illinois River basins. These results are important because it demonstrates that input uncertainty is nearly unavoidable, and can confound the proper identification and evolution of model states associated with perturbations in parameters.

Chapter 4

An Assessment of Distributed Flash Flood Forecasting Accuracy using Radar and Rain Gauge Input for a Physics-Based Distributed Hydrologic Model

4.1 Abstract

[1] One approach to reducing societal impacts from flooding is to minimize the public's exposure by closing flooded intersections, warning, and evacuating affected stakeholders. Emergency responders must know when and where flooding is likely to occur. This article describes the real-time performance of a flash flood forecasting system for a significant flood event (September 7-8, 2010) in Austin, Texas. The system uses a physics-based distributed (PBD) hydrologic model, V*flo*, together with radar rainfall input to predict stage and discharge at 222 locations in real-time. A comparison of model forecast accuracy using the operational rain gauge-adjusted radar rainfall input (GARR) is made against rain gauge only (RGO) input for a recent flash flood. A collection of calibrated hydrologic models for flash flood prone basins, within the City of Austin, is used for the comparison. A 1.9 hr reduction in timing error was achieved using GARR as input rather than RGO. The RMSE of peak stage forecasts with GARR was 0.89 m, but with RGO input, the peak stage

[1] Adapted version of Looper, J. P., and Vieux, B. E. (2012). An Assessment of Distributed Flash Flood Forecasting Accuracy using Radar and Rain Gauge Input for a Physics-Based Distributed Hydrologic Model. *Journal of Hydrology*, 412, 114-132.

RMSE increased to 1.77 m. The use of GARR as input to the PBD model not only increases the forecast lead-time accuracy, but also the accuracy of forecast peak stage across a range of basin sizes and with variable rain gauge densities used for radar bias correction. Rain gauge density over the forecast basins was one of the main determinants of forecast accuracy during an extreme event that resulted in significant flooding in a major metropolitan area.

4.2 Introduction

Flash flood mitigation requires emergency responders to know when and where flooding is going to happen. Flood impacts in urban areas are elevated due to high population density, imperviousness, and flood wave acceleration due to stream channelization. From a societal impact perspective, useful hydrologic forecasts provide time to close roads, re-route traffic, activate high-water signals, and deploy emergency personnel before a flood occurs. Flood stage forecasts in urban areas are especially difficult because the basin's hydrologic response time is the same order of magnitude as the emergency response time. Due to the speed of flood waves in urban watersheds, there is often insufficient time to make manual adjustments to model input or parameters. Flash flood forecast accuracy and reliability depend strongly on model structure configuration, input accuracy, and correct model parameter calibration. While any model is a simplification of complex runoff and hydraulic processes, physics-based distributed (PBD) hydrologic modeling uses the spatially variable hydraulic characteristics of a basin to determine hydrologic response at locations distributed across an urban area.

This article describes the performance of the operational distributed flash

flood forecasting system in Austin, Texas. The flash flood forecasting system uses the PBD model, V*flo*, and radar rainfall input to predict flood stage and discharge at 222 locations in real-time. The study goal is to evaluate if the flash flood forecasts issued using a merged input from radar and rain gauges (GARR) was better than using a rain-gauges-only product (RGO). The City of Austin is one of the most flash-flood prone regions in North America. The forecast lead-time accuracy is critical for taking emergency actions. Evaluative statistics are presented regarding the accuracy and reliability of flood forecasts achieved using GARR compared to RGO input at 21 stream flow gauges distributed throughout seven basins covering a combined area of 1200 km^2. Figure 4.1 shows the drainage area boundaries with the rain gauge network coverage (164 gauges) used to correct the radar rainfall input.

PBD hydrologic models use conservation equations to route runoff through a network of channel and overland flow elements. Because the full dynamic equations, referred to as St. Venant equations, are more complex than required for many watersheds, a simplified flow analogy such as the kinematic or diffusive wave is often used. Vieux and Gauer (1994), among others, have proposed the runoff routing using a numerical solution of the kinematic wave equation through a gridded representation of the watershed based on information derived from a digital terrain model and other geospatial data. The discretization scheme and resulting numerical method for solving conservation equations for open channel flow is often the finite difference solution (Julien and Saghafian, 1991; Ogden and Julien, 1993; Downer and Ogden, 2004), whereas finite volume modeling with 1-D and 2-D irregular meshes has been employed by Cunge (1980), and Fang and Su (2006). The application of the finite element solution in space and finite difference in time was employed in

r.water.fea (Vieux and Gauer, 1994), and V*flo* described in Vieux (2004a,b), and its application to flood prediction in Looper et al. (2009), and Vieux et al. (2009).

Flood warning systems provide lead-time for emergency responders to evacuate citizens and deploy resources to assess flood damage. To be useful, these systems must provide adequate response time for mitigation of flood impacts, especially where emergency response actions are taken based on the hydrologic forecast and warning. Creutin et al. (2009) compared social response time to basin response time in terms of effectiveness, and found that for small basins with drainage areas less than 100 km^2, the rainfall spatial distribution and accuracy were the most important determinants of effective flood warning. They reported the most important factors that reduced flood impacts during extreme flash flood generating storms were: 1) continuous enhancement of radar rainfall accuracy and its quality control; 2) providing access to more accurate real time information about rainfall accumulations during the decision-making process, and, 3) widespread access to information and dissemination of products that are readily understandable by people at risk. The system described herein incorporates these features, except that dissemination is not to the public but to city employees tasked with responding and helping to protect the public from flood hazards. Thus, flood information with relatively short lead time is useful. The methodology and results of the radar-based flood alert system are presented in the following section.

4.3 Methodology

4.3.1 Study Area

Rainfall and terrain characteristics of the City of Austin result in flooding as a public safety issue. The City is located in central Texas on the Colorado River that crosses the Balcones escarpment, separating the steeply sloped and hilly topography called the Texas Hill Country from the flatter plains area called the Blackland Prairies to the east. Steep slopes in the western part of Austin and Travis County provide only a thin covering of topsoil derived from limestone and shale geologic material. Austin is located near the Gulf Coast of Texas, where tropical storms are capable of producing heavy precipitation. The combined effect of ample atmospheric moisture near the Gulf coupled with steep topography in the headwaters and flatter areas in receiving portions of the watershed, that are either fully developed or are urbanizing with mixed land use, leads to dangerous conditions from flash floods.

The City of Austin experiences flooding over a range of watershed sizes that have response times with considerable variability making a distributed framework useful for managing flood emergencies. A recent flood event, 7-8 Sep 2010, illustrates the vulnerability of the city to flooding. Tropical Storm (TS) Hermine formed just off the south Texas coast on September 7, 2010, when the system made landfall and traveled north towards the San Antonio-Austin area over the day. Between the hours of 20:00 on 7 Sep10 through 05:00 on 8 Sep10 heavy rainfall occurred primarily on the west side of Austin. The rainfall resulted in 32 road closures due to inundation; 9 structures flooded due to creeks overflowing their banks; 30 structures that flooded due to localized

flooding; 4 swift-water rescues (two on Bull Creek, one on Shoal Creek, and one on Canyonwood in Travis County); and one death.

Portions of the watershed areas affecting the City are monitored with stream gauges as shown in Figure 4.1. There are 222 forecast locations (watch points) in the City, but only 21 have stream gauges, which are maintained by the US Geological Survey. A distributed hydrologic model, V*flo* described below, provides a distributed framework for managing flood stage information at these watch points. Table 4.1 presents the watershed areas and model resolution in the study area. The basin sizes range from 16.5 km^2 to over 839 km^2 and model grid sizes from 50 m to 250 m in horizontal resolution. In real-time, the total area modeled with the PBD model is 1200 km^2, which runs continuously to track soil moisture, rainfall, and stream flow over each model grid.

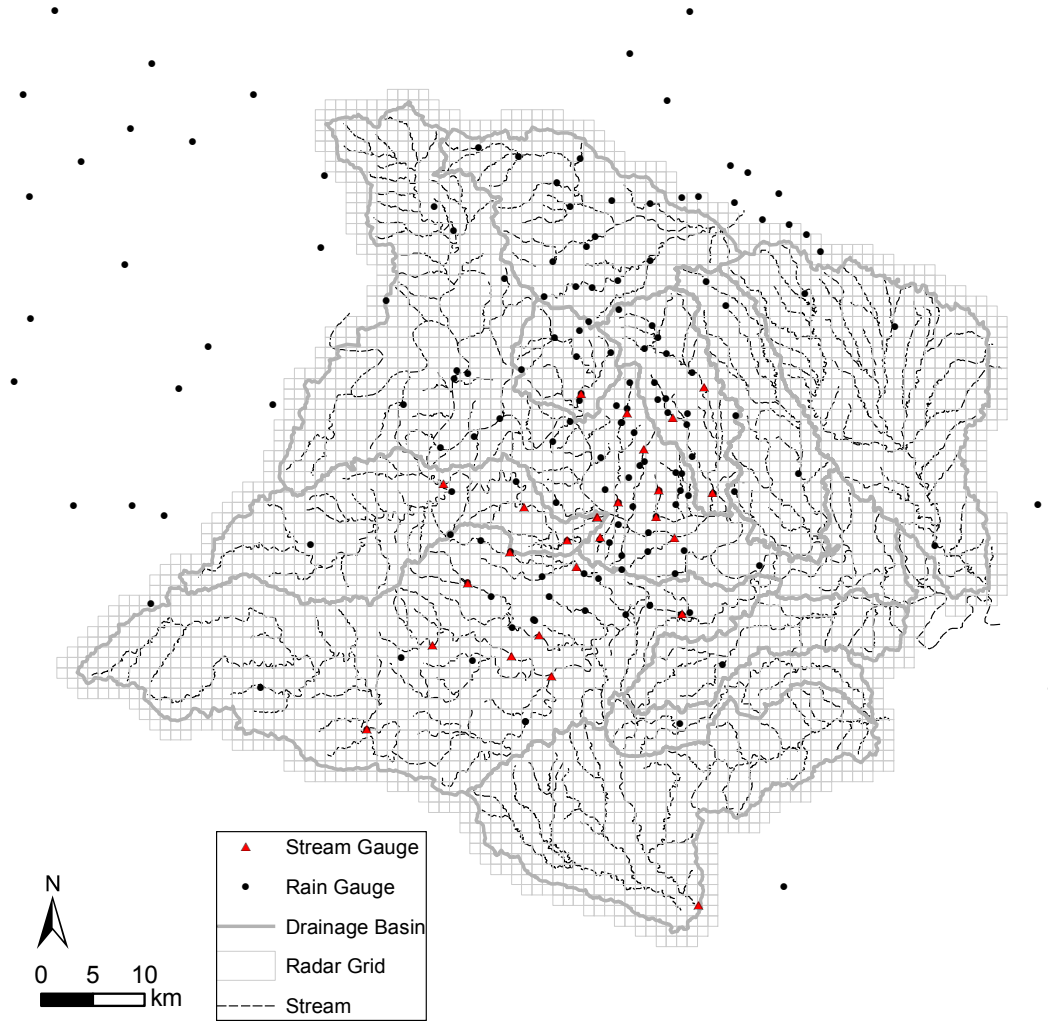

Figure 4.1: Rain gauge and streamflow gauge networks covering the target watersheds affecting the City of Austin TX

Table 4.1: Model resolution, forecast watch points, and watershed area

	Grid Resolution (m)	**No. of grids**	**No. of watch points**	**Drainage Area (km^2)**
Shoal Creek	60	9000	38	32.4
Onion Creek	250	13426	7	839.1
Waller Creek	50	6588	27	16.5
Walnut Creek	150	6533	48	147.0
Bull Creek	70	11694	5	57.3
Boggy Creek	65	8429	43	35.6
Williamson Creek	150	3467	54	78.0
Total		59137	222	1205.9

4.3.2 Radar Rainfall

The Flood Early Warning System (FEWS) rain gauge network consists of telemetered gauges connected via SCADA (Supervisory Control and Data Acquisition). SCADA reliably transmits rainfall data used in real-time operations. The rainfall used in real-time distributed hydrologic modeling consists of radar at 1-km resolution, and rain gauge coverage in and surrounding the target watersheds affecting the City of Austin. The rain gauge network is composed of several heterogeneous networks as seen in Figure 4.1. Automated rejection of erroneous gauge data greatly improves the bias correction of radar in offline and online applications (Steiner et al., 1999; and Marzen and Fuelberg, 2005). The City of Austin radar coverage is primarily served by a single S-band NEXRAD (WSR-88D) radar; however, two additional NEXRAD radars can provide a backup if the primary radar is offline. Reflectivity is converted by means of a default Z-R, but is continuously adjusted in real-time by the rain gauge network with updates every 15 minutes. The study area is located within 80 km of the radar with a beam top height of approximately 1.7 km; therefore, making overshooting unlikely except at the far reaches of the modeled area to the north even with wintertime stratiform storms.

Dependence of runoff forecast reliability on precipitation input and soil moisture, both in offline and real-time modes, has been demonstrated by studies reported by Vieux et al. (2009), Norbiato et al. (2008), and Anquetin et al. (2010) among others. Bias correction of radar for hydrologic applications has been demonstrated to improve stream flow prediction in both offline (Vieux et al., 2009; Habib et al., 2008; Gourley and Vieux, 2005 and 2006; and Vieux and Bedient, 2004), and in online applications (Vieux et al., 2003; Bedient et

al., 2003). It is well recognized that bias correction of radar improves rainfall estimation and resulting hydrologic prediction accuracy as reported by Collier and Knowles (1986) and Mimikou and Baltas (1996); in urban areas presented by Vieux and Vieux (2005) and Vieux and Bedient (2004); and in Borga et al. (2010) in the overview of a special issue on flash floods and the articles contained therein.

Hydrologic prediction requires precipitation that is accurate and representative for the watershed area. The initial use of GARR for input is described as follows. While the method of adjustment depends on the hydrologic application and the spatial extent of the area of interest, the mean field bias (MFB) approach is useful for identifying gauges that are not consistent with the radar using a spatially constant adjustment factor and also reducing the single rain gauge error from corrupting the bias correction (Bedient et al., 2008). The Local Bias (LB) approach to adjusting the radar rainfall applies a spatially-variable ratio of gauge to radar accumulations (G/R) from surrounding gauges with the closest gauge having the most weight (Seo and Breidenbach, 2002). The LB approach used here distributes the variation of bias over the area based on a 6-hour moving window that is updated every 15-minutes. The 6-hr moving window is an integration period updated every 15 minutes, which is similar to the window probability matching method (Rosenfeld, 1994). The LB uses the ratio between the sum of each gauge divided by the sum of the sampled radar values over each gauge. Gauge and radar accumulations were computed for each moving window. All radar/gauge (RG) pairs were then checked for statistical outliers. Exclusion of any gauge accumulation during a moving window is based on control limits of two standard deviations from the mean. After exclusion, remaining RG pairs are then distributed spatially over

the analysis area using a Barnes objective analysis scheme (Barnes, 1964). The resulting LB value over each radar bin is the multiplicative factor that adjusts the radar. The Barnes objective analysis scheme is also used to perform the spatial interpolate the rain gauge data for the rain gauge only (RGO) input.

The rain gauge network density is important for characterizing rainfall variability alone or in conjunction with radar. Collier (1986) recommended a rain gauge spacing of 20 km to produce results as accurate as radar in Northwest England for all precipitation types, e.g. frontal, showers, and bright-band affected storms. Since then, many researchers and practitioners have employed rain gauge networks for validation of the quantitative precipitation estimates, evaluated inaccuracies in GARR on flood forecasting, and identified improvements needed for uniform reliability of rainfall measurements. Errors in precipitation estimates derived from radar can lead to inaccurate stream flow predictions and mis-calibration of hydrologic models (Winchell et al., 1998). To overcome this inaccuracy in post-event analysis, Bouilloud et al. (2010) developed an effective Z-R relationship through optimization using rain gauges to identify coefficients that minimized event-scale rainfall measurement differences. They found that an effective Z-R relationship could be optimized with respect to rain gauge accumulations measured at the event time scale, and that this approach could compensate for range dependent errors associated with radar. Coefficients of the Z-R relationship can vary significantly over time and space. Continuous updating of spatially variable radar bias correction factors is important for radar-based flood forecasting, especially where local downdrafts during storms can enhance rainfall rates that would otherwise go undetected by radar (Smith et al., 2007).

4.3.3 Hydrologic Model

Each basin in the study area is modeled with a series of discrete elements joined together forming a drainage network that are used to solve conservation of mass and momentum within the kinematic wave analogy (KWA). A central component of the flash flood forecasting system is PBD model, V*flo* (Vieux, 2004a,b), which solves the KWA equations using the finite element method (Vieux, 1988). The one-dimensional finite elements used in this approach are assigned as overland or channel cells with appropriate hydraulic characteristics. Within the model, two coupled components generate the simulated hydrologic response: 1) routing of runoff according to a fully turbulent open channel flow, and 2) runoff generation composed of infiltration rate excess (Hortonian), saturation excess (Dunne), or both operating simultaneously in a watershed. Manning's equation combined with the conservation of mass forms the governing partial differential equation for overland flow (Eq. 4.1),

$$\frac{\partial h}{\partial t} + \frac{S^{1/2}}{\eta}\frac{\partial h^{5/3}}{\partial x} = R - I \tag{4.1}$$

where h represents the flow depth in each element, S is the dominant land slope, η represents the nodal hydraulic roughness centered in each grid cell, R the rainfall rate over an element, and I the infiltration rate. Channel routing in the model uses the following form of the kinematic wave equation,

$$\frac{\partial A}{\partial t} + \frac{\partial Q}{\partial x} = q \tag{4.2}$$

where Q is the discharge or flow rate in the channel; A is the wetted area of the cross section; and q is the rate of lateral inflow per unit length of

the channel. The hydraulics of the overland and channel cells combined in a drainage network produce the hydrologic response of the basin without reliance on unit-hydrograph functions. Channel cross-sectional geometry is used to define the hydraulics, which are either surveyed or extracted from LiDAR digital elevation data. Hydraulic roughness is assigned based on dominant land cover in overland areas and as a composite η value in channels (Vieux, 2004b).

V*flo* models the infiltration rate, I, using the Green and Ampt equation,

$$I = K_s \left[1 + \frac{\Psi_f \Delta\theta}{F(t)} \right] \tag{4.3}$$

where K_s is the saturated hydraulic conductivity, Ψ_f is the wetting front suction head, $\Delta\theta$ is the soil moisture deficit, and $F(t)$ is the cumulative infiltration depth. The available soil moisture deficit is depleted at the potential evapotranspiration rate (PET). The soil moisture is also fully redistributed throughout the soil profile on a daily basis. Green and Ampt parameters are derived from soil water characteristics estimated by soil texture properties (Saxton and Rawls , 2006). Grid cells that contain impervious cover only allow infiltration to occur on the pervious portion of the cell. Infiltration is allowed to continue until the wetting front reaches the bottom of the soil depth layer, saturation occurs and then runoff equals rainfall.

4.3.4 Ordered Physics Based Parameter Adjustment

The ordered physics based parameter adjustment (OPPA) framework (Vieux and Moreda, 2003) is a guided calibration process for PBD models. The OPPA approach optimizes runoff volume parameters followed by the optimization

of overland and channel hydraulic parameters. The OPPA method focuses first on the parameters that influence runoff volume. The main parameters controlling runoff volume in V*flo* are soil depth and assumed porosity, and saturated hydraulic conductivity. Adjusting these parameters simultaneously includes both saturation excess and infiltration rate excess runoff-generating processes of the basin. The main steps in the OPPA method are:

1. Estimate spatially distributed parameters from physical properties.
2. Assign channel hydraulic properties based on measured cross-sections where available.
3. Study the sensitivity of each parameter (Figure 4.2).
4. Determine the optimum parameter set, which minimizes the respective objective functions for runoff volume, timing, and peak discharge.
5. Perform continuous and event based simulations then re-adjust parameters to account for interactions as necessary.

Spatially uniform scalar multipliers adjust a-priori distributed parameter estimates derived from soil and channel parameters with the objective of minimizing a function composed of the differences between observed and simulated quantities, e.g. volume, peak stage, and timing.

Objective function selection requires consideration of which features of hydrologic prediction are important for system objectives. Within the OPPA calibration procedure, parameters are first adjusted to minimize the error in volume, J_v defined as,

$$J_v = \sqrt{\frac{\sum_{i=1}^{n} (V_{sim} - V_{obs})^2}{n}} \tag{4.4}$$

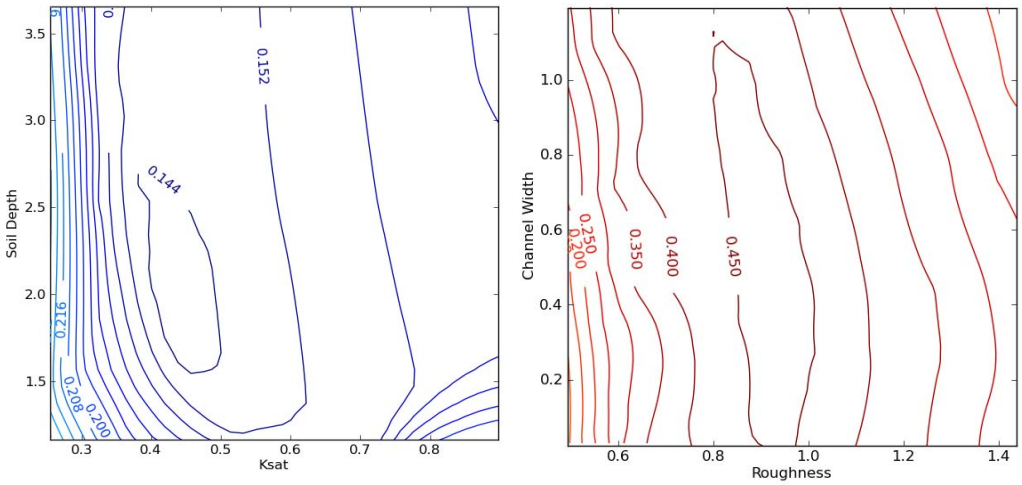

Figure 4.2: OPPA objective functions for Williamson Creek gauge (08158930).

where V_{sim} and V_{obs} are the simulated and observed runoff event volumes and n is the number of calibration events.

Next, hydraulic roughness and channel geometry are adjusted to fine-tune the timing aspects of hydrologic response, namely timing and peak discharge/stage. A flood alert system depends on accurate stage prediction, but confidence in the system requires accurate estimation of hydrologic response throughout an event. A common objective function is the Nash-Sutcliffe Efficiency, NSE, which is composed of the correlation, bias, and relative variability between simulated and observed values described by Gupta et al. (2009) as,

$$NSE = \overbrace{2 \cdot \alpha \cdot r}^{Correlation} - \overbrace{\alpha^2}^{Variance} - \overbrace{\beta_n^2}^{Bias} \tag{4.5}$$

where $\alpha = \frac{\sigma_{sim}}{\sigma_{obs}}$; $\beta_n = \frac{\mu_{sim} - \mu_{obs}}{\sigma_{obs}}$; r is the Pearson correlation coefficient; μ and σ are the mean and standard deviation of the observed (obs) and simulated (sim) series; α measures the variability between the simulated and observed

series, and β_n is the bias normalized by the standard deviation. Examples of the objective surfaces that were obtained in the calibration process by the OPPA method are shown in Figure 4.2. A batch process was used to explore the parameter space to identify the most probable parameter sets based on available rainfall events. The parameter scalars corresponding to minimum error in these plots are identified through the OPPA model calibration for use in real-time operation of the hydrologic models representing the basins.

4.4 Results

Evaluation of forecast stage accuracy obtained with GARR and RGO as input to the PBD model is presented in terms of rainfall input accuracy and rain gauge network density. Analysis focuses on the extreme event that identifies whether useful hydrologic warnings can be obtained for a range of basin sizes with variable rain gauge density.

4.4.1 Rainfall Accuracy

Rainfall inputs to a hydrologic model can affect the lead-time afforded for emergency response. GARR and RGO were used as the primary inputs to the hydrologic model. The GARR used in real-time, during this event, is produced through bias correction of a standard Z-R relationship, $Z = 300R^{1.4}$. However, Z-R relationships can be modified depending on precipitation type. The bias correction is computed over a 6-hr moving accumulation period updated every 15-min. The operationally computed time series of bias correction factors for the nine months leading up to the extreme event on 7-8 Sep 2010, is shown in Figure 4.3a, where the inset box indicates the extreme event period.

The bias correction factor shown is the average of the local bias correction factors, and shows considerable departure from a value of 1.0, i.e. perfect agreement between radar and gauge. In Figure 4.3b, the mean bias is plotted just for the extreme event period, 7-8 Sep 2010. The evolution of the bias during TS Hermine is interesting because it starts out at 1.5 and above. This magnitude of correction would be consistent with adjusting the convective Z-R relationship to be more characteristic of a tropical Z-R of $Z = 250R^{1.2}$. As described by Vieux and Bedient (1998), the expected increase in rainfall produced using the convective Z-R relationship would be 40% higher for storms described by the tropical Z-R. Without bias correction, the rainfall produced from radar alone would be biased low, requiring approximately a 50% increase to be useful as model input.

As mentioned earlier, the operational system used to support FEWS is capable of rejecting erroneous rain gauge data in online modes of operation. The map of rain gauges refused (or used) is presented in Figure 4.4. The rain gauges refused are mostly due to zero rainfall measured by the rain gauge. Those gauges Not Found would be those with telemetry failure during any period. However, no such loss was detected in this period. The storm total shown in Figure 4.5 highlights the variability of rainfall, where sequential storm cells embedded within TS Hermine trained from south to north over the central part of Austin creating prolonged rainfall with several intense periods. The improvement in rainfall statistical agreement with rain gauges used in operation is seen in Figure 4.6 for the period covered by the storm total. The absolute average difference between radar sampled over each gauge and the gauge accumulation is the 32.1% before and 15.6% after bias adjustment. This accuracy is only an estimate since it is computed from the same gauges

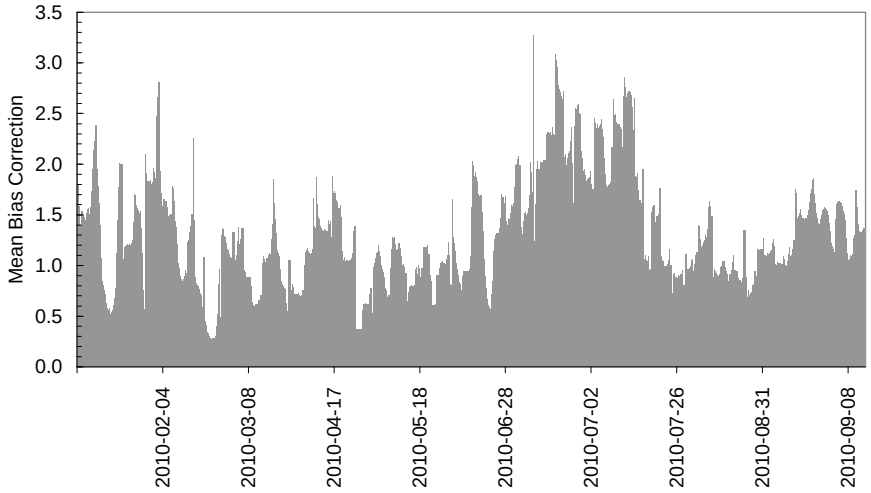

(a)

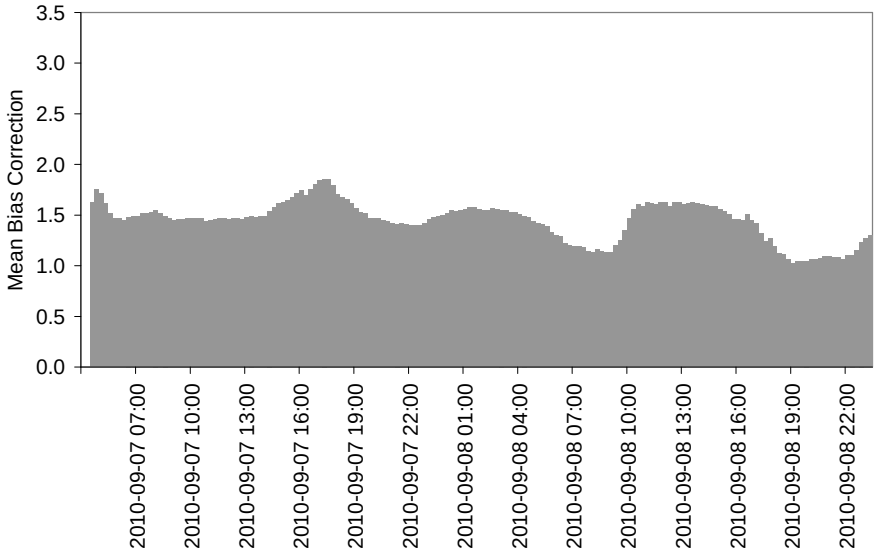

(b)

Figure 4.3: a) Mean bias correction time series from Jan-Sep 2010, b) Event mean bias correction time series, 7-Sep-2010 to 8-Sep-2010

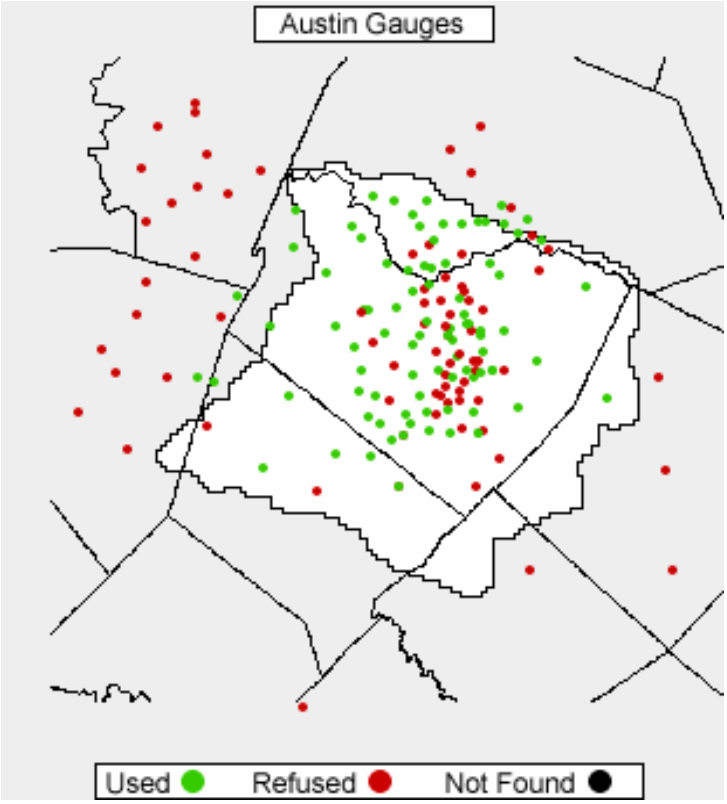

Figure 4.4: Map of rejected and used gauges during the 7-8 Sep-2010 event

used in bias correction. Similar improvement in bias is found for the entire 9-month period.

While operational stream flow forecasts are produced by the V*flo* model using gridded rainfall directly, the basin-averaged rainfall for Bull Creek illustrates the temporal dimension of rainfall during this event seen in Figure 4.7. The most intense rainfall, for the City of Austin, occurred over Bull Creek, between 17:00 and 18:00 hours on 7-Sep 2010. The rainfall during the 6-hour period ending at 3:45 CDT on 8-Sep, contained the greatest gauge accumulation exceeding 203 mm, with a peak rainfall intensity of 70 mm/hr. During this integration period, the mean bias correction was 1.528, which produced

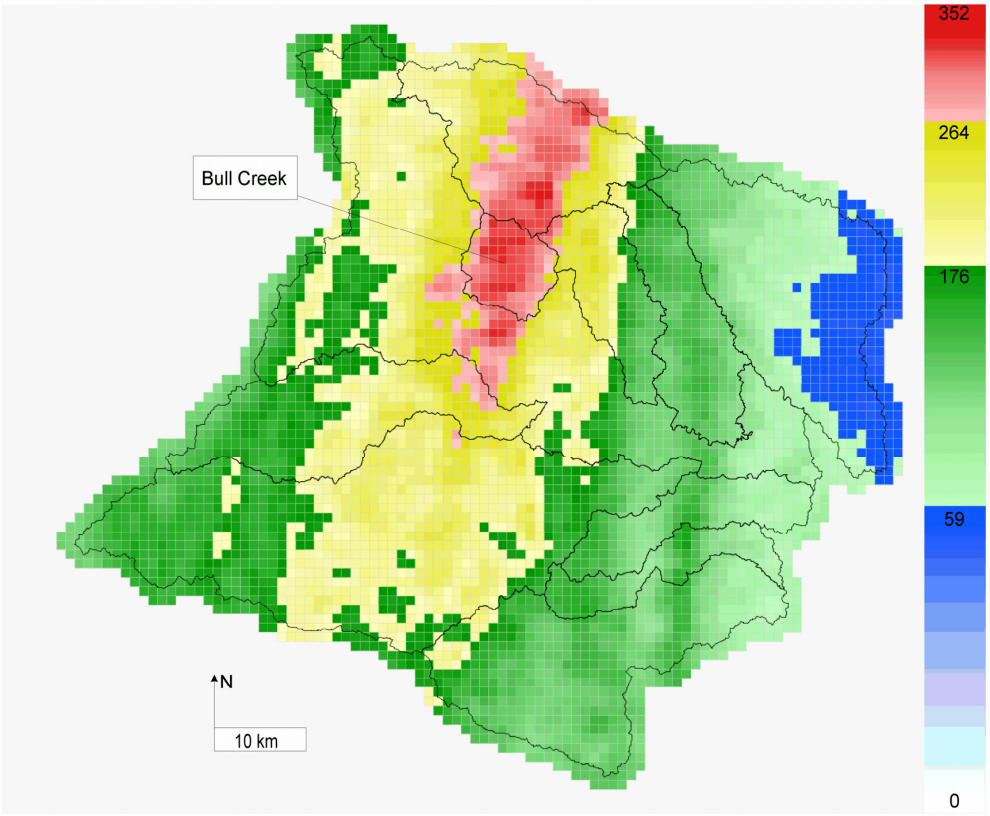

Figure 4.5: Gridded storm total produced by the online system during the 7-8 Sep-2010 event. Rainfall accumulation in mm

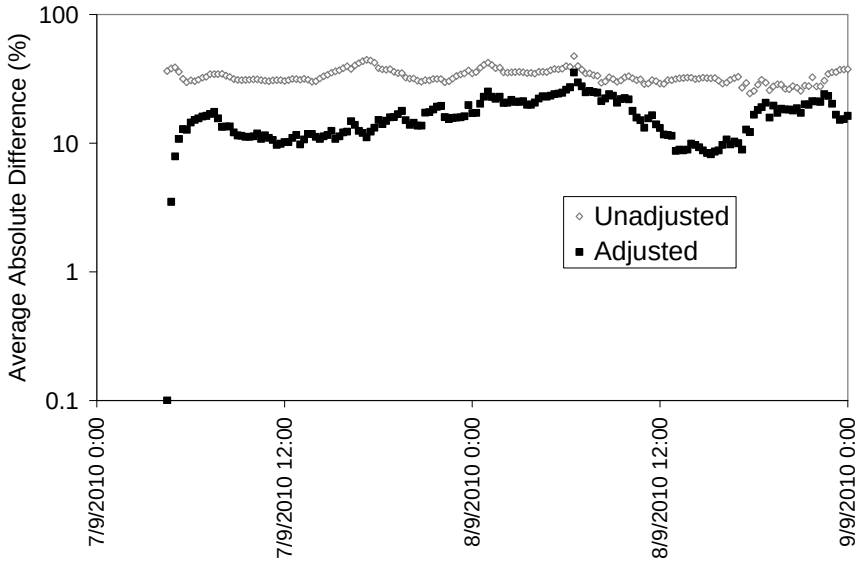

Figure 4.6: Average difference between rain gauge and radar precipitation estimates

an average difference between gauge and radar of +/- 10% computed with 76 of the 164 gauges ingested into the online system.

Figure 4.8 shows the calibration results for the Bull Creek basin. The basin was calibrated using GARR input for four events during the 2007-2010 period. The September 7-8, 2010 event was significantly larger than the calibration events providing a validation event for the Bull Creek model. Besides producing GARR for model input, the system provides a backup product composed only of the rain gauge amounts. Thus, it is important to consider what the accuracy would be had RGO been used during the event. During the 7 - 8 Sep 2010 event, GARR was used solely, and the RGO product is tested through reanalysis.

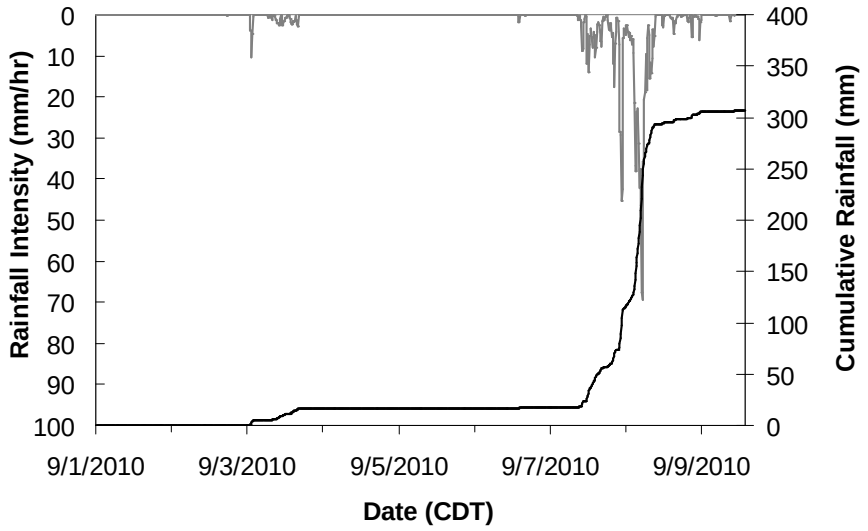

Figure 4.7: Bull Creek radar rainfall estimated intensity and accumulation

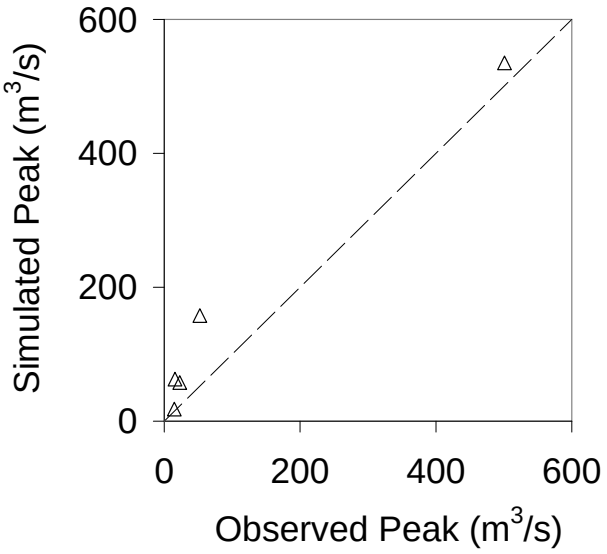

Figure 4.8: Scatterplot of Bull Creek peak discharge prediction

4.4.2 Evaluation of Operational Distributed Flood Forecasting

Two aspects of the flood-forecasting problem were investigated for each rainfall input, 1) prediction accuracy and 2) lead-time. The system must be able to reproduce the observed behavior of stream flow response during an event. A visual inspection of the hydrographs shown in Figure 4.9a-u illustrates the performance of the PBD basin models during the event. The subplots show the reliable correlation between the simulated and observed response during both low and high stage conditions. Watch and warning levels shown are set based on thresholds established by the FEWS staff at critical locations where flooding can occur.

One aspect of a flood warning system is the accuracy attained with precipitation inputs to the operational model. For the presented hydrographs (Figure 4.9a-u), the measured and forecast stage correlation coefficients range from 0.73 to 0.98 for GARR input and from 0.63 to 0.97 for RGO input.

In some cases, both the GARR and RGO produce relatively low correlation coefficients. Figure 4.10 shows the scatterplot of peak stage results using GARR input. In comparison of simulated and observed peak stage using GARR as input, the agreement in terms of the Mean Absolute Difference (MAD) was 0.57 m, with an RMSE of 0.89 m. Thus, radar produced relatively unbiased forecasts with a trendline slope of 1.084. Whereas, with RGO as input, error in peak stage prediction shown in Figure 4.11 shows a doubling of the error where the peak stage MAD is 1.18 m and the RMSE is 1.77 m. The peak stage produced with RGO resulted in a trendline slope of 1.35, or a 27% over prediction had the forecasts been produced with gauge measurements as input rather than GARR.

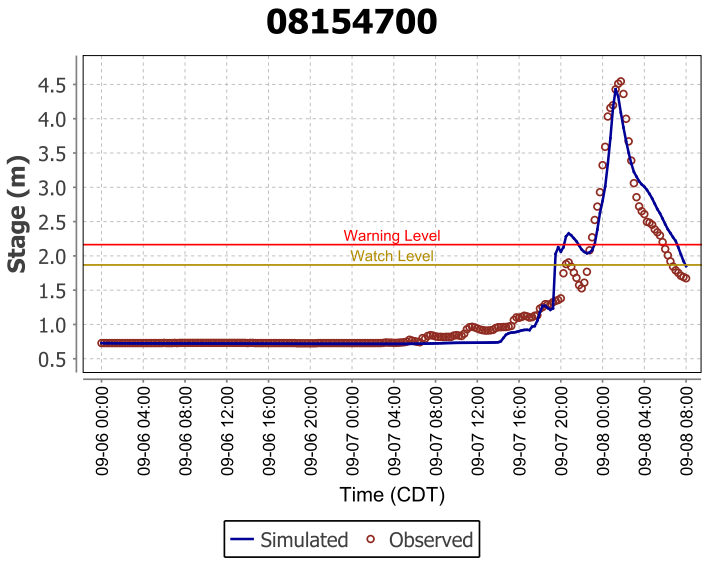

(a)

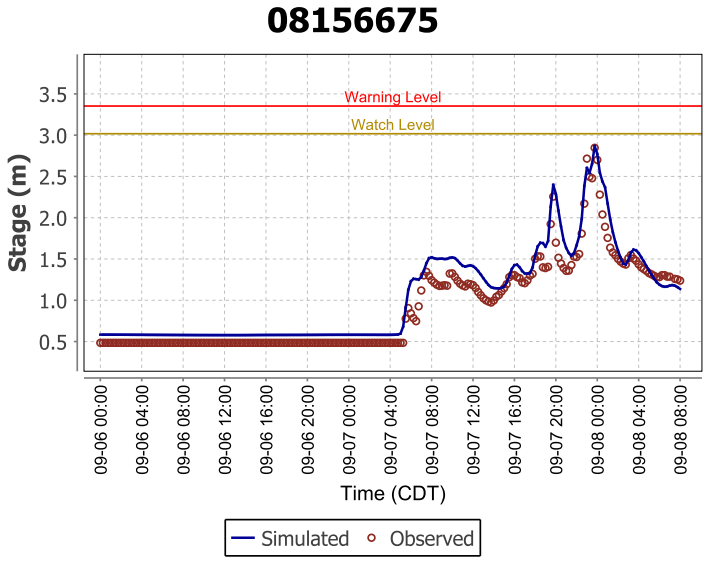

(b)

Figure 4.9: Subplots of forecast and observed stage hydrographs using GARR input

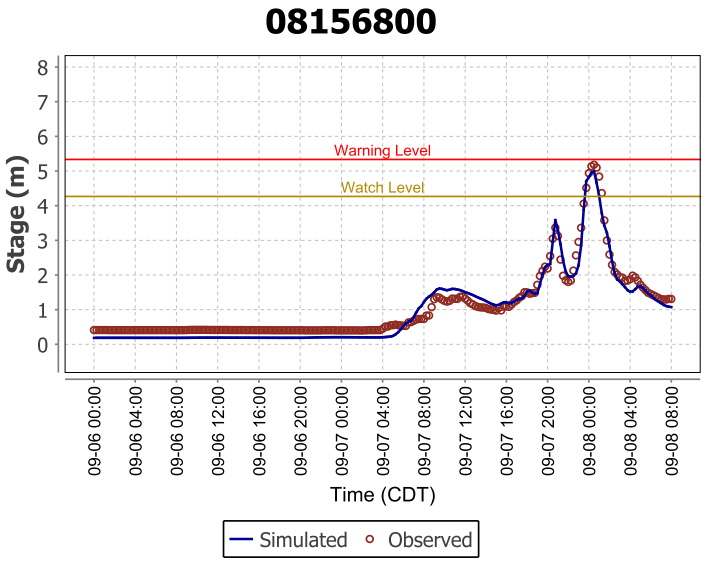

(c)

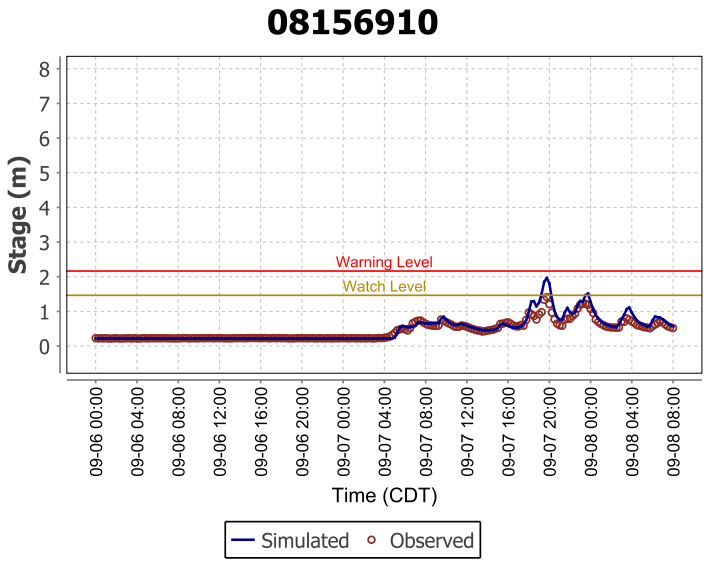

(d)

Figure 4.9: Subplots of forecast and observed stage hydrographs using GARR input

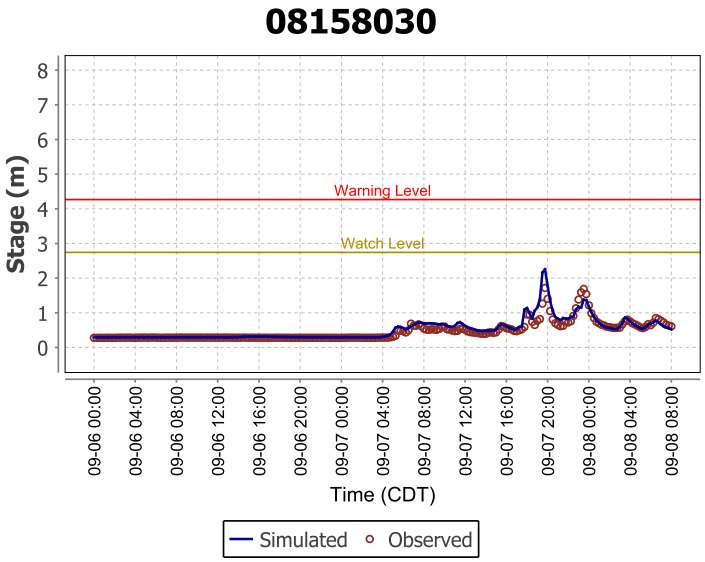

(e)

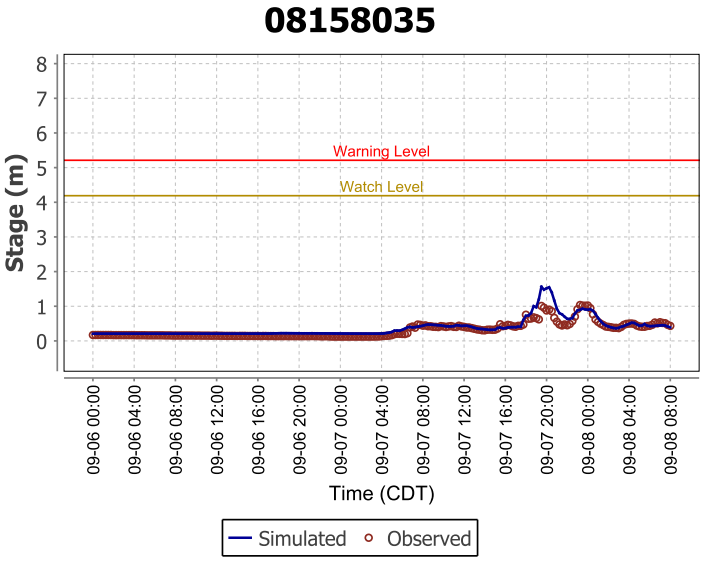

(f)

Figure 4.9: Subplots of forecast and observed stage hydrographs using GARR input

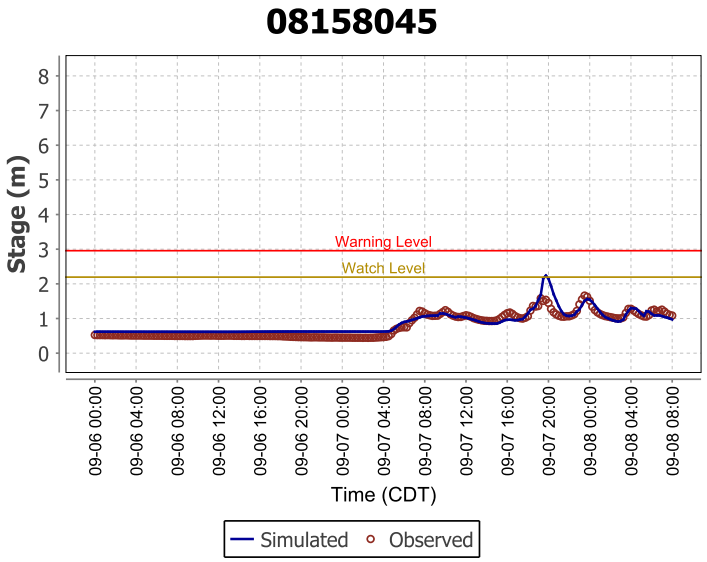

(g)

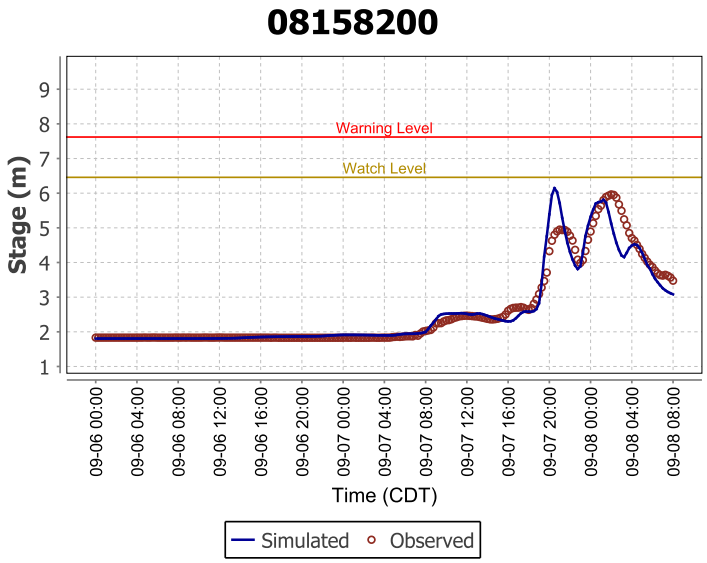

(h)

Figure 4.9: Subplots of forecast and observed stage hydrographs using GARR input

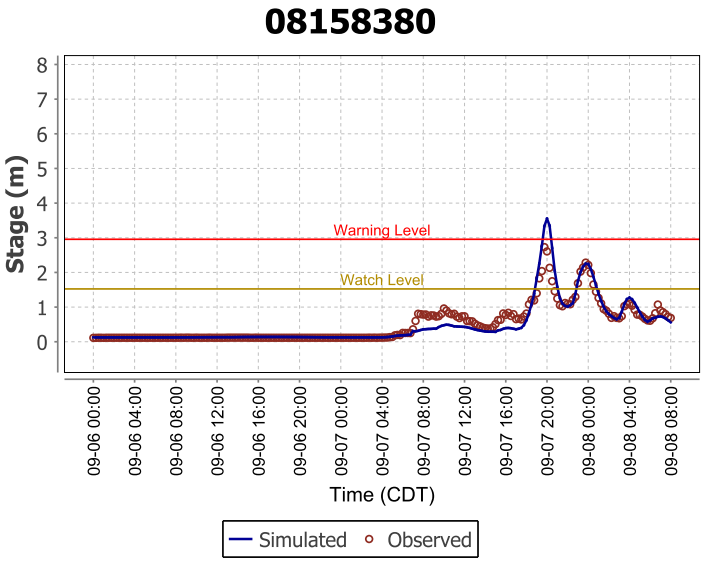

(i)

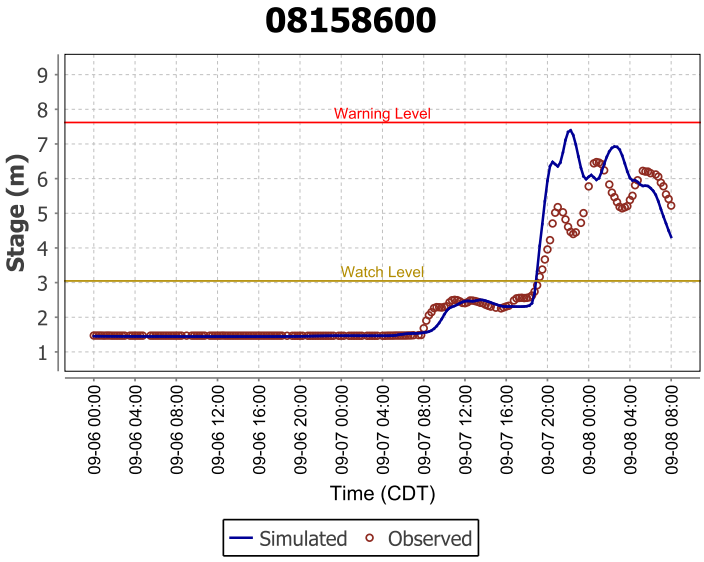

(j)

Figure 4.9: Subplots of forecast and observed stage hydrographs using GARR input

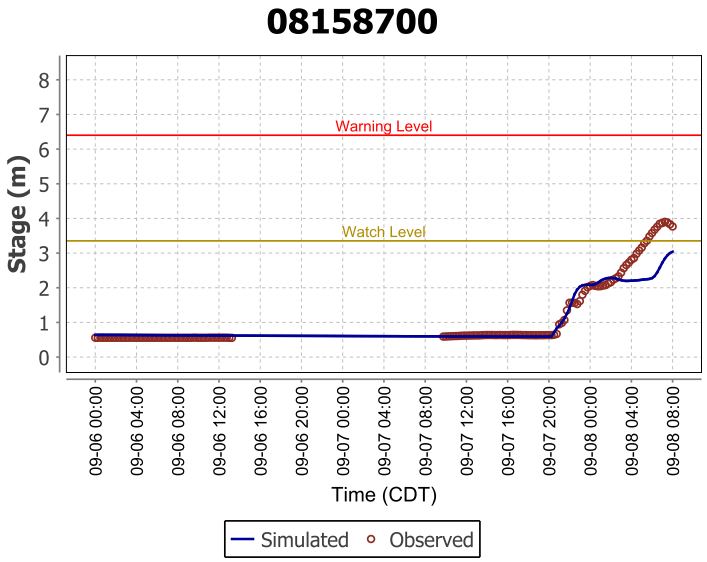

(k)

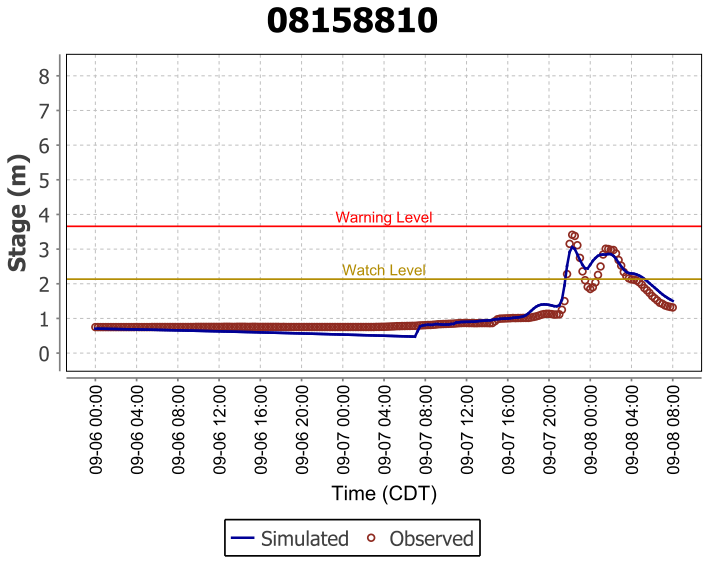

(l)

Figure 4.9: Subplots of forecast and observed stage hydrographs using GARR input

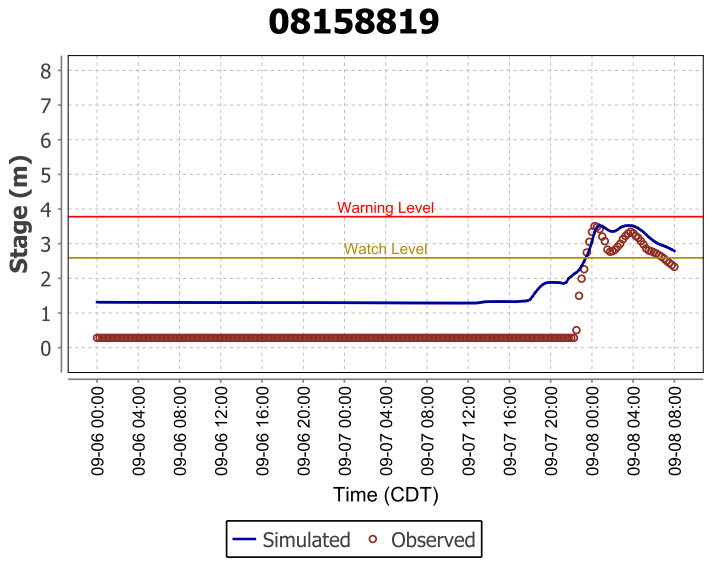

(m)

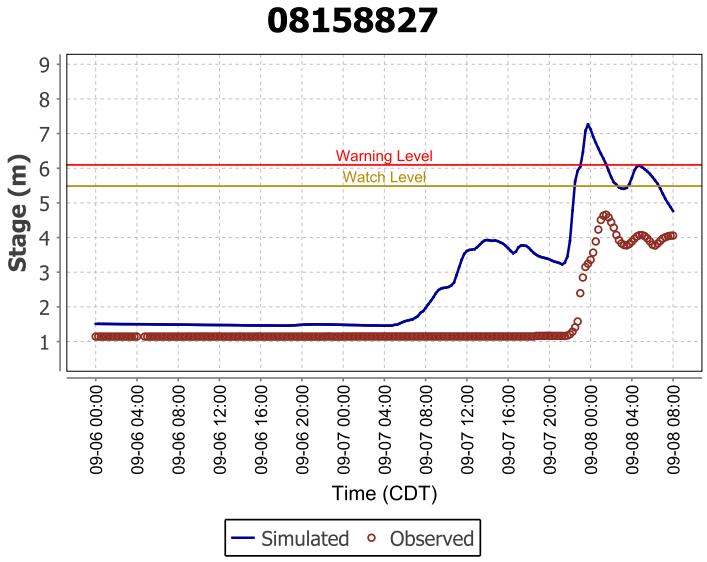

(n)

Figure 4.9: Subplots of forecast and observed stage hydrographs using GARR input

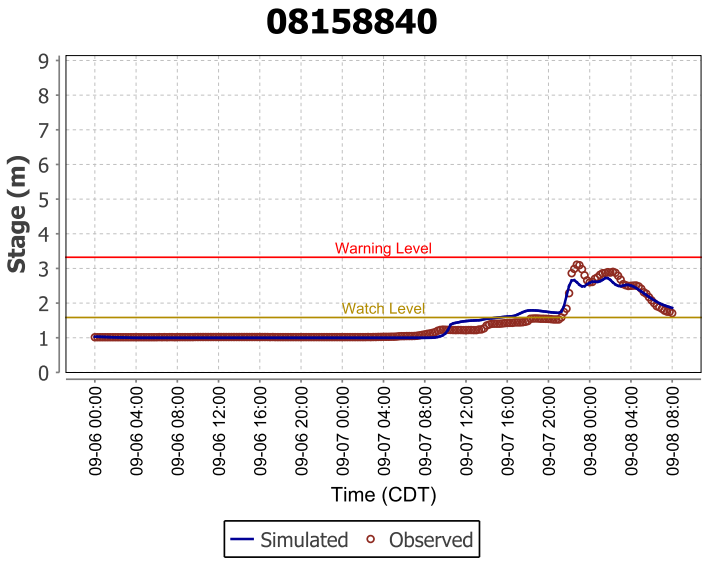

(o)

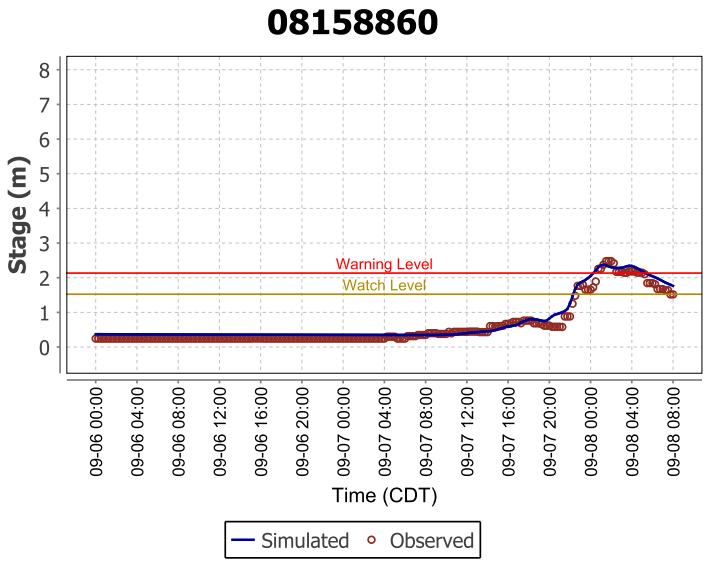

(p)

Figure 4.9: Subplots of forecast and observed stage hydrographs using GARR input

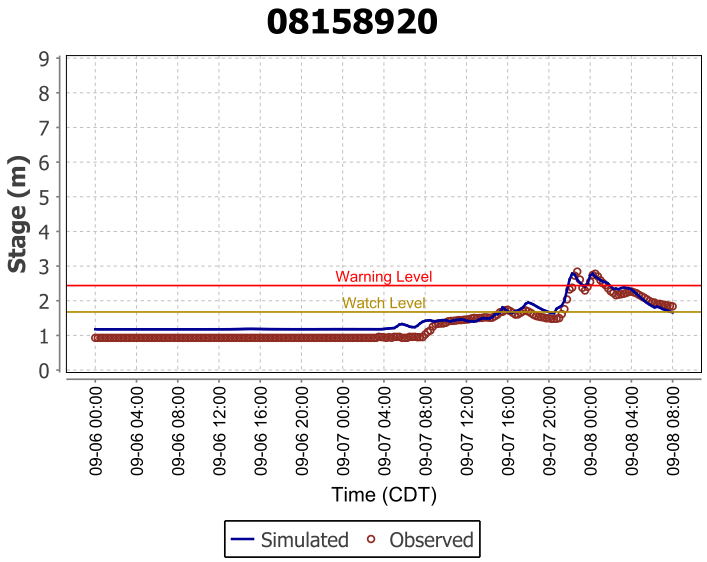

(q)

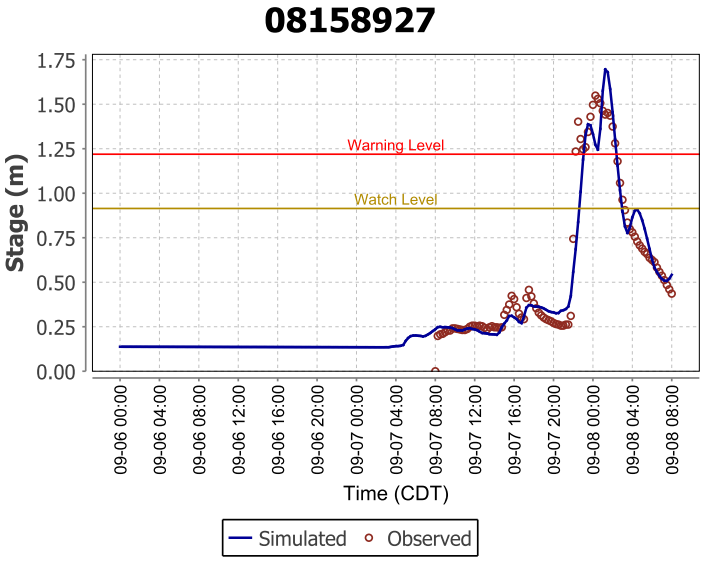

(r)

Figure 4.9: Subplots of forecast and observed stage hydrographs using GARR input

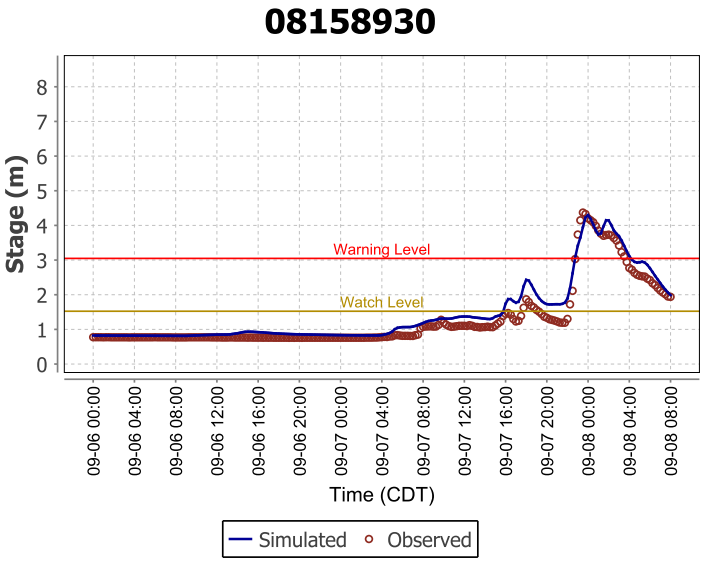

(s)

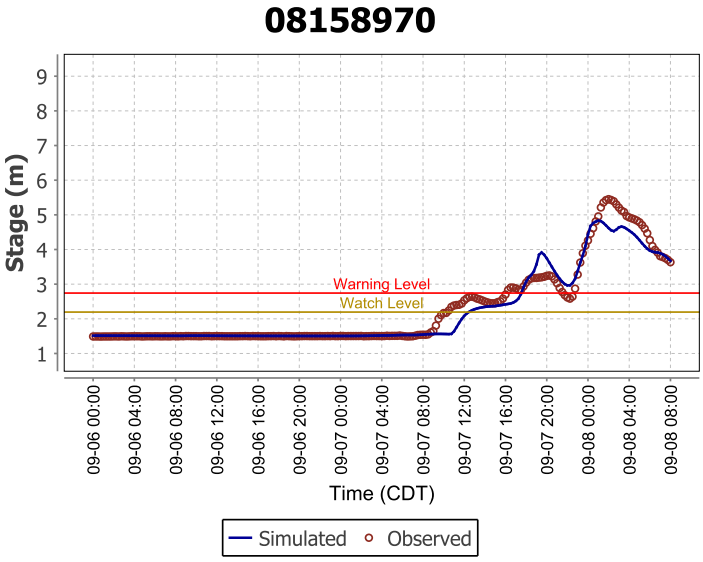

(t)

Figure 4.9: Subplots of forecast and observed stage hydrographs using GARR input

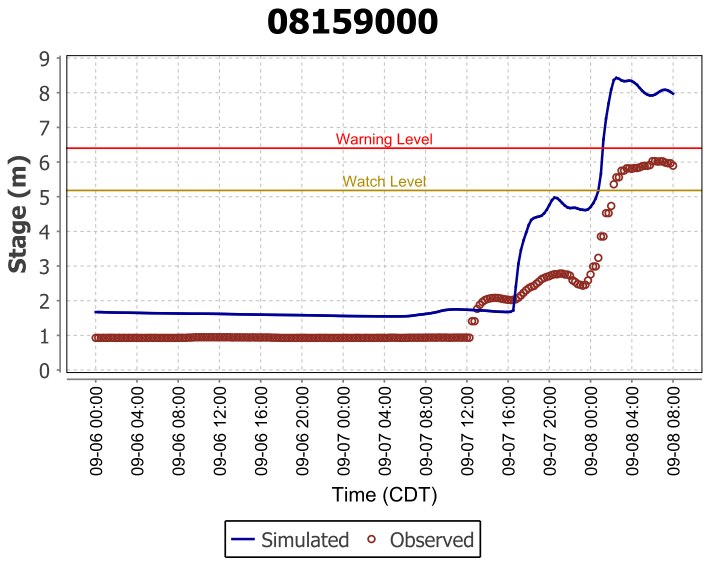

(u)

Figure 4.9: Subplots of forecast and observed stage hydrographs using GARR input

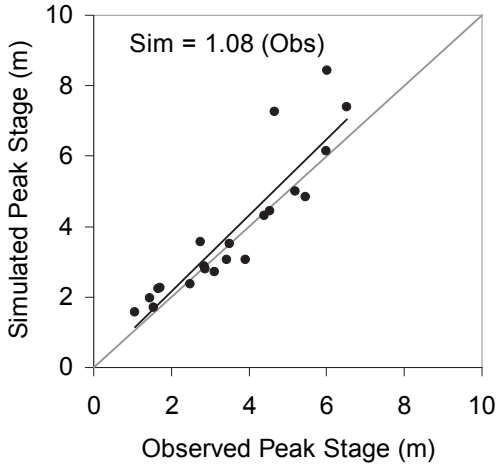

Figure 4.10: Scatterplot of peak stage simulated using GARR input versus the observed stream flow gauges

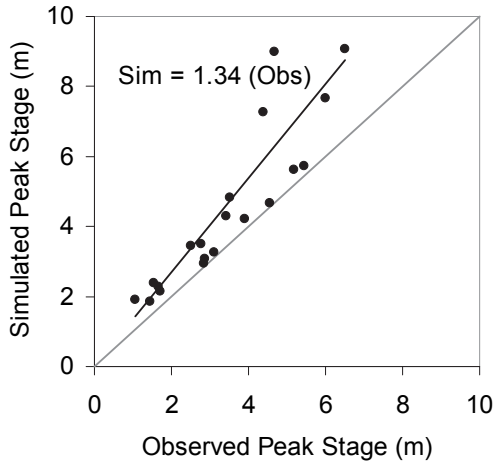

Figure 4.11: Scatterplot of peak stage simulated using RGO input versus the observed stream flow gauges

4.4.2.1 Forecast Lead-Time and Error

In the unattended system, the lead-time is determined by the hydraulic response of the system. In this case, lead-time is the time between generation of a forecast with detected rainfall until the time when forecast stage exceeds the flood warning level. Using both RGO and GARR, lead-time was calculated for all of the 222 forecast locations. Many of these locations are ungauged so there is not a measurement of when actual flooding occurred. Because lead-time is critical for taking emergency action, it is evaluated here to determine whether radar offers some advantages as opposed to a rain gauge-only system. The difference between lead-times produced by GARR and RGO is assessed as,

$$\Delta = T_L^R - T_L^G \tag{4.6}$$

where Δ is the difference between GARR lead-time, T_L^R, and RGO lead-time, T_L^G. To visualize the shift in lead-time gained using GARR, the histogram of

Δ is shown in Figure 4.12. The mode of the histogram lies between 0.25 - 0.5 hours meaning that forecasts based on radar (GARR) were ahead of forecasts based on rain gauge (RGO). The maximum lead-time of 3 hours occurred in Onion Creek, which is the largest basin simulated ($>$ 300 sq. km). There were two locations where the lead-time from RGO exceeded the lead-time achieved with GARR input.

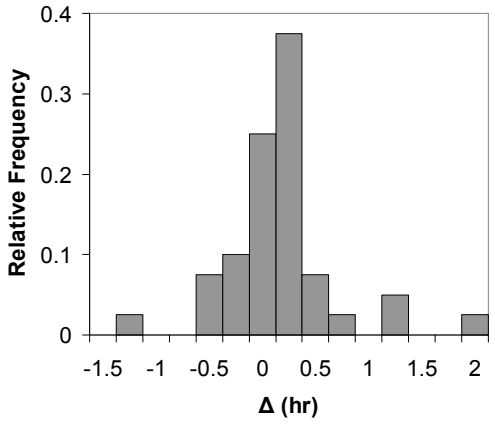

Figure 4.12: Histogram of differences between GARR and RGO lead-time

While the lead-time is the difference between two predicted quantities, comparison with observed stream flow was possible at six locations where flooding was both predicted to occur and actually did so. Forecast timing error, ϵ, is defined as,

$$\epsilon = |T_{sim} - T_{obs}| \tag{4.7}$$

where T_{sim} is the simulated flooding time and T_{obs} is the observed flooding time. During the 7-8 Sep 2010 event, there were six stage gauges where flooding exceeded flood stage. The timing error for RGO and GARR input is shown

in Figure 4.13. While the GARR forecast lead-time error at 08154700 was larger than expected, the median GARR timing error was less than 30 minutes excluding this location. The median timing error considering RGO as input was 2.42 hours, or about 4.8 times that of GARR. Thus, compared to observed stage, timing error was reduced by 1.9 hr (2.4-0.5) using GARR as input rather than RGO.

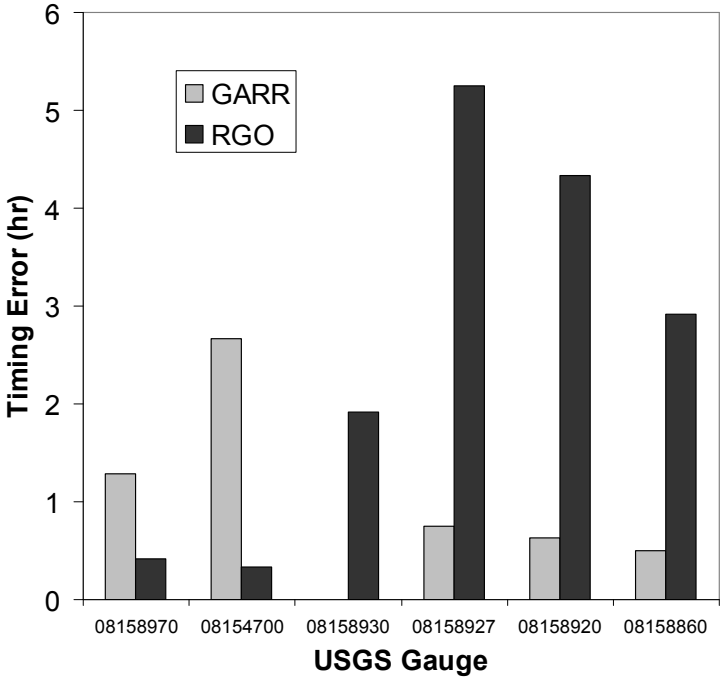

Figure 4.13: Flooding timing error for each rainfall input at USGS gauges where flooding occurred

4.4.2.2 Forecast Accuracy

Another measure of simulation accuracy between GARR and RGO inputs is the Nash-Sutcliffe Efficiency (NSE) evaluated during the event from 15-minute discharge values. Figure 4.14 shows a boxplot of NSE values together with the key points of the probability density function. The y-axis scale is broken from -3 to -10 since no data points fall in this range. The box portion contains the inner quartile range (IQR) of the distribution while the whiskers are 1.5*IQR. The median NSE for GARR was 0.78 while the median NSE for RGO was -0.51. The majority (86%) of NSE for GARR are greater than zero while only 24% of NSE for RGO are greater than zero. There are four points for the GARR input that are below the bottom whisker, which indicates these data points as possible outliers. The y-axis scale is broken between -4 and -20 to show the two outliers for the RGO input. These outliers correspond to the points along the main stem of the Onion Creek basin. The Onion Creek basin is located near the city limits where rain gauge density is reduced.

Analysis of the hydrograph response seen in the individual plots in Figure 4.9a-u illustrates the range of model performance that was achieved by each input. Figure 4.15 shows representative hydrographs that correspond to the upper (Q3) and lower (Q1) quartiles of the NSE probability distribution with RGO and GARR inputs. With GARR input, the finer scale shape of the hydrologic response is better represented than the RGO input, which tends to dampen the variability in hydrologic response. Figure 4.16 shows the impact of rain gauge density on simulated hydrograph accuracy measured by NSE. As the area per rain gauge increases, the accuracy of simulated hydrographs decreases significantly for the RGO input. However, the NSE for simulated

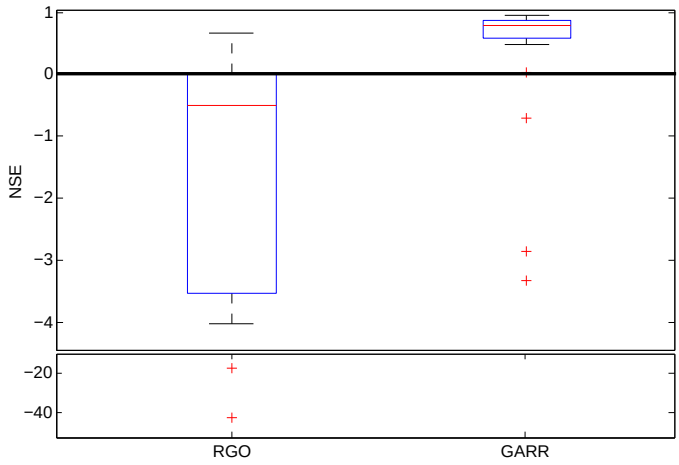

Figure 4.14: Boxplot of Nash Sutcliffe Efficiency for rain gauge only (RGO) and gauge adjusted radar rainfall (GARR) inputs to the City of Austin V*flo* models.

hydrographs generated using the GARR input is uniformly above zero up to a gauge density of one per 321 km^2. However, the accuracy that would be obtained if RGO were used as input is uniformly at or below zero (negative NSE), and tends to decrease sharply for gauge densities above one per 61 km^2. In addition, the variance produced from RGO input starts to increase rapidly above this threshold, whereas the GARR prediction accuracy and its variance is relatively stable across densities described by area per gauge in Figure 4.16. The predictive stage accuracy resulting from use of RGO grows with the area per gauge about 7 times faster than with radar as input, witnessed by the trendline coefficient multiplying area per gauge of -0.0046 and -0.0322, for GARR and RGO input, respectively.

For purposes of comparing the forecast stage accuracy from GARR used in real-time and RGO in re-analysis, the absolute average difference of forecast stage for each input is computed for the values in Figures 4.10 and 4.11.

Recall that the accuracy of the GARR input is estimated by comparing the radar sampled at the rain gauge locations. The absolute average difference after bias correction was 15.6% during this event. Using the GARR as input, the accuracy of peak stage forecasts was 17.7%, while the average difference declines to only 27.6% with RGO.

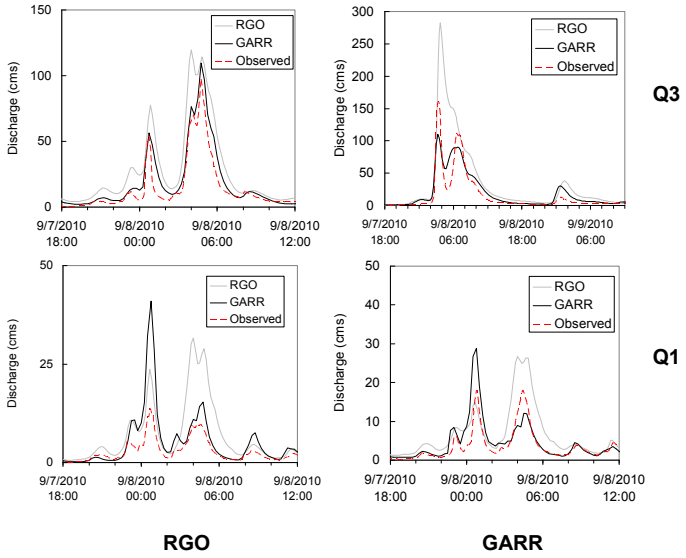

Figure 4.15: Simulated hydrographs representative of the upper (top) and lower (bottom) quartiles of the NSE probability distribution for RGO (left) and GARR (right) inputs.

4.5 Discussion

The September 7-8, 2010 event provided verification of the flash flood forecasting system. During this event, the accuracy of the bias corrected radar input is 15.6% compared to gauge accumulations, which is a 51% improvement over unadjusted radar. Rainfall input accuracy is a principal determinant of hydrologic prediction accuracy as evidenced by the resulting peak stage and timing accuracy. If only RGO were used, a higher density of rain gauges would

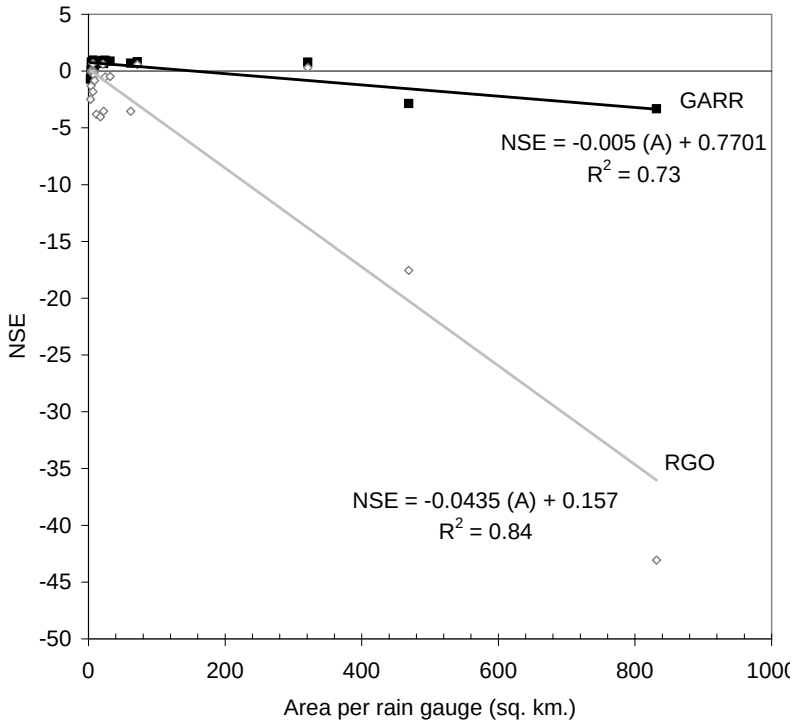

Figure 4.16: Nash Sutcliffe Efficiency compared by rain gauge density.

be required to achieve the same simulated hydrograph accuracy delivered by the GARR input. In fact, using the RGO input, the gauge density required to achieve equivalent accuracy to the GARR input is approximately 5 times denser. The predictive stream flow accuracy using RGO input diminishes with rain gauge density about 7 times faster than with the GARR input.

Bias correction of the radar product resulted in better agreement with rain gauge point measurements with an estimated average difference of 15.6%. With GARR as input, the forecast stage accuracy of 17.7% is comparable to the accuracy of the input. However, while RGO can produce some acceptable results where the density is high, forecast stage accuracy declines with the sparseness of the rain gauge network.

The scatterplots and boxplots between rainfall inputs indicated that there

are possible outliers in modeled stream flow accuracy. The main two outliers were USGS gauge 08158827 (A=469 km^2 per rain gauge) and 08159000 (A=831 km^2 per rain gauge). These gauges are located in the Onion Creek basin, which extend beyond the City limits and have sparse rain-gauge coverage for use in radar bias correction or for RGO input. While the NSE for these forecast points is strongly correlated with the rain gauge density, there are additional reasons that could be causing a loss of simulated stream flow accuracy in the Onion Creek basin. The Edwards Aquifer is a Karst recharge zone that crosses the middle portions of the basin. Model structural errors in this zone could also lead to the decrease in accuracy, especially since neither RGO nor GARR produce accurate results in this watershed.

It is interesting to note that while the models were calibrated using lower-flow events, during the extreme event, the accuracy was quite good with a median NSE near 0.8 using GARR as input. During extreme events, the soil properties may not be affecting the runoff and hence the prediction accuracy due to saturation. Thus, when the soil porosity is completely filled, the accuracy of the forecast stage may be more dependent on rainfall accuracy than factors controlling infiltration. From the extreme event on September 7-8, 2010 that forced so many stream levels above flood stage, insight was gained from the re-analysis of RGO in terms of the gauge density and its effect on forecast stage accuracy. The timing error was reduced by 1.9 hr (2.4-0.5) using GARR as input rather than RGO. The use of GARR improved the accuracy in both forecast lead-time and peak stage across a range of basin sizes and rain gauge densities.

4.6 Summary

The integration of radar with rain gauges and a PBD model showed more accurate hydrologic prediction than could be achieved using rain gauge only input during a recent flash flood event. Radar rainfall that is quality controlled and bias-corrected in real-time is valuable for monitoring of evolving precipitation and storm threats. Besides storm thresholds, GARR also serves as distributed input to a real-time PBD model that forecasts flooding in urban watersheds within City of Austin. Distributed flash flood forecasts allow decisions to be made as complex variable rainfall evolves over watersheds that range from headwaters to major streams. During a recent severe storm, the PBD approach to flash flood forecasting allowed emergency responders to close bridges and street intersections based on reliable forecast stage information. Through re-analysis, closer agreement between predicted and observed stage was possible using the GARR input rather than RGO input. Further, the timing error of forecast stage versus observed stage was reduced by 80% using GARR input compared to RGO input. From evaluation of forecast accuracy, it was found that the rain gauge density required to achieve equivalent accuracy to the GARR input is approximately 5 times denser, and that the predictive stream flow accuracy using RGO input diminishes with rain gauge density about 7 times faster than with the GARR input. The use of GARR as input to the PBD model not only increases the forecast lead-time and its accuracy, but also the accuracy of forecast peak stage across a range of basin sizes and with variable rain gauge densities used in real-time for radar bias correction. Useful lead-time and accurate forecast stage distributed throughout an urban area was obtained from the radar-based distributed flash flood

forecasting system. These results show that forecasting is even more sensitive to input uncertainty, particularly lead-time available to take precautionary actions. Whereas in retrospective evaluations, inputs can be adjusted and accuracy enhanced, the opportunity to do so in real-time is more limited, but important for accurate model results.

Chapter 5

Distributed Hydrological Forecast Reliability using Next Generation Radar

5.1 Abstract

[1] Stormwater runoff can significantly impact flooding in urban areas. Flood prediction depends on model structure uncertainties and the accurate determination of rainfall. Three aspects of hydrologic forecasting in real-time and hydrologic predictions in offline modes include: 1) distributed model reliability, 2) accuracy of radar derived rainfall, and 3) scaling of basin input and response. An existing flood alert system (FAS) that is operational for Brays Bayou in Houston, Texas forms the basis for testing the relative magnitudes of these effects on prediction accuracy. The importance of gauge-corrected radar input was demonstrated through a probabilistic approach and by comparison to events with streamflow observations. The difference in discharge, called dispersion, obtained from corrected and uncorrected radar input scales with drainage area, but at a nonlinear rate and differs from storm to storm. An additional comparison was made between the existing flood alert system's kinematic wave model, V*flo*, and the full dynamic wave model, HEC-RAS. Both models showed similar scaling with radar bias correction. Considering

[1] Adapted version of Looper, J. P., and Vieux, B. E. (2013). Distributed Hydrologic Forecast Reliability Using Next-Generation Radar. *Journal of Hydrologic Engineering*, 18(2), 260-268.

that random errors in rainfall rates measured by radar should cancel out over large areas, the decline in forecast skill measured by the critical success index (CSI) was not intuitive. Both empirical observations and the perturbation experiment confirm that predictability decreased with increased drainage area. This article shows the benefit of accurate radar rainfall, but that predictability does not follow linear scaling across a range of drainage areas.

5.2 Introduction

Considerable attention has been focused recently on radar hydrology, and its quantitative application in hydrologic modeling. Offline evaluation of hydrologic model prediction accuracy using archival radar and/or gauge data is a necessary step for improving operational use in real-time forecasting. These evaluations also provide opportunities to investigate the predictability of distributed hydrologic models used for decision making. The combination of distributed hydrologic modeling with high-resolution rainfall input derived from radar and gauge observations, offers the potential for gaining insight into how prediction accuracy scales with drainage area. Of particular importance is an understanding of how corrections made to radar rainfall input affect uncertainty in hydrologic predictions, and how it scales with drainage area.

5.2.1 Hydrologic Predictability

How predictable a natural system is defines whether a combination of modeling and observations can produce reliable forecasts of system behavior. Three factors influencing predictability and limits to prediction were identified (NRC-COHS, 2000), 1) Sensitivity to initial conditions 2) Sensitivity to boundary

conditions 3) Impact of scaling on predictability The third type of predictability addresses the scaling response of a basin due to the heterogeneity of land cover, topography, drainage network, and precipitation. Because of this scaling behavior, spatial and temporal averages do not necessarily result in more predictable model performance due to strong transitions or changes in characteristics (NRC-COHS, 2000 p. 13ff).

This investigation focuses on the third type of predictability. This study identifies streamflow prediction accuracy using radar as input to a distributed hydrologic model. The objectives of this study are, 1) How accurately can a radar-based distributed flood forecasting system make predictions with and without gauge-correction? 2) How much improvement is achieved through gauge correction of the radar derived QPE? 3) Does the predictability and improvement in prediction accuracy achieved through gauge-correction scale linearly or nonlinearly with drainage area?

5.2.2 Study Area

The Brays Bayou watershed is located within the corporate limits of Houston, Texas. The watershed is fully urbanized with impervious surfaces averaging 40%. Within the watershed, urban impervious surfaces cover soils that are generally of clay texture with hydraulic conductivities on the order of 1 mm/hr (0.04 in/hr). These soil and land cover conditions make soil moisture and infiltration rates insignificant compared to rainfall rates encountered during most storms. Therefore, the effects of soil infiltration and moisture on the transformation of rainfall into runoff are insignificant. The topography of Brays Bayou is typical of coastal plains particularly along the Gulf Coast, with overland and channel slopes averaging less than 1% (Bedient et al., 2003). Be-

cause this basin is essentially impervious, it is useful for hydrologic evaluation of radar input (Vieux and Bedient, 2004). Observed streamflow in this basin is derived from the interior gauging stations operated by the United States Geologic Survey (USGS) at two locations, the Main Street gauge 08075000 with 245.8 km^2 (94.9 mi2), and upstream at the Gessner gauge 08074810, with 136.0 km^2 (52.5 mi2).

5.2.3 Flood Alert System

Use of a physics-based distributed model, for operational flood forecasting in Brays Bayou, is described in Bedient et al. (2003) and Vieux et al. (2004). The PBD model called, V*flo*, is a distributed hydrologic model that solves two state variables, soil moisture, and runoff distributed throughout the drainage network composed of channel and overland flow grid cells. The kinematic wave analogy is solved using the finite element method in space and the finite difference method in time (Vieux, 2004). Detailed geospatial data is used to setup and calibrate the model. The distributed model has been calibrated and produces reliable results (Vieux and Bedient, 2004), and is used herein to test quantitative precipitation estimates (QPE) derived from radar.

The configuration of radar and rain gauge network, for the Brays Bayou study area, provides high resolution gauge-corrected radar input to the model. Two sources of input are considered here: 1) archived radar rainfall from the Flood Alert System (FAS), and 2) gauge-corrected radar using quality controlled rain gauge data to correct radar bias. The FAS system uses NWS radar data (Level 2) from the nearby NEXRAD radar (KHGX), which is located approximately 50 km away from the center of Brays Bayou. The rain gauge network is operated by a local authority (HCOEM) for emergency man-

agement purposes. Figure 5.1 shows the sample locations for evaluating hydrologic model response, the stream gauges operational in Brays Bayou, and channel network of the basins used to test the hypotheses in this study. The main channel of Brays Bayou flows from southwest in an easterly direction in the lower right portion of the map in Figure 5.1 . The spatial distribution of rain gauges is approximately 84 km^2 per rain gauge. For purposes of testing runoff sensitivity, 22 sample locations are chosen within the basin that range in size from 6 to 310 km^2.

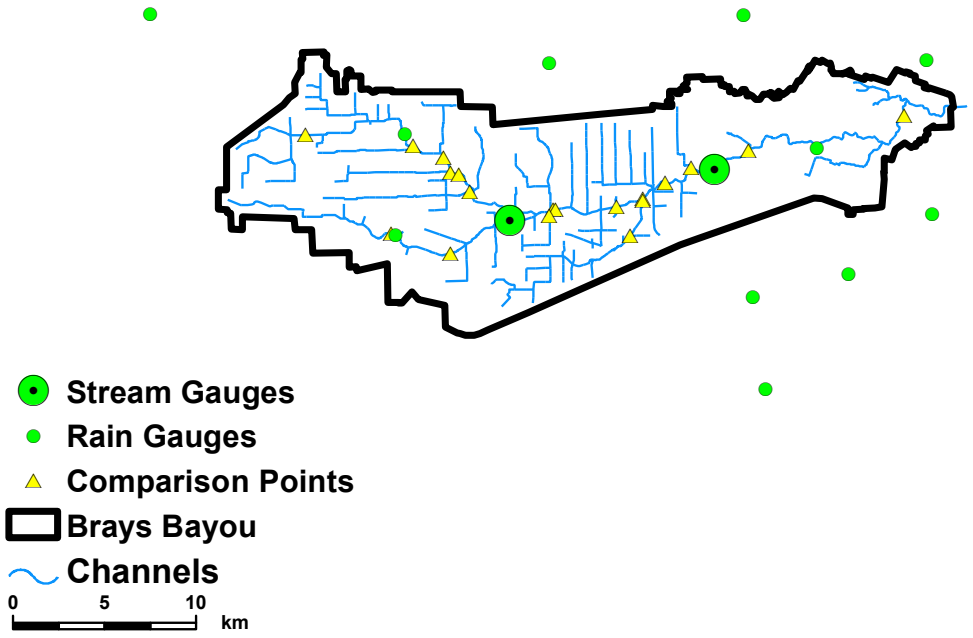

Figure 5.1: Layout of basin, channels, and comparison points (watch points) used for experiment

5.2.4 Radar Rainfall Uncertainty

Uncertainties in radar rainfall estimates used as input to hydrologic models can affect the accuracy of both offline prediction (post-analysis) and online forecast (real-time) applications, as observed by Carpenter and Georgakakos (2004) who considered ensemble streamflow forecasting in larger river basins where presumably there is less control over the radar bias and sparse rain gauge networks. The uncertainty inherent in precipitation derived from radar has been well established as having both random and systematic (bias) components, as described by Wilson and Brandes (1979), Doviak and Zrnic (1993) among others. It is also supposed that random error in the radar rainfall estimates, e.g. those caused by updrafts and downdrafts, should cancel out over catchment areas of sufficient size. Disparities in the representativeness of measurements of each sensor can cause disagreement between rainfall measurements made by gauges and radar, as found by Ciach et al. (2003, 2006), Chumchean et al. (2003), and Habib et al. (2004). Mandapaka et al. (2009) estimated the spatial correlation distance to be about 20 km, which can increase uncertainty in rainfall estimates derived from combinations of gauge and radar. Effort expended on error separation to account for differences between rain gauge and radar measurements is important for understanding why observations from these sensors differ and where these errors come from. Beyond the uncertainty in point-area rainfall estimation, from a hydrologic perspective, understanding is needed on how these errors feed forward into hydrologic prediction and forecasting, whether they average out, or if there is scale dependency across catchment areas.

Conversion of reflectivity to rainfall rate is accomplished using a Z-R re-

lationship that depends on the number and size of raindrops (Marshall and Palmer, 1948). However, among the many sources of uncertainty, error can be introduced due to differences between the assumed drop size distribution (DSD) in a given Z-R relationship and the actual storm DSD. Considerable reduction in radar rainfall uncertainty can be achieved through bias correction using rain gauges (Wilson and Brandes, 1979). The factors affecting radar rainfall accuracy, and the improvement achieved through bias correction using rain gauges are described by Chumchean et al. (2003), Morin et al. (1995), Rosenfeld et al. (1993, 1994), Smith et al. (1996), Seo et al. (1999), Sanchez-Diezma, et al. (2001), and Vieux and Vieux (2005a, 2005b).

Interest in characterizing radar adjustment techniques has accelerated with the advent of distributed hydrologic models that are capable of integrating the spatially distributed rainfall information (Gourley and Vieux, 2005, Habib et al., 2008). Use of gauge-adjusted weather radar for hydraulic modeling of sewer systems is becoming well established (Einfalt et al., 2005). An overview of the hydrologic requirements for weather radar used in urban drainage is described by Einfalt et al. (2004), who identified the radar processing requirements for hydrologic applications of various weather radar systems in Germany and the United States. Vieux and Bedient (2004) demonstrated the importance of gauge-correction of radar, and the achievable streamflow accuracy of distributed model predictions. In spite of point-area errors, it was found that gauge-corrected radar rainfall produced rainfall (input) agreed with measured streamflow (output) with a correlation coefficient of 0.94 for a single basin outlet location, i.e. the USGS stream gauge 08075000 in Brays Bayou, whereas, uncorrected radar produced much poorer agreement with streamflow. Even with high quality bias-corrected radar rainfall and a well characterized basin,

uncertainty in the rainfall estimates can still persist and create prediction error. Quantifying how this uncertainty in radar input propagates forward and scales in a distributed model is described in the next section.

5.3 Methodology

5.3.1 Model Overview

The distributed model, V*flo*, is used to test the sensitivity and scaling of radar rainfall uncertainties (Vieux, 2004). This model represents the watershed response using a drainage network composed of channel and overland flow cells of regular size. The kinematic wave equations are solved numerically for the drainage network based on conservation equations. The overland flow depth, h, depends on flow from upslope areas, infiltration, I; rainfall intensity, R; land surface slope, and hydraulic roughness. The kinematic wave equation in terms of overland flow depth is,

$$\frac{\partial h}{\partial t} + \frac{S^{1/2}}{\eta}\frac{\partial h^{5/3}}{\partial x} = R - I \tag{5.1}$$

where S is the land surface slope, η is the Manning's roughness coefficient, R is rainfall rate derived from radar rates sampled into each model grid, and the distance, x, is measured from one cell to the next. Eq. 5.1 is modified for channel cells to represent flow area in trapezoidal cross-sections, surveyed cross-sections, or by means of a stage-discharge rating curve. The runoff in each grid cell is modeled as saturation excess, or as infiltration rate excess runoff. When the soil profile becomes saturated, rainfall becomes saturation excess runoff. In the reconstruction of historical storm events, the initial degree

of saturation can be based on antecedent conditions, or derived from continuous simulation in cases where the antecedent soil moisture is a significant influence on basin response.

The V*flo* model is setup for Brays Bayou at a 120-m resolution, which is the same resolution used in the online V*flo* flood forecasting system for this basin, and offline for evaluation of prediction accuracy. The basin model, in combination with radar input, serves as a test bed for evaluating hydrologic forecast ability, and for identifying the limitations posed by radar rainfall accuracy. Evaluation of runoff volume from the basin was measured by integration of streamflow hydrographs and compared to gauge-corrected radar input. From comparison of input to output volumes, approximately 7% of the rainfall input infiltrated from the surface water system. Thus, the basin is essentially impervious, making it useful for hydrologic evaluation of radar input.

5.3.2 Radar Rainfall Processing

Operationally, the FAS processes NEXRAD radar at a 1x1 km resolution through a real-time correction scheme to reduce systematic errors (bias). The system computes a running total of radar, R, and gauge, G, accumulations over a 6-hour period with 15-minute updates. Appropriate Z-R relationships are applied seasonally or for major storms through human interaction. The system then applies a spatially variable bias correction factor. The mean of these bias correction factors is referred to as the MFB based on qualified rain-gauge accumulations. The MFB correction factor applied to the radar rainfall is defined as,

$$MFB = \frac{\sum_{i=1}^{n} G_i}{\sum_{i=1}^{n} R_i} \tag{5.2}$$

where G_i is the gauge accumulation; and R_i is the radar accumulation for each radar-gauge pair. Each pair is automatically screened using a minimum storm total threshold (MSTT) check. Further, any radar-gauge pair whose radar or gauge event sum totals less than 0.10 inches is removed from analysis for that event. The quality control identifies upper and lower control limits calculated to identify statistical outliers. Any pair whose individual bias (G/R) or average difference, AD, value that is in excess of 3 standard deviations of the mean is considered an outlier and discarded from analysis during an event and in operation. The agreement between gauge and corrected-radar accumulation is computed as the average difference, AD,

$$AD = \frac{100}{n} \sum_{i=1}^{n} \frac{G_i - (MFB \times R_i)}{G_i} \tag{5.3}$$

where the terms are as previously defined. Once the radar data is bias corrected by the MFB, there remains random error associated with updrafts, downdrafts or point-area differences, which suggests that AD is almost never zero. Because understanding the uncertainty associated with flood forecasting is the main goal of this study, we select extreme events with heavy precipitation known to cause localized or major flooding, whereas, the time series of MFB factors are derived from the automated flood alert system (FAS). The statistical characteristics of the selected events are shown in Table 5.1. We will use the archival time series of MFB factors to derive the probability distribution function (PDF).

Table 5.1: Rainfall event probability distribution parameters

		Gamma Distribution Parameters	
Event	**Mean Field Bias**	α	β
TSA1	1.08	33.8	0.032
TSA2	0.44	11.3	0.039
TSA3	0.69	68.3	0.01
FRANCES	1.48	26	0.057
8/15/2002	0.84	28.3	0.03
4/25/1997	1.3	35.9	0.036
1/6/1998	1.71	25.8	0.066
1/21/1998	1.22	36.3	0.034
2003-2007	1.17	7.7	0.15

5.3.3 Perturbation Scheme

The timeseries of MFB factors for a three year period, 2005-2007, is taken from the operational system and evaluated to find the type of probability distribution that the MFB follows. To test the impact of bias correction on the prediction of peak discharge, the MFB is treated as a random variable. The radar rainfall input time series is then multiplied by a random variable from the MFB distribution, while preserving spatial and temporal variability of the event.

While several candidate PDFs (e.g. log-normal or exponential) could be fitted, a gamma distribution is selected and its goodness-of-fit evaluated using the Kolmogorov-Smirnov test. The gamma distribution is found to fit the entire dataset closely, as well as, individual events. It is not surprising that the PDF for the period of record is gamma distributed, since each event is so distributed. Each event is perturbed by factors from its own PDF to maintain consistency and realistic storm variability.

The perturbation approach shown in Figure 5.2 seeks to determine the

impact of the variability of rainfall on the generation of runoff. The rainfall, , is modified for input to the model by applying the bias correction factor from each event's distribution function. The infiltration rate, f, is held as a constant which is consistent with the conditions found in the study area. Restating Eq. 5.1 in these terms yields,

$$\int_{\Omega} \frac{\partial \tilde{A}}{\partial t} d\Omega + \int_{\Omega} \frac{\partial \tilde{Q}}{\partial x} d\Omega = \int_{\Omega} \tilde{R}\, d\Omega - \int_{\Omega} f\, d\Omega \tag{5.4}$$

where the dependent streamflow, Q , and cross sectional area, A , become random dependent variables filtered through the basin model. In V*flo*, the solution of Eq. 5.4 over the space-time domain Ω is implemented using non-linear equations (kinematic wave) rather than linear equations such as the unit hydrograph approach. The model has been setup, calibrated for a range of events, and used operationally in forecasting Brays Bayou. Additional validation of the KWE solution is described below where comparisons are made that demonstrate sensitivity with a full dynamic model, HEC-RAS. The distributed model is thus used to test and identify the role that bias correction plays in achieving accurate predictions along with the scaling relationships evaluated at the sample locations within this basin.

The main steps in the procedure are,

1. Fit probability distribution functions to the measured bias correction factors for each event (Figure 5.3).

2. Select bias correction factors at the 10th, 25th, 50th, 75th, 90th percentiles sampled from the probability distribution function.

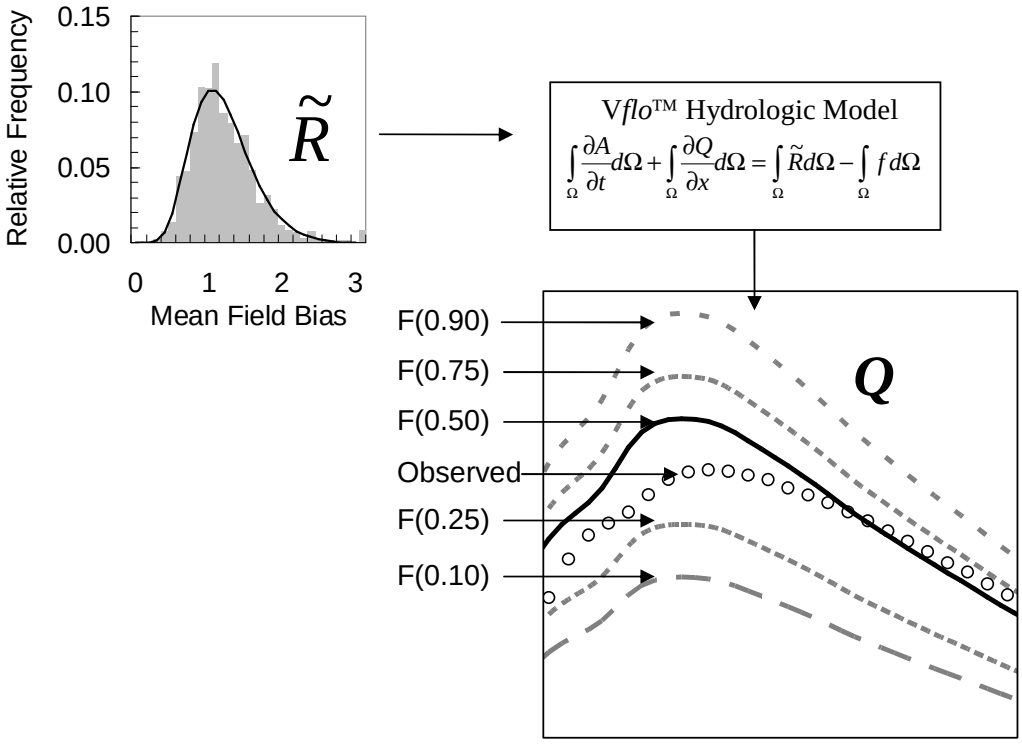

Figure 5.2: Stochastic framework for evaluating gauge corrected rainfall using a distributed hydrologic model

3. Apply uniformly the bias correction factor to rainfall input which is variable in space and time across an event (Figure 5.4).

4. Run the hydrologic model with each bias-corrected rainfall input.

5. Run the hydrologic model with uncorrected rainfall input.

6. Compute the difference between peak discharge generated from bias corrected rainfall input and uncorrected rainfall input.

7. Compute the difference between the 25th and 75th percentiles.

The corresponding difference in discharge at each of the 22 sample locations is then evaluated. The output is characterized by the difference in discharge

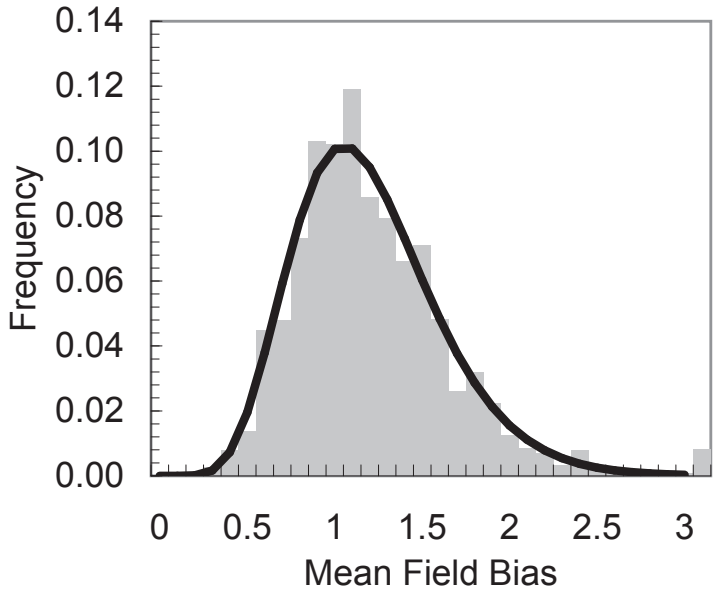

(a)

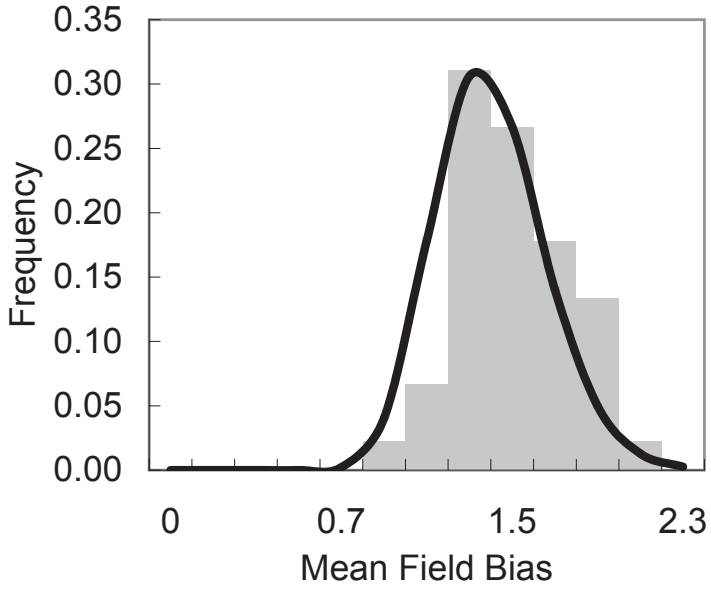

(b)

Figure 5.3: a) Gamma distribution of mean field bias from 2005 -2007 for Brays Bayou. b) gamma distribution for Tropical Storm Frances

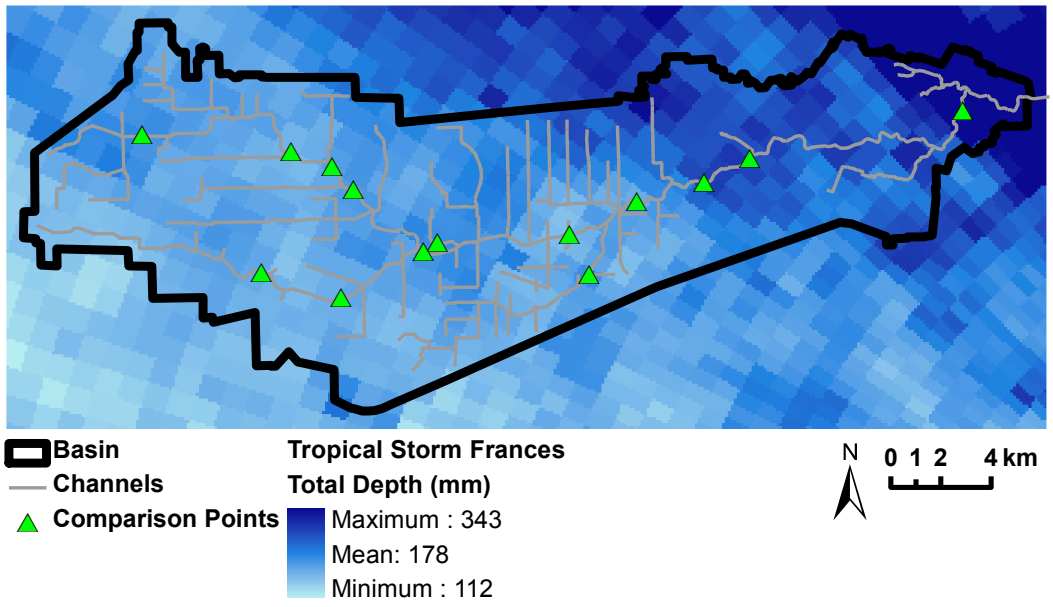

Figure 5.4: Storm total spatial distribution for Tropical Storm Frances

produced by the corrected and uncorrected input obtained by applying the bias correction factors sampled from the input PDF at each percentile. This step is repeated for each of the nine storm events to gain an ensemble of perturbed input and resulting output differences in discharge. Streamflow measurements are not available at the interior sample locations, thus the analysis described next is the difference in corrected and uncorrected discharge as the random variable resulting from the perturbed input filtered through the basin hydrologic model.

Estimating the sensitivity of hydrologic prediction to uncertainty in rainfall input is accomplished by computing peak discharge using corrected radar input (Q_c), and peak discharge using uncorrected radar input (Q_u), which is referred to as dispersion, D, defined as

$$D = Q_c - Q_u \tag{5.5}$$

If the transformation of radar rainfall to runoff were a linear process, then the corresponding difference, D, between the uncalibrated and calibrated radar should increase linearly with the MFB applied.

For verification of the effects found for the KWA model, V*flo*, a comparison is included using the HEC-RAS unsteady dynamic wave model developed for the Harris County Flood Control District as a part of their floodplain mapping. Rainfall input to V*flo* is perturbed by applying bias correction factors at each percentile and then used to simulate the runoff at the upstream Gessner gauge on Brays Bayou. Next, the simulated runoff at the upstream Gessner gauge is routed downstream to the Main Street gauge using both V*flo* and HEC-RAS. Additionally, the observed runoff at the upstream Gessner gauge is routed downstream to the Main Street gauge using both the V*flo* and HEC-RAS models as means of evaluating the model sensitivity for an actual storm event. The simulations are then compared at the limits of the PDFs to see how the solution techniques vary.

5.4 Results and Discussion

5.4.1 Dispersion Scaling with Drainage Area

We wish to find whether dispersion in predicted streamflow scales with drainage area or if it is invariant with scale. From analysis of the long-term MFB factors, the probability density functions follow a gamma distribution as seen in Figure 5.3, both for the period of record (2005-2007), and for a particular event,

e.g. Tropical Storm Frances on September 8-13, 1998. The gamma probability density function parameters for each event are shown in Table 5.1. From each storm event PDF, the perturbed input is used to measure the response across a range of catchment areas using the distributed model.

Another measure of dispersion is the inner-quartile range, which is the difference in flow rates generated from the 75th percentile rainfall, F(0.75) and 25th percentile rainfall, F(0.25). The 75th and 25th quartile rainfall are the corresponding bias correction factors sampled at the quartile and applied to the event. This measure of dispersion is consistent with that proposed by Carpenter and Georgakakos (2004), which is the difference between the flow rate generated from the 90th percentile and the flow rate from the 10th percentile normalized by the 50th percentile flow rate.

Figure 5.5 shows that there is an increase in dispersion as witnessed by the growing difference between peak discharge produced by bias correction quartiles with drainage area. For the first portion of Tropical Storm Allison (TSA1), the difference is increasing monotonically with drainage area with some curvature (Figure 5.5). However, the rate of change is less than expected from a unit-hydrograph assumption of linearity. Thus the effect dampens out with increasing area.

For the second portion of Tropical Storm Allison (TSA2) dispersion also increases between the 70 km^2 and the 220 km^2, but exhibits pronounced erratic behavior for areas less than 70 km^2 (Figure 5.6). Reasons for this decline could be related to the storm event scale in relation to the basin size where random errors in rainfall input did not cancel out. There is a sharp increase in the differences between the gauge corrected and the uncorrected radar rainfall input at the 50 km^2 drainage area sample location. This location corresponds

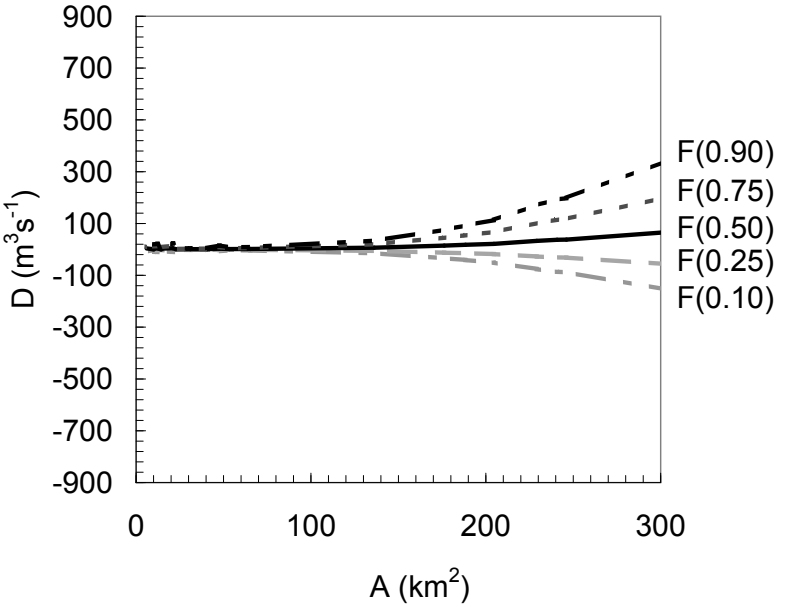

(a)

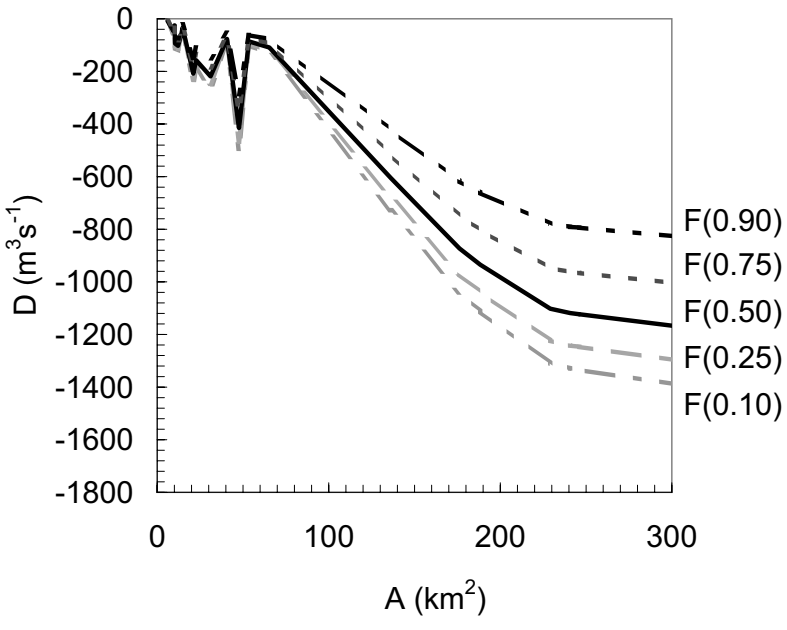

(b)

Figure 5.5: Dispersion scaling for a) Tropical Storm Allison (TSA1), b)Tropical Storm Allison (TSA2), c)Tropical Storm Allison (TSA3) d) August 15, 2002

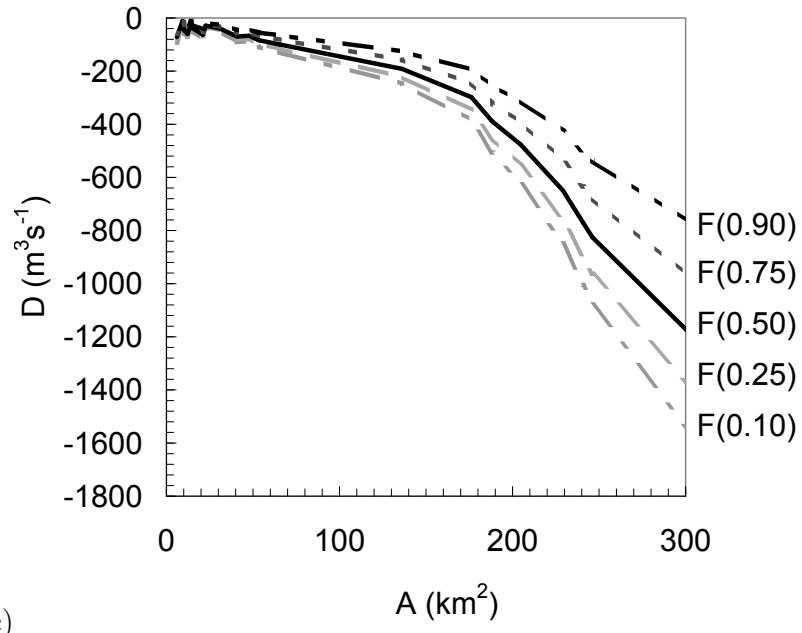

(c)

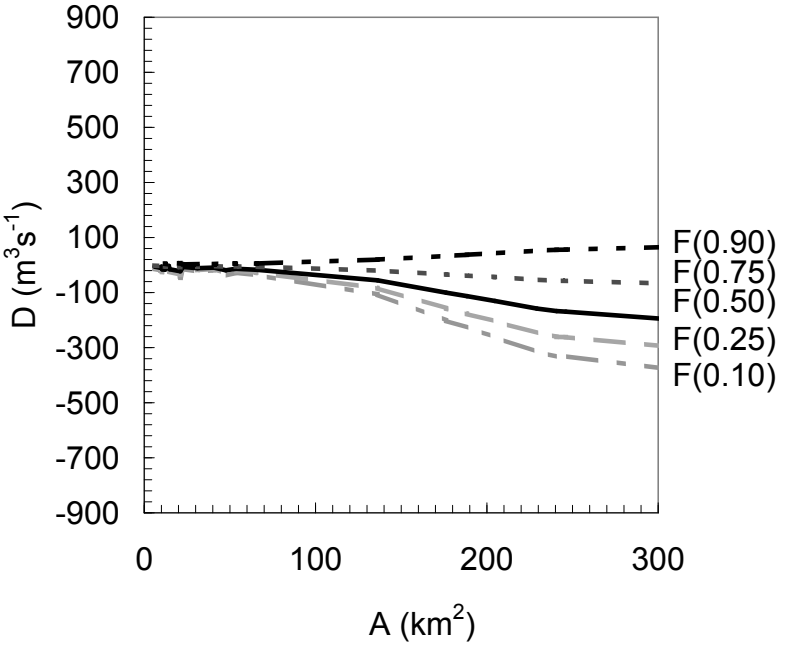

(d)

Figure 5.5: Dispersion scaling for a) Tropical Storm Allison (TSA1), b)Tropical Storm Allison (TSA2), c)Tropical Storm Allison (TSA3) d) August 15, 2002

to the outlet of Keegan's Bayou, a subbasin in the upper reaches of Brays Bayou. From investigation of the individual radar scans, an intense cell was found that developed over this area on June 7, 2001 at 01:15:00 CDT. If the model had used a spatially uniform rainfall input, the effects of this intense storm would have been smoother. At drainage areas larger than about 50 km^2, erratic departures area not present for this event.

For the third part of Allison (TSA3) shown in Figure 5.5c, there is an increase in the dispersion with increasing drainage area as compared with other events. There is a change in the rate of increase of the dispersion, $\Delta D/\Delta A$, at the 170 km^2 drainage area, where rainfall spatial distribution is a possible explanation for this scaling behavior, because there is a strong gradient of rainfall depth from east to west across the basin, with heavier rainfall to the east. In fact, when the rainfall is spatially averaged, i.e. lumped over the basin, the increase becomes uniform in terms of dispersion increase, $\Delta D/\Delta A$.

Dispersion in flow rate is found to scale with drainage area. As the drainage area increases, the calibration of radar rainfall becomes more important for simulating hydrologic processes. For instance, the difference between the flow rates (dispersion) generated from rainfall at the 50^{th} percentile bias is approximately 1200 m^3s^{-1} for 300 km^2. However, the difference for the 100 km^2 drainage basin is only 150 m^3s^{-1} for a drainage area of 100 km^2. Therefore the dispersion increases nonlinearly as the drainage area increases. Consistent results are evident in the remaining events shown in Figure 5.6.

As mentioned above, a comparison is performed between the kinematic wave model, V*flo*, and the dynamic wave model, HEC-RAS. Figure 5.7 shows the degree to which rainfall input uncertainty is propagated through each of the models. The flow is routed using each of the hydraulic models from the

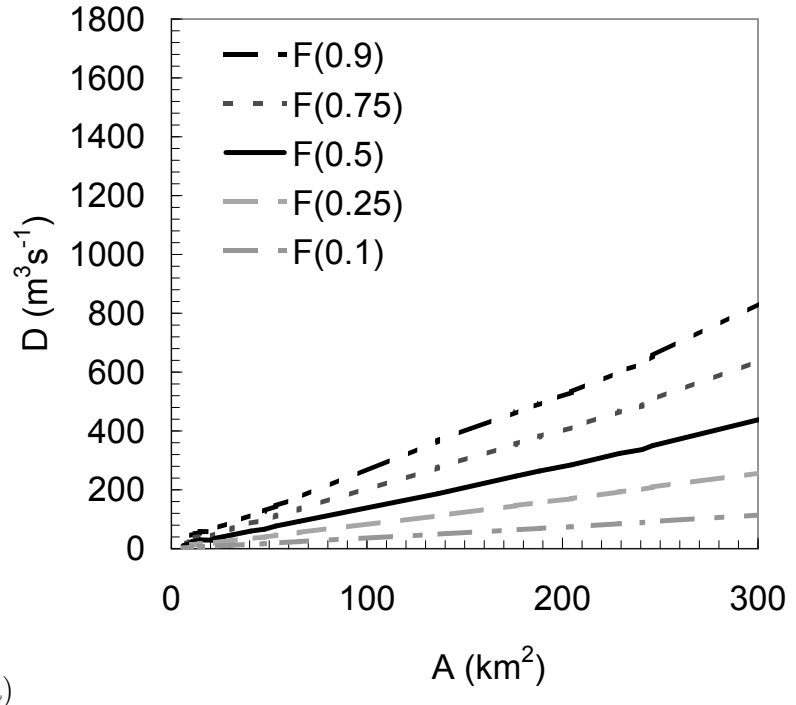

(a)

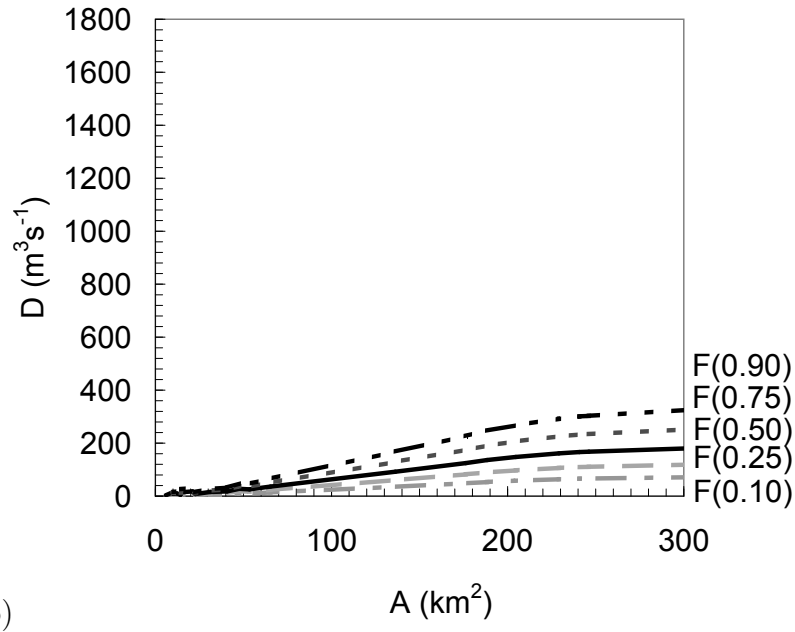

(b)

Figure 5.6: Dispersion scaling for a) Frances, b) January 6, 1998, c) April 25, 1997, d) January 21, 1998

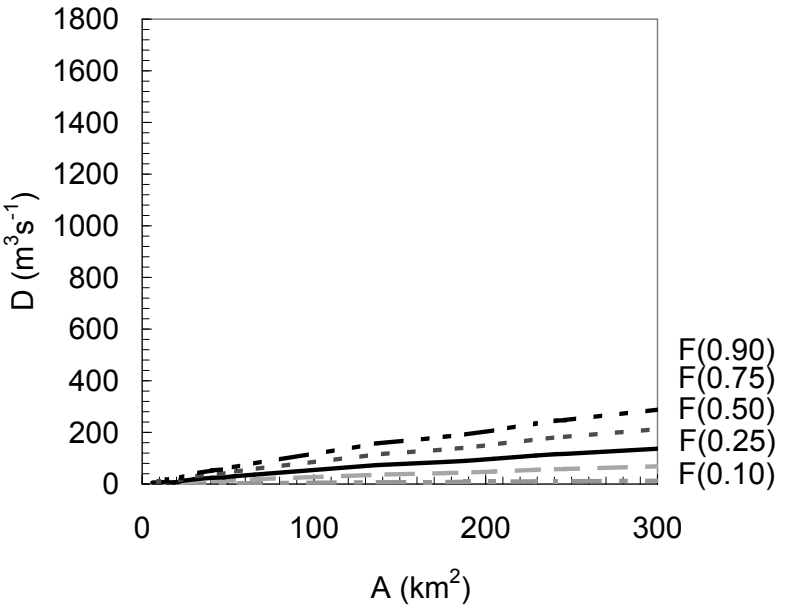

(c)

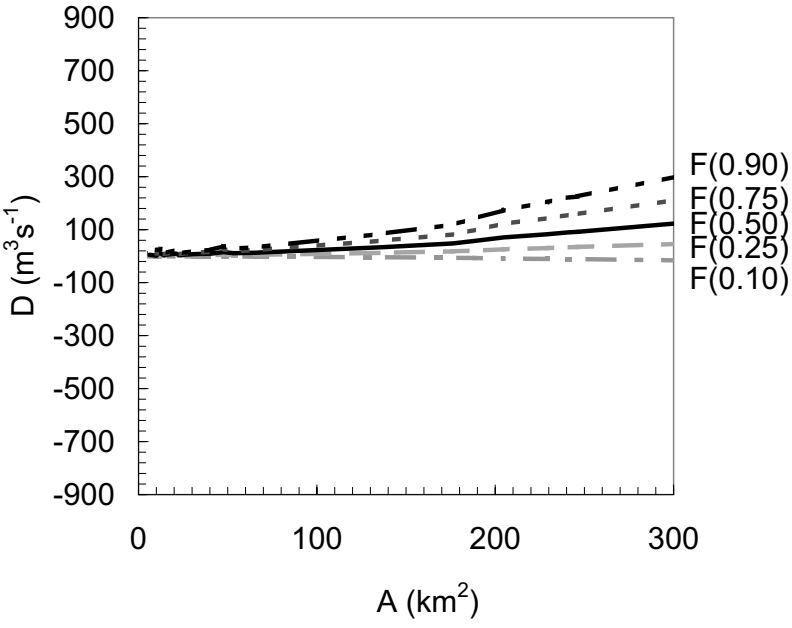

(d)

Figure 5.6: Dispersion scaling for a) Frances, b) January 6, 1998, c) April 25, 1997, d) January 21, 1998

Gessner gauge to the Main Street gauge for the August 15, 2002 event. This event had flows that were contained within the main channel and did not have significant floodplain interactions, which allows for a simpler evaluation of how each model propagates the uncertainty in bias correction factors. Also, the observed flow from the Gessner gauge is routed to Main Street using the HEC-RAS model. Simulations are performed for the F(0.01), F(0.5), and F(0.99) bias correction factors. There is only a 2.8 m^3s^{-1} difference between the two models for the F(0.01) bias correction factor, a 15.1 m^3s^{-1} difference for the F(0.5) bias correction factor, and a 47.4 m^3s^{-1} difference for the F(0.99) bias correction factor. Also, the difference between observed discharge and the V*flo* model is only 0.4 m^3s^{-1} for the F(0.5) bias correction factor, while peak discharge produced by HEC-RAS is more attenuated as expected. However, in terms of sensitivity to bias correction, these results demonstrate similarity between the kinematic wave and the dynamic wave model for this basin.

The graph in Figure 5.8 shows a measure of the dispersion for all events on the same plot for comparative purposes. The inner quartile range represents the difference between the flow generated from the 75th percentile rainfall and the flow generated from the 25th percentile rainfall. An interesting scaling relationship is the apparent linear increase in dispersion for the Frances event. The spatial distribution of the Frances storm event resulted in a relatively uniform pattern over the basin, which could explain the scaling behavior with drainage area. However, in TSA2 and TSA3 there is a non-linear relationship between dispersion and drainage area, with pronounced changes in the rate of dispersion increase with area.

We have demonstrated that the effect of bias correction becomes more important with larger drainage areas as shown by the increase in dispersion with

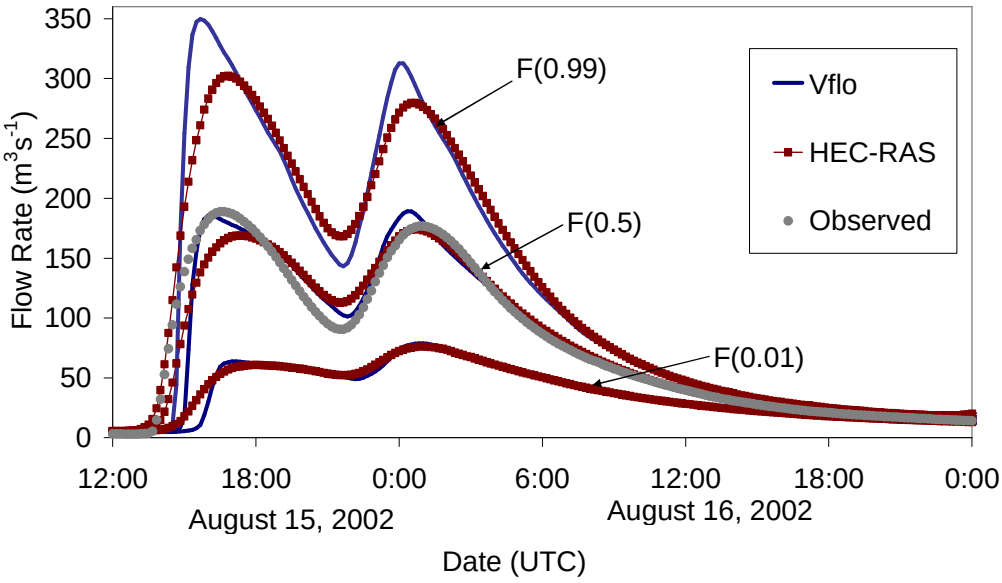

Figure 5.7: Comparison of V*flo* and HEC-RAS for the 2002-08-15 event for the Main Street gauge

increased drainage area. The scaling is not constant but varies by storm showing that rainfall spatio-temporal distribution of each event can play a major or minor role. These results are derived from perturbation of rainfall input based on the PDF of bias correction factors for each event. As distributed hydrologic modeling is used to predict stormwater runoff using spatially variable input, the model performance at interior locations is scale dependent due to the nonlinear behavior of the governing equations, and the spatial distribution of rainfall. The next section addresses the effect of bias correction on prediction skill and its scale behavior obtained through comparison of observed and simulated peak discharge at two locations where streamflow records exist.

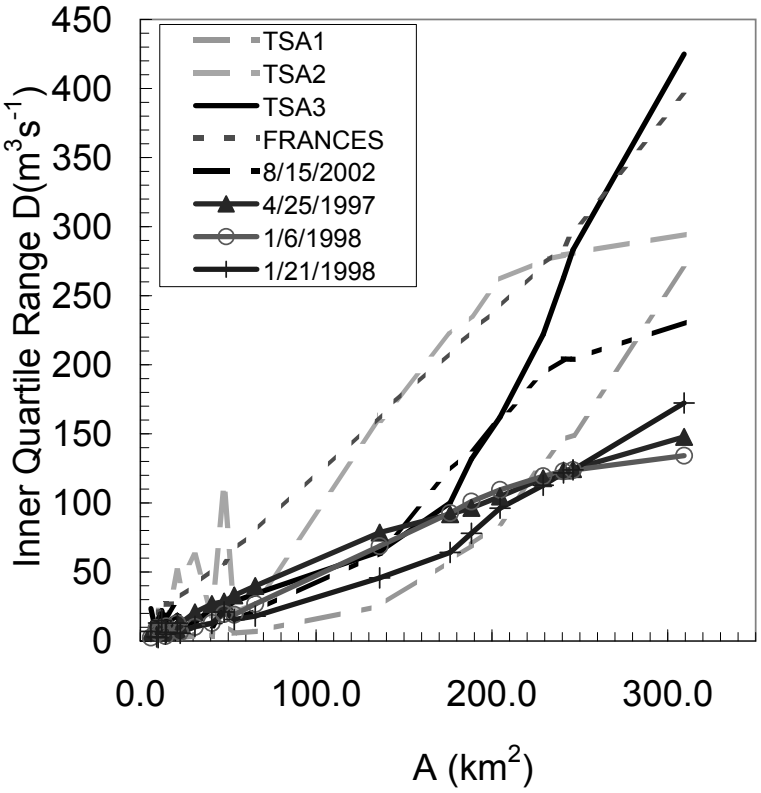

Figure 5.8: Scaling of inner quartile range by drainage area

5.4.2 Predictability and Scaling

In order to assess the impact of increasing drainage area on the predictability, comparison is made between the observed and simulated hydrographs. For this basin there are two streamflow gauges located at Main Street (245.8 km^2) and Gessner (136 km^2). The model predictability is evaluated using a contingency table and skill scores, probability of detection (POD), false alarm ratio (FAR), and critical success index (CSI). Physically, these measures indicate the ability of the model to make accurate predictions at the locations tested. A high CSI indicates that few false alarms (over-predictions) were made in relation to the probability of detection of a flood event.

Table 5.2: Contingency table showing hits, misses, false alarms and correct negative outcomes

		Observed	
		Yes	**No**
Forecast	**Yes**	Hits – a	False alarms - c
	No	Misses - b	Correct Negative - d

A 2 x 2 contingency table consists of hits, misses, and false alarms and is useful for evaluation of meteorological forecast skill (Wilks, 2006). Table 5.2 presents the possible forecast outcomes for an observed event.

The skill scores for the False Alarm Ratio, FAR, Probability of Detection, POD, and Critical Success Index, CSI, are computed from the scalar attributes as,

$$FAR = \frac{b}{a+b} \tag{5.6}$$

$$POD = \frac{a}{a+c} \tag{5.7}$$

$$CSI = \frac{a}{a+b+c} \tag{5.8}$$

where the a, b, and c scalars are defined as in Table 5.2. Unlike applications where there are discrete events, predicted and observed flow rates are continuous variables. Therefore a threshold must be established to assign a hit or

Table 5.3: Contingency table showing hits, misses, false alarms and correct negative outcomes

Sample Point	Area (km^2)	Precipitation Input	CSI	POD	FAR
Brays Bayou at Main Street	259	Uncorrected	0.25	0.33	0.50
		Gauge Corrected	0.75	0.86	0.14
		Precipitation Input	**CSI**	**POD**	**FAR**
Brays Bayou at Gessner	136	Uncorrected	0.43	0.60	0.40
		Gauge Corrected	1.00	1.00	0.00

miss. The threshold used to define a hit, miss or false alarm is tested. Once the threshold is settled on, the scalar attributes for the contingency table can be computed for the events. A limited sensitivity to threshold magnitude is evaluated as seen in Figure 5.9. Regardless of the threshold chosen, the corrected radar product produces a higher CSI, whereas the uncorrected is lowest for all cases. This pattern of forecast accuracy is consistent between the two stream gauges. To summarize, the POD, FAR, and CSI are presented for all events in Table 5.3. The CSI measure indicates the level of hits versus the number of forecasts, which represents the ratio of correct forecasts to total forecasts made.

The CSI improves 3-fold with gauge correction of the radar input showing dramatic improvement in predictability with bias correction (Figure 5.10). The results show interesting scaling behavior where the CSI decreases as the drainage area increases from 136 km^2 (Gessner) to 259 km^2 (Brays) for both corrected and uncorrected inputs.

This scale-dependence in peak behavior runs counter to the expectation of cancellation of random errors over catchment area for volume, and thus the decline in forecast skill measured by the CSI may not be intuitive. It should be noted that the storm duration of the events used in the analysis was between

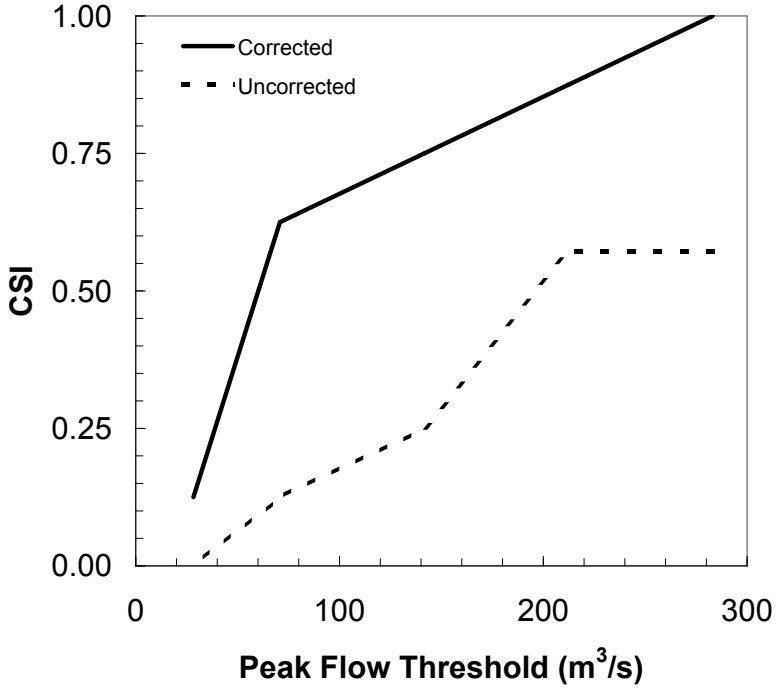

Figure 5.9: Identification of critical success index

6–17 hours. For shorter duration events, then peaks from sub-catchments may not add together. The perturbation experiment confirmed that the dispersion between corrected and uncorrected input scaled with drainage area, and for some events, at a nonlinear rate. As expected the CSI dramatically increased with gauge-corrected radar. However, both dispersion, D, and the CSI predictability measure decrease with increasing drainage area showing that they are not scale invariant.

5.5 Summary

Identification of streamflow prediction accuracy using radar as input to a distributed hydrologic model for a relatively impervious basin is performed using corrected and uncorrected radar input. Streamflow predictions are found to

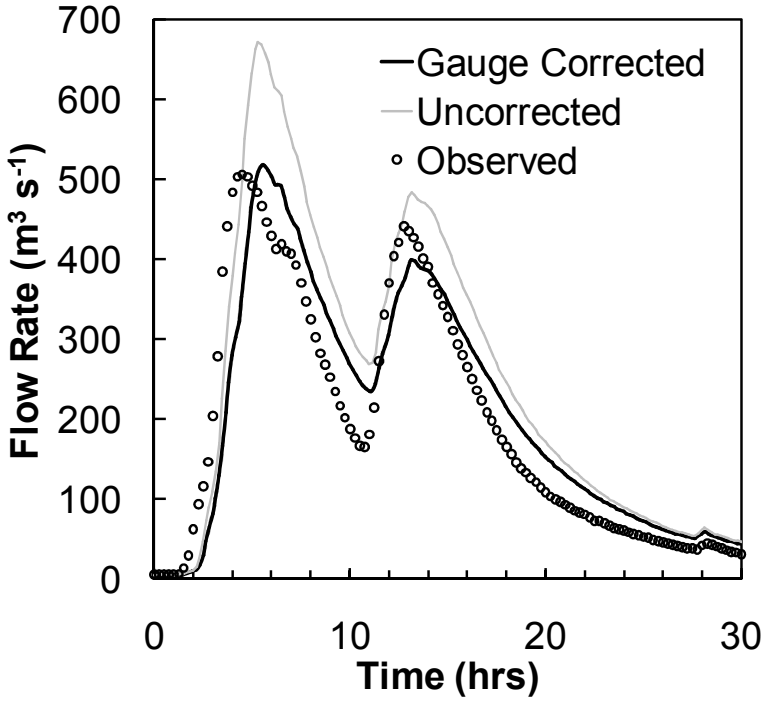

Figure 5.10: Simulated hydrographs for the 2002-08-15 event

depend on: 1) the gauge correction of the radar derived QPE; and 2) the non-linear scaling of gauge-correction with watershed area. Rainfall input is perturbed based on the PDF of bias correction factors for each event showing how gauge correction scales with drainage area. Across storm events, the difference between flow rates produced with corrected and uncorrected radar input consistently increased with drainage area, but at non-constant rates. The comparison between V*flo* and the HEC-RAS model demonstrated similarity between the kinematic wave and the dynamic wave model for this basin. As confirmed by the perturbation experiment, the forecast skill decreases with larger drainage areas. The perturbation of inputs is used to confirm results obtained through comparison of forecast skill at two stream gauge locations. The model skill improves 3-fold when gauge-corrected radar is used over predictions obtained with the use of uncorrected radar. Forecast skill is shown to

be dependent on watershed scale, and the uncertainties do not average out for larger areas. Thus larger basins are more difficult to forecast in terms of peak stage which is critical for flood forecasting.

Chapter 6

Distributed Hydrologic Model Calibration using the Forward Sensitivity Method

6.1 Introduction

This chapter focuses on the level of complexity necessary to model the major hydrologic processes of an urban watershed using a physics based approach. Models of physical processes always require some level of abstraction from the actual physical process to a simpler structure that can be harnessed to answer the question at hand (Rosenblueth and Wiener, 1945). The inherent question is how simple can we make the process. Physics based distributed hydrologic models attempt to explain hydrologic processes using simplifications of physical processes. We usually have data about topography, land use, and soils that can be used to estimate distributed a-priori parameters for a model. However, these a-priori parameter estimates have uncertainty in them due to our lack of knowledge about sub-scale processes that are occurring within the watershed. For operational flash flood forecasting, we are forced to estimate effective parameters that when used with a model satisfactorily reproduce the behavior of a watershed. This is due to both discretization and sub-scale processes that are occurring with a grid point. Determining these effective parameters requires starting with the a-priori parameters as an initial starting point and incrementally adjusting the parameters to minimize an objective function that measures

the difference between simulated state variables and observations. The main question to be addressed in this chapter is in how to perform the adjustment of a-priori parameters. Should the adjustment be performed using a spatially uniform adjustment factor, or does the use of spatially distributed adjustment factors further minimize the differences between simulated state variables and observations? However a better question would be can a well characterized distributed hydrologic model for an urban watershed be improved by a spatially distributed calibration technique. The experiments will be performed using the flood forecasting system described in chapter 5.

The Forward Sensitivity Method (Lakshmivarahan and Lewis, 2010) is a new approach to data assimilation based on sensitivity analysis techniques. Lakshmivarahan and Lewis (2010) has shown that the FSM is equivalent to the 4DVAR technique (Le Dimet and Talagrand, 1986). The adjoint technique has been used by Castaings et al. (2009); Vieux et al. (1998); White et al. (2003) to estimate parameters of a distributed hydrologic model. The advantages of the FSM method as compared with the adjoint are the calculation of sensitivities with the forward model. This allows us to understand how a parameter impacts the simulation results while we are calculating the forward model. It also allows us to see the influence of individual observations on the calibration process. Castaings et al. (2009) showed the power of using a variational approach to model calibration for a simple overland and channel separation. However, he did not investigate the use of higher numbers of parameter groupings. Higher numbers of parameter groupings will be explored in this chapter.

6.2 Methodology

6.2.1 Model Description

The forward model investigated within this chapter is the kinematic wave equation.

6.2.1.1 Formulation

The kinematic wave equation is derived from the continuity equation (6.1)

$$\frac{\partial A}{\partial t} + \frac{\partial Q}{\partial x} = q \tag{6.1}$$

where A is the cross sectional area of flow, Q is the discharge, q is the lateral inflow per unit of length perpendicular to the direction of flow. The lateral inflow per unit of length can be further subdivided into,

$$q = (r - i)w \tag{6.2}$$

where r is the rainfall rate, i is the infiltration rate, and w is the width of a grid. Infiltration is handled using the Green and Ampt Model described in Chapter 2.

The underlying assumption of the kinematic wave equation is that there is a functional relationship between Q and A. This occurs under uniform flow conditions. Assuming this form results in a greatly simplified representation of the full dynamic wave equations.

Further, Henderson (1966) showed the relationship between the wave propagation speed, $\frac{dx}{dt}$, and the kinematic wave celerity, c. If $Q = f(A)$ is continu-

ously differentiable there exists a relationship $\frac{dQ}{dA}$ referred to as the kinematic wave celerity. Substituting the kinematic wave celerity into (6.1) gives,

$$\frac{\partial A}{\partial t} + \frac{dQ}{dA}\frac{\partial A}{\partial x} = q \tag{6.3}$$

Using the simplified momentum equation (i.e. assuming uniform flow) results in a form of the momentum equation where gravity force is balanced by the shear force (Sturm, 2001),

$$\gamma A \Delta L sin\,(\theta) = \tau_0 P \Delta L \tag{6.4}$$

where γ is the specific weight of the fluid, A is the cross sectional area of flow, ΔL is the length between grid points, τ_0 is the shear stress along the bottom of the channel, and P is the wetted perimeter in contact with the fluid. $sin\,(\theta)$ can be further approximated as the bed slope, S_0 (i.e. $tan\,(\theta)$) bed slope) for very small values of θ. For steady uniform flow the bed slope is equal to the slope of the energy grade line, S_f where

$$S_f = \frac{h_f}{L} \tag{6.5}$$

Therefore, (6.4) can be further rearranged as

$$\frac{h_f}{L} = \frac{\tau_0 P}{\gamma A} \tag{6.6}$$

The uniform flow velocity, V, can then be approximated using Manning's formula

$$V = \frac{C}{\eta}\left(\frac{A}{P}\right)^{2/3} {S_f}^{1/2} \tag{6.7}$$

Combining the main geometric terms for wetted perimeter and friction slope,

$$G = \frac{C}{P^{2/3}} {S_f}^{1/2} \tag{6.8}$$

Therefore, the discharge, Q, is represented as,

$$Q = VA = \frac{G}{\eta} A^m \tag{6.9}$$

where $m = \frac{5}{3}$ for Manning's equation.

Eq. 6.9 can be differentiated with respect to A either analytically for regular geometries or numerically for irregular cross sections to yield the kinematic wave celerity $\frac{\partial Q}{\partial A}$.

6.2.1.2 Discretization

Discretization of the kinematic wave equation can be handled using either method of characteristics (Woolhiser and Liggett, 1967), finite difference, finite element techniques (Desai, 1979; Jayawardena and White, 1977; Vieux, 1988). A complete summary of the various techniques for kinematic wave modeling is provided by Singh (1996). Vieux (1988) found that the finite element technique could be useful for simulating overland runoff. He used nodal values of roughness and slope to overcome instability problems within the finite element discretization. A thorough comparison of finite difference techniques was performed by Castantindies (1981). He compared a backward, weighted average backward, backward central, backward central leap frog, diffusive, unstable, and leap frog finite difference schemes. The results showed that a forward time backward difference provided the most accurate and stable

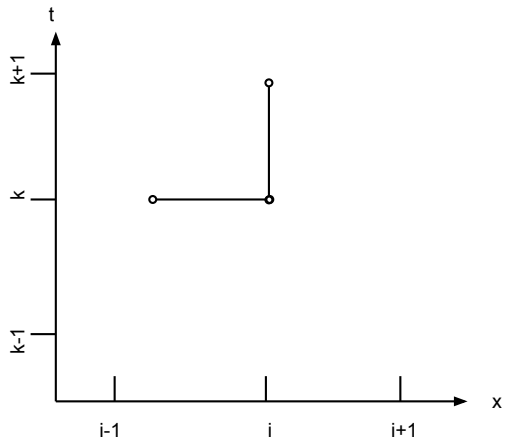

Figure 6.1: Finite difference stencil for forward time backward difference

results. Stephenson and Meadows (1986) further indicated that this forward time backward finite difference technique most closely resembles the method of characteristics. They indicated that both the method of characteristics and the forward time backward difference only propagate information downstream which is a constraint of the kinematic wave equation. Therefore, the kinematic wave equation is discretized for this chapter using the forward time backward difference finite difference form.

$$\frac{A_{i,k+1} - A_{i,k}}{\Delta t} + \frac{Q_{i,k} - Q_{i-1,k}}{\Delta x} = r_{i,k+1} w_i \tag{6.10}$$

Rearranging and solving for $A_{i,k}$ and substituting

$$A_{i,k+1} = A_{i,k} - \frac{\Delta t}{\Delta x}\left(\frac{G_i}{\eta_i} A_{i,k}^m - \frac{G_{i-1}}{\eta_{i-1}} A_{i-1,k}^m\right) + r_{i,k+1} w_i \Delta t \tag{6.11}$$

$$\begin{bmatrix} A_1 \\ \vdots \\ A_i \\ \vdots \\ A_n \end{bmatrix}_{k+1} = \begin{bmatrix} A_1 \\ \vdots \\ A_i \\ \vdots \\ A_n \end{bmatrix}_{k} - \frac{\Delta t}{\Delta x} \begin{bmatrix} \frac{G_1}{\eta_1} A_1^m - \frac{G_0}{\eta_0} A_0^m \\ \vdots \\ \frac{G_i}{\eta_i} A_i^m - \frac{G_{i-1}}{\eta_{i-1}} A_{i-1}^m \\ \vdots \\ \frac{G_n}{\eta_n} A_n^m - \frac{G_{n-1}}{\eta_{n-1}} A_{n-1}^m \end{bmatrix}_{k} + \Delta t \begin{bmatrix} w_1 r_1 \\ \vdots \\ w_i r_i \\ \vdots \\ w_n r_n \end{bmatrix}_{k+1} \tag{6.12}$$

And in matrix form,

$$\begin{bmatrix} A_1 \\ \vdots \\ A_i \\ \vdots \\ A_n \end{bmatrix}_{k+1} = \begin{bmatrix} A_1 \\ \vdots \\ A_i \\ \vdots \\ A_n \end{bmatrix}_{k} - \frac{\Delta t}{\Delta x} \begin{bmatrix} 1 & 0 & \cdots & 0 & 0 \\ -1 & 1 & 0 & \vdots & \vdots \\ 0 & -1 & \ddots & 0 & 0 \\ \vdots & \ddots & \ddots & 1 & 0 \\ 0 & \dots & 0 & -1 & 1 \end{bmatrix} \begin{bmatrix} \frac{G_1}{\eta_1} A_1 m \\ \vdots \\ \frac{G_i}{\eta_i} A_i m \\ \vdots \\ \frac{G_n}{\eta_n} A_n m \end{bmatrix}_{k} + \Delta t \begin{bmatrix} w_1 r_1 \\ \vdots \\ w_i r_i \\ \vdots \\ w_n r_n \end{bmatrix}_{k+1} \tag{6.13}$$

The system of equations can be modified for a branched network by modifying the spatial partial derivative of (6.1) by using the following,

$$\frac{\partial Q}{\partial x} = \frac{\sum Q_o - \sum Q_i}{\bar{\Delta} x} \tag{6.14}$$

where $\sum Q_o$ represents the sum of the inflows to a cell and $\sum Q_i$ represents the sum of the outflows from a cell. The $\bar{\Delta} x$ term represents the average length of each grid point above a branch location.

6.2.2 Forward Sensitivity Method

The Forward Sensitivity Method (Lakshmivarahan and Lewis, 2010) was developed to show the equivalence between forward sensitivity analysis techniques and the 4DVAR method. The optimization component of FSM can be used for parameter estimation. The following section describes the calculation of the forward sensitivities necessary for the parameter adjustment step. The following derivation shows the sensitivities with respect to Manning's roughness.

$$A_{i,k+1} = A_{i,k} - \frac{\Delta t}{\Delta x}\left(\frac{G_i}{\eta_i} A_{i,k}^m - \frac{G_{i-1}}{\eta_{i-1}} A_{i-1,k}^m\right) + \gamma r_{i,k+1} w_i \Delta t \tag{6.15}$$

6.2.2.1 First Order Sensitivities with Respect to Roughness

$$A_{i,k+1} = A_{i,k} - \frac{\Delta t}{\Delta x}\left(\frac{G_i}{\eta_i} A_{i,k}^m - \frac{G_{i-1}}{\eta_{i-1}} A_{i-1,k}^m\right) + r_{i,k+1} w_i \Delta t \tag{6.16}$$

$$M(A_{i,k}) \equiv A_{i,k} - \frac{\Delta t}{\Delta x}\left(\frac{G_i}{\eta_i} A_{i,k}^m - \frac{G_{i-1}}{\eta_{i-1}} A_{i-1,k}^m\right) + r_{i,k+1} w_i \Delta t \tag{6.17}$$

$$\frac{\partial A_{i,k+1}}{\partial \eta_j} = \sum_{q=1}^{n} \left[\frac{\partial M_{i,k}}{\partial A_{q,k}} \frac{\partial A_{q,k}}{\partial \eta_j} \right] + \left[\frac{\partial M_{i,k}}{\partial \eta_j} \right] \tag{6.18}$$

For $1 \leq i \leq n$ and $1 \leq j \leq p$ with $\frac{\partial A_i(0)}{\partial \eta_j} = 0$ as initial condition.

For $i = j$

$$\begin{aligned} \frac{\partial A_{i,k+1}}{\partial \eta_j} = \frac{\partial A_{i,k}}{\partial \eta_j} - \frac{\Delta t}{\Delta x} \Big(& \frac{G_i}{\eta_i} m A_{i,k}^{m-1} \frac{\partial A_{i,k}}{\partial \eta_j} - \frac{G_i}{\eta_i^2} A_{i,k}^{m} \\ & - \frac{G_{i-1}}{\eta_{i-1}} m A_{i-1,k}^{m-1} \frac{\partial A_{i-1,k}}{\partial \eta_j} \Big) \end{aligned} \tag{6.19}$$

For $i > j$

$$\frac{\partial A_{i,k+1}}{\partial \eta_j} = \frac{\partial A_{i,k}}{\partial \eta_j} - \frac{\Delta t}{\Delta x} \left(\frac{G_i}{\eta_i} m A_{i,k}^{m-1} \frac{\partial A_{i,k}}{\partial \eta_j} - \frac{G_{i-1}}{\eta_{i-1}} m A_{i-1,k}^{m-1} \frac{\partial A_{i-1,k}}{\partial \eta_j} \right) \tag{6.20}$$

For $i - 1 = j$

$$\begin{aligned} \frac{\partial A_{i,k+1}}{\partial \eta_j} = \frac{\partial A_{i,k}}{\partial \eta_j} - \frac{\Delta t}{\Delta x} \Big(& \frac{G_i}{\eta_i} m A_{i,k}^{m-1} \frac{\partial A_{i,k}}{\partial \eta_j} - \frac{G_{i-1}}{\eta_{i-1}} m A_{i-1,k}^{m-1} \frac{\partial A_{i-1,k}}{\partial \eta_j} \\ & + \frac{G_{i-1}}{\eta_{i-1}^2} A_{i-1,k}^{m} \Big) \end{aligned} \tag{6.21}$$

For $i - 1 < j$

$$\frac{\partial A_{i,k+1}}{\partial \eta_j} = 0 \tag{6.22}$$

because $A_{i,k+1}$ is independent of η_j

The equations follow a general form of,

$$\begin{aligned} \frac{\partial A_{i,k+1}}{\partial \eta_j} = \frac{\partial A_{i,k}}{\partial \eta_j} - \frac{\Delta t}{\Delta x} \Big(& \frac{G_i}{\eta_i} m A_{i,k}^{m-1} \frac{\partial A_{i,k}}{\partial \eta_j} - \delta_{i,j} \frac{G_i}{\eta_i^2} A_{i,k}^{m} \\ & - \frac{G_{i-1}}{\eta_{i-1}} m A_{i-1,k}^{m-1} \frac{\partial A_{i-1,k}}{\partial \eta_j} + \delta_{i-1,j} \frac{G_{i-1}}{\eta_{i-1}^2} A_{i-1,k}^{m} \Big) \end{aligned} \tag{6.23}$$

where δ is the standard Kronecker delta function. It is helpful to notice that the term $\frac{G}{\eta}mA^{m-1}$ is the kinematic wave celerity $\frac{\partial Q}{\partial A}$. Therefore, a generalized notation for any cross sectional geometry would be,

$$\begin{aligned}\frac{\partial A_{i,k+1}}{\partial \eta_j} = \frac{\partial A_{i,k}}{\partial \eta_j} - \frac{\Delta t}{\Delta x}\Big(&\frac{\partial Q}{\partial A}_i \frac{\partial A_{i,k}}{\partial \eta_j} - \delta_{i,j}\frac{G_i}{\eta_i^2}A_{i,k}^m \\ &-\frac{\partial Q}{\partial A}_{i-1}\frac{\partial A_{i-1,k}}{\partial \eta_j} + \delta_{i-1,j}\frac{G_{i-1}}{\eta_{i-1}^2}A_{i-1,k}^m\Big)\end{aligned} \tag{6.24}$$

The sensitivity equations can also be expressed in matrix form as,

$$D_\eta(A_{k+1}) = D_A(M_k)D_\eta(A_k) + D_\eta(M_k) \tag{6.25}$$

where $D_A(M) = \frac{\partial M_i}{\partial A_q}$, $D_\eta(A) = \frac{\partial A_q}{\partial \eta_j}$ and $D_\eta(M) = \frac{\partial M_i}{\partial \eta_j}$

This can further be simplified for a branched network using the incidence matrix, C,

$$D_\eta(A_{k+1}) = D_A(M_k)D_\eta(A_k) + D_\eta(M_k) \tag{6.26}$$

where $D_A(M_k) = I - \frac{\Delta t}{\Delta x}[C]\left[\frac{\partial Q}{\partial A}\right]_k$ and $D_\eta(M_k) = \frac{\Delta t}{\Delta x}[C]\left\{\frac{Q}{\eta}\right\}_k$

Alternatively, if the adjustment is performed as a multiplier (β) it can be shown that the sensitivity with respect to the multiplier,

$$\begin{aligned}\frac{\partial A_{i,k+1}}{\partial \beta_j} = \frac{\partial A_{i,k}}{\partial \beta_j} - \frac{\Delta t}{\Delta x}\Big(&\frac{G_i}{\eta_i}mA_{i,k}^{m-1}\frac{\partial A_{i,k}}{\partial \beta_j} - \delta_{i,j}\frac{G_i}{\eta_i\beta_i}A_{i,k}^m \\ &-\frac{G_{i-1}}{\eta_{i-1}}mA_{i-1,k}^{m-1}\frac{\partial A_{i-1,k}}{\partial \beta_j} + \delta_{i-1,j}\frac{G_{i-1}}{\eta_{i-1}\beta_{i-1}}A_{i-1,k}^m\Big)\end{aligned} \tag{6.27}$$

6.2.2.2 First Order Sensitivities with Respect to Rainfall (γ)

$$A_{i,k+1} = A_{i,k} - \frac{\Delta t}{\Delta x}\left(\frac{G_i}{\eta_i}A_{i,k}^m - \frac{G_{i-1}}{\eta_{i-1}}A_{i-1,k}^m\right) + \gamma r_{i,k+1} w_i \Delta t \tag{6.28}$$

$$\frac{\partial A_{i,k+1}}{\partial \gamma_j} = \sum_{q=1}^{n}\left[\frac{\partial M_{i,k}}{\partial A_{q,k}}\frac{\partial A_{q,k}}{\partial \gamma_j}\right] + \left[\frac{\partial M_{i,k}}{\partial \gamma_j}\right] \tag{6.29}$$

For $1 \leq i \leq n$ and $1 \leq j \leq p$ with $\frac{\partial A_i(0)}{\partial \gamma_j} = 0$ as initial condition.

or in matrix form,

$$D_\gamma(A_{k+1}) = D_A(M_k)D_\gamma(A_k) + D_\gamma(M_k) \tag{6.30}$$

For $i = j$

$$\frac{\partial A_{i,k+1}}{\partial \gamma_j} = \frac{\partial A_{i,k}}{\partial \gamma_j} - \frac{\Delta t}{\Delta x}\left(\frac{G_i}{\eta_i} m A_{i,k}^{m-1}\frac{\partial A_{i,k}}{\partial \gamma_j}\right) + r_i w_i \Delta t \tag{6.31}$$

For $i > j$

$$\frac{\partial A_{i,k+1}}{\partial \gamma_j} = \frac{\partial A_{i,k}}{\partial \gamma_j} - \frac{\Delta t}{\Delta x}\left(\frac{G_i}{\eta_i} m A_{i,k}^{m-1}\frac{\partial A_{i,k}}{\partial \gamma_j} - \frac{G_{i-1}}{\eta_{i-1}} m A_{i-1,k}^{m-1}\frac{\partial A_{i-1,k}}{\partial \gamma_j}\right) \tag{6.32}$$

For $i < j$

$$\frac{\partial A_{i,k+1}}{\partial \gamma_j} = 0 \tag{6.33}$$

because $A_{i,k+1}$ is independent of γ_j

6.2.2.3 Example Propagation of Sensitivities

Figure 6.2 shows the evolution of the forward sensitivities for the Frances event over the Brays Bayou basin (with a black outline). There are a total of 16722 grid points upstream of this streamflow gauge. The sensitivities are initially negative indicating that the cross sectional area is decreasing during this period. The propagation of sensitivity is also driven by the wave celerity in Eq. 6.26. During the first image, at t=10.5 hrs no rainfall has occurred over the watershed. As the rainfall moves over the watershed the sensitivities fill in upstream of the observation point at Main St. Thus at every point upstream of the observation point the sensitivities indicate whether δA is increasing or decreasing with respect to a change in roughness, $\delta\eta$. It can also be noted that the positive sensitivities near the streamflow gauge. These positive sensitivities indicate that the cells near the observation point will have a stronger influence on parameter estimation.

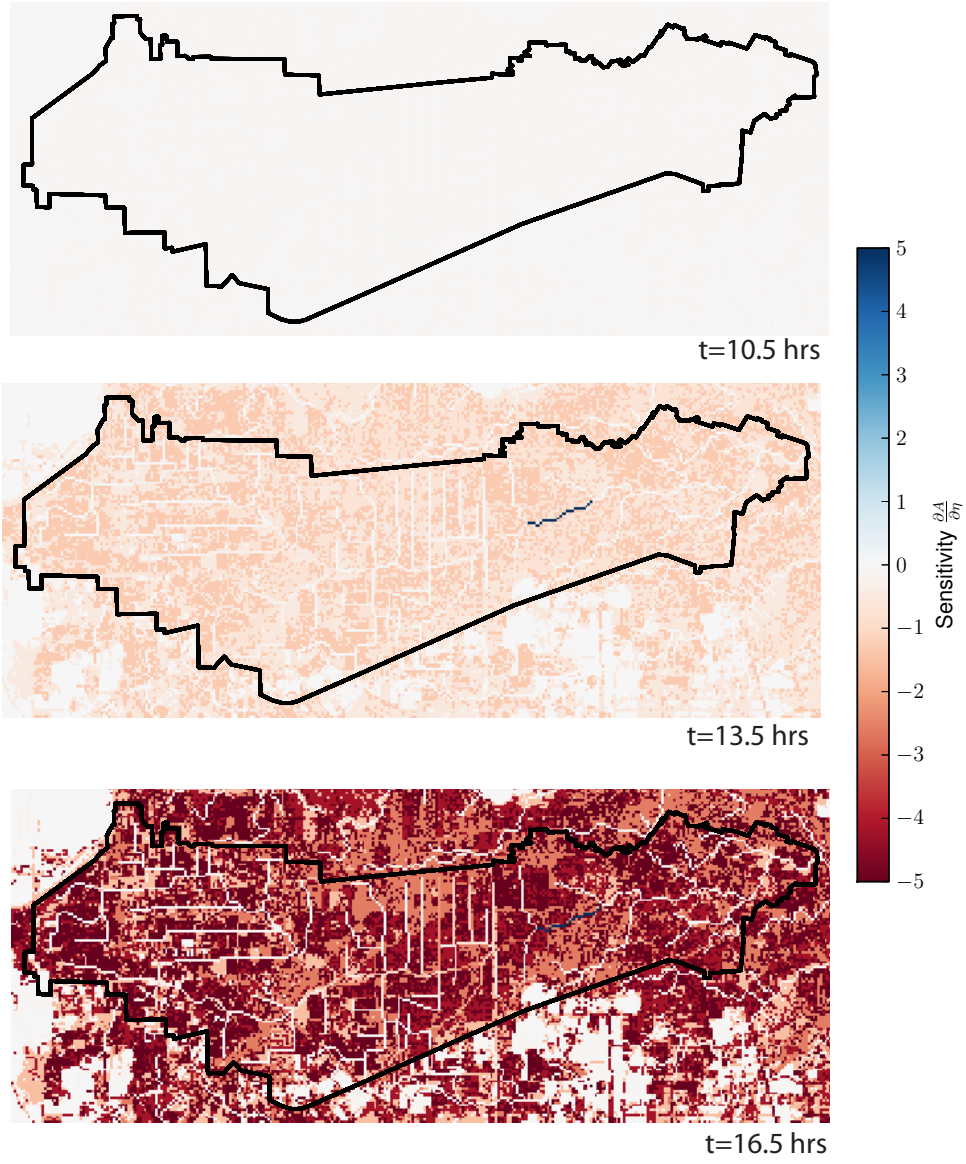

(a)

Figure 6.2: Evolution of Sensitivities for the Main Street gauge during the Frances event

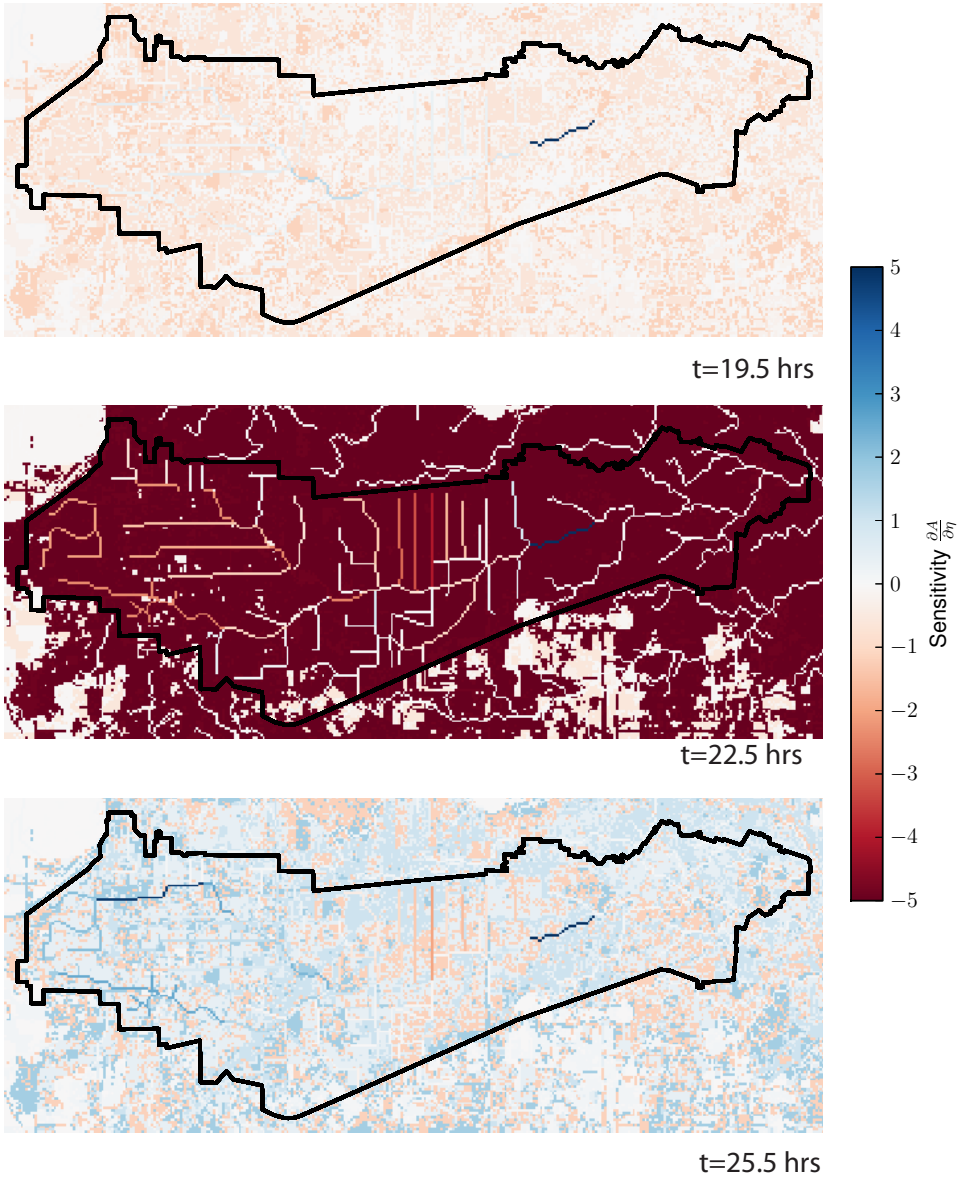

(b)

Figure 6.2: Evolution of Sensitivities for the Main Street gauge during the Frances event

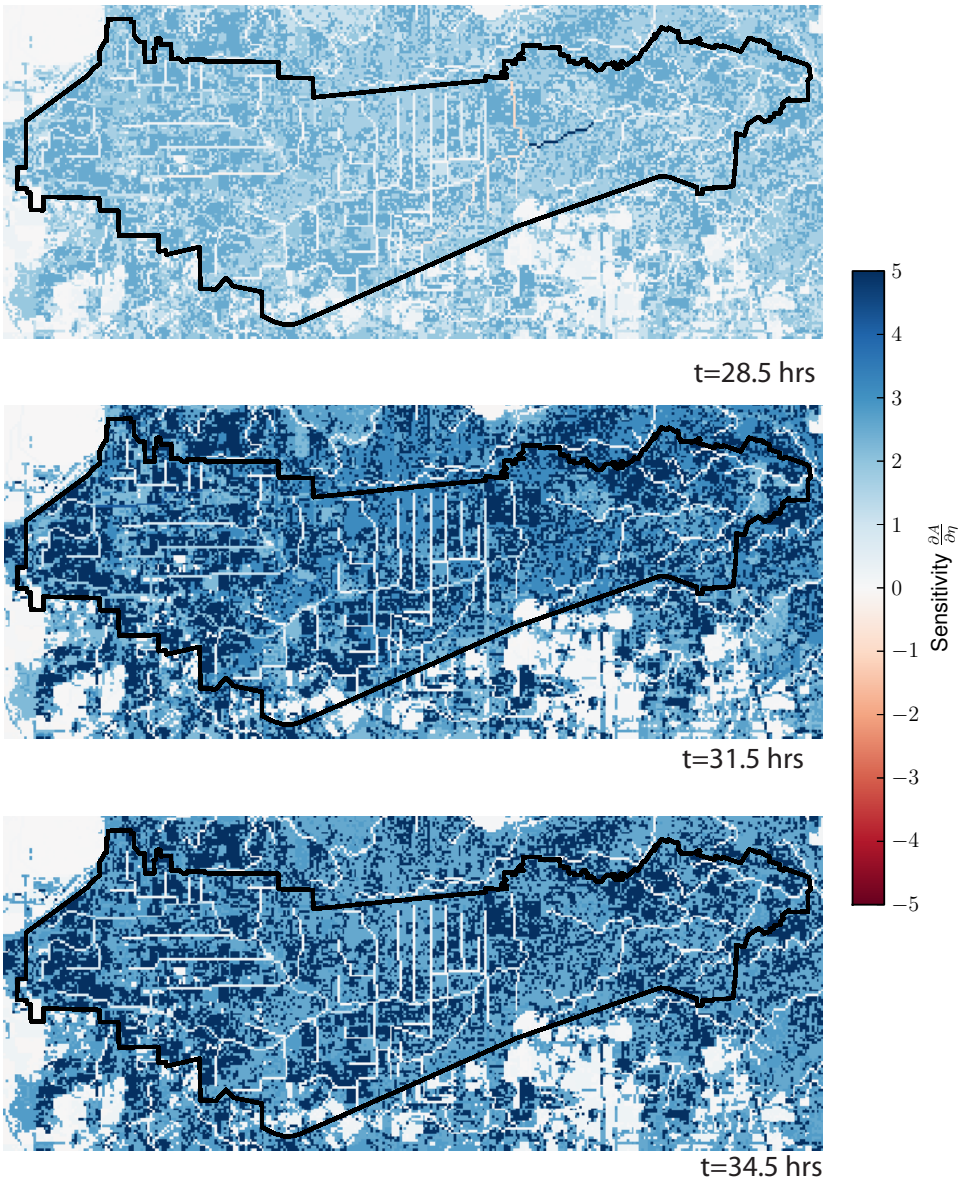

(c)

Figure 6.2: Evolution of Sensitivities for the Main Street gauge during the Frances event

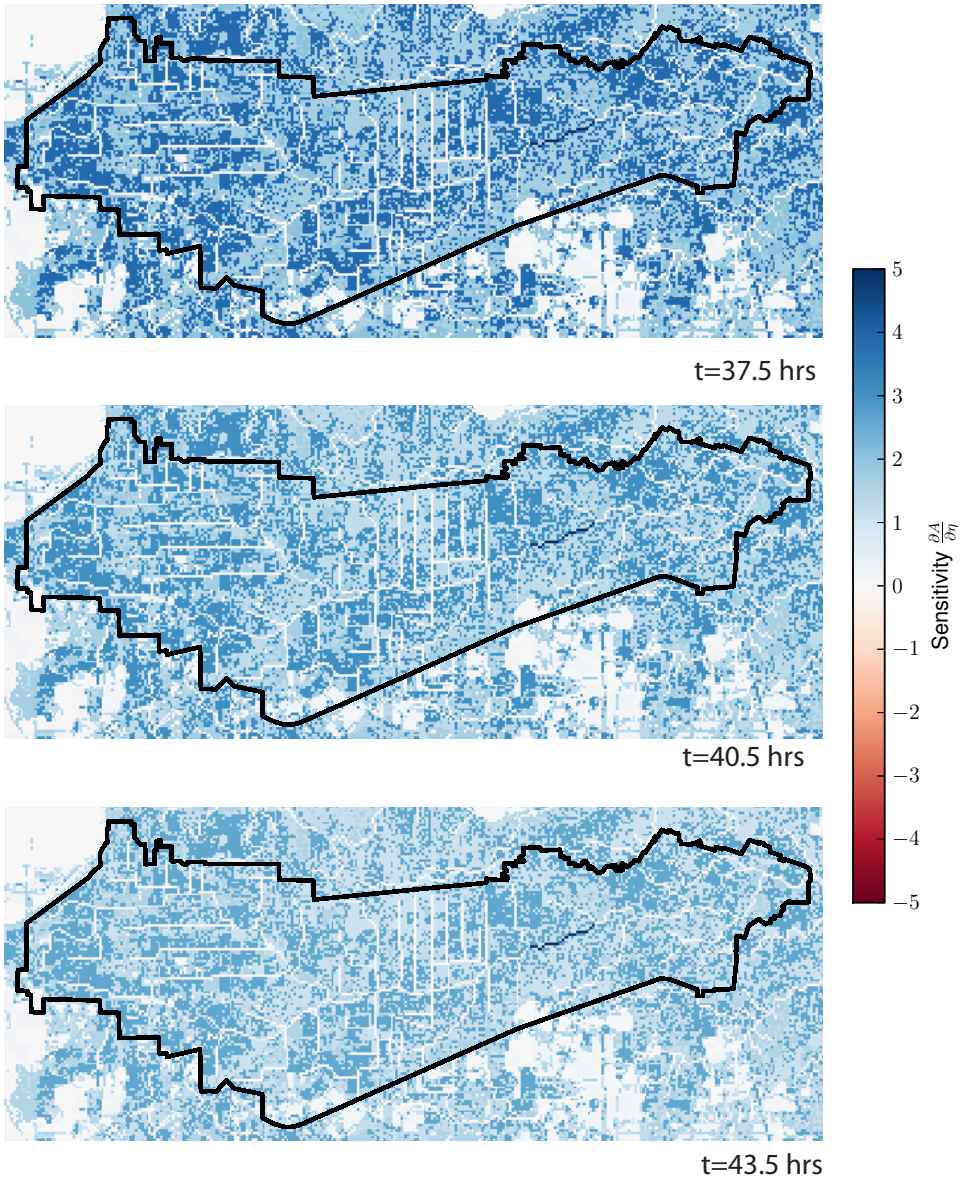

(d)

Figure 6.2: Evolution of Sensitivities for the Main Street gauge during the Frances event

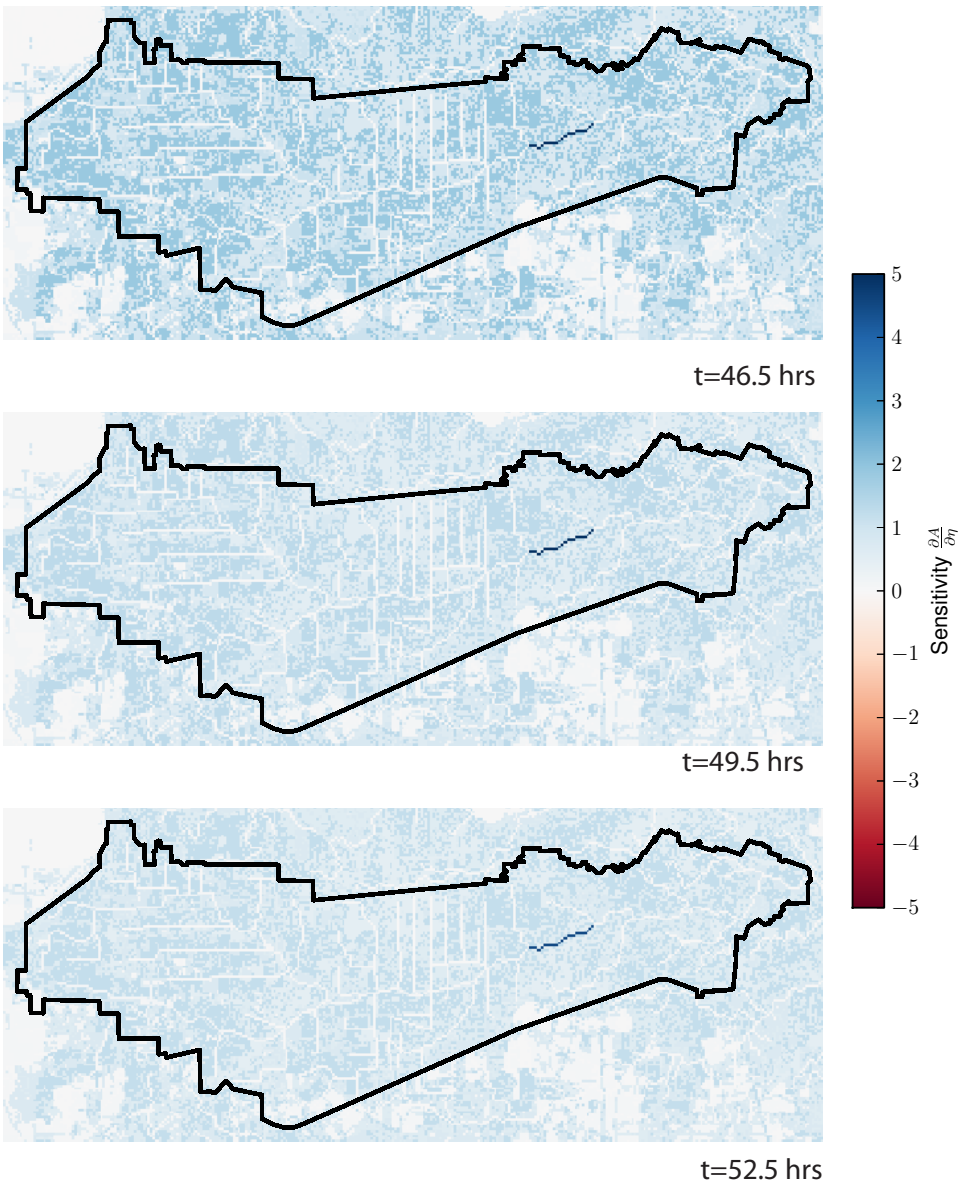

(e)

Figure 6.2: Evolution of Sensitivities for the Main Street gauge during the Frances event

6.2.3 Parameter Adjustment Step

The following derivation follows from Lakshmirvarahan and Lewis (2010). Using the sensitivities derived from the Forward Sensitivity Method, the next step is to adjust model parameters based on a least squares adjustment. If we only allow variations in the parameters while assuming that there are not perturbations to the initial conditions or boundary conditions, then we can approximate the change in the state variable, ΔA, as

$$\Delta A = \delta A = D_\eta (A)\, \delta\eta \tag{6.34}$$

It should be noted that δA can also include perturbations in initial conditions and boundary conditions. However, this case strictly focuses on the distributed parameter estimation problem.

The term on the right hand side $D_\eta (A)\, \delta\eta$ represents the change in the state variable, A, found by multiplying the sensitivity matrix with respect to roughness, $D_\eta (A)$, by the first variation of the roughness parameter, $\delta\eta$.

The change in the forward operator, Δh, is approximated using the first variation, δh, given by, where $h(A_t) : \Re^n \longrightarrow \Re^m$ is the mapping from the model space,$\Re^n$, to the observation space, $\Re^m$.

$$\Delta h = \delta h = D_A (h)\, \delta A \tag{6.35}$$

For the case where the observation and state variable represent the same quantity,

$$h(A(t)) = A(t) \tag{6.36}$$

Therefore,

$$D_A\left(h\right)) = I \tag{6.37}$$

where I is the identity matrix. Therefore, 6.35 is reduced to

$$\delta h = \delta A \tag{6.38}$$

$$e_f(t_i) \equiv z(t_i) - A(t_i) = \delta h \tag{6.39}$$

Finally, by setting 6.34 equal to 6.39 results in the following relationship,

$$D_\eta\left(A\right)\delta\eta = e_f(t_i) \tag{6.40}$$

Then, 6.40 can further be expanded to handle multiple observations by using the sensitivity matrix calculated at each time step. This is shown below using the sensitivity for sequential times,

$$\begin{bmatrix} D_\eta(A)_0 \\ D_\eta(A)_1 \\ \vdots \\ D_\eta(A)_k \\ D_\eta(A)_{k+1} \\ \vdots \\ D_\eta(A)_N \end{bmatrix} \{\delta\eta\} = \begin{bmatrix} (e_f)_0 \\ (e_f)_1 \\ \vdots \\ (e_f)_k \\ (e_f)_{k+1} \\ \vdots \\ (e_f)_N \end{bmatrix} \tag{6.41}$$

The least squares problem is then solved using the LSQR algorithm (Paige and Saunders, 1983) based on the conjugate gradient method. The LSQR

algorithm can handle large sparse matrices with under-determined, uniquely determined, and overdetermined least squares problems. The LSQR method also allows for damping function to handle ill-conditioned problems. The basic least squares problem solved by LSQR is for the over-determined case where the observations, n, are greater than the number of parameters,

$$D_\eta^T D_\eta \delta\eta = D_\eta^T e_f \tag{6.42}$$

6.2.4 Calibration and Validation

Experiments are performed using the Brays Bayou operational distributed hydrologic model presented in Chapter 5. The events used that had sufficient observed data (Vieux and Bedient, 2004) for data assimilation are,

Table 6.1: Events used for parameter estimation

Event	Mean Field Bias	Rainfall Depth (mm)[1]
TSA1	1.08	39.6
TSA2	0.44	74.3
Frances	1.48	163.4
1998-01-06	1.71	54.6
1998-01-21	1.22	55.1
2002-08-15	0.84	108.7

[1] Depth in (mm) is computed from adjusted radar above Main Street

White et al. (2003) provided a method that considered a scalar adjustment method for calibrating a distributed hydrologic method. The forward sensitivity method builds on this method by adjusting the parameter estimates using a vector of adjustments. A comparison is performed between the results of the scalar method with the vector approach.

6.2.4.1 A-priori Roughness Parameter Estimate

The overland flow is modeled using Manning's roughness interpreted from land use/cover maps of the watershed. For overland cells, roughness values are estimated using tabulated values reported by landuse type (Engman, 1986). Spatial datasets of landuse type are obtained from the National Land Cover Database (NLCD, 2001). Landuse classifications contained in the NLCD are then reclassified to maps of overland roughness coefficients using lookup tables based on Engman (1986). Channel cells are defined at locations in the watershed consistent with networks contained in the National Hydrography Dataset (NHD) GIS database. Roughness values for channel cells are estimated from lookup tables provided by Chow (1959), Barnes (1967), and from previous modeling studies (Vieux et al. 2004b).

Spatially distributed parameter adjustment (SD) determines the spatial distribution of parameter adjustments using the evolution of sensitivities determined by the distributed hydrologic model dynamics. The method relies on determining the number of parameter groups that represent the hydrologic characteristics of a watershed. One criticism of distributed hydrologic models has been the argument of over parameterization. Over parameterization occurs as a model has too many parameters that cannot be identified. Within distributed hydrologic models there can easily be greater than 100,000 parameters within the model. However, we usually only have measurements at a few stream gauges within the watershed.

K-Folds Cross Validation (Efron and Tibshirani, 1995) is a technique for determining the predictive error of a model (Figure 6.3). The technique involves withholding a set of data from the model calibration procedure which

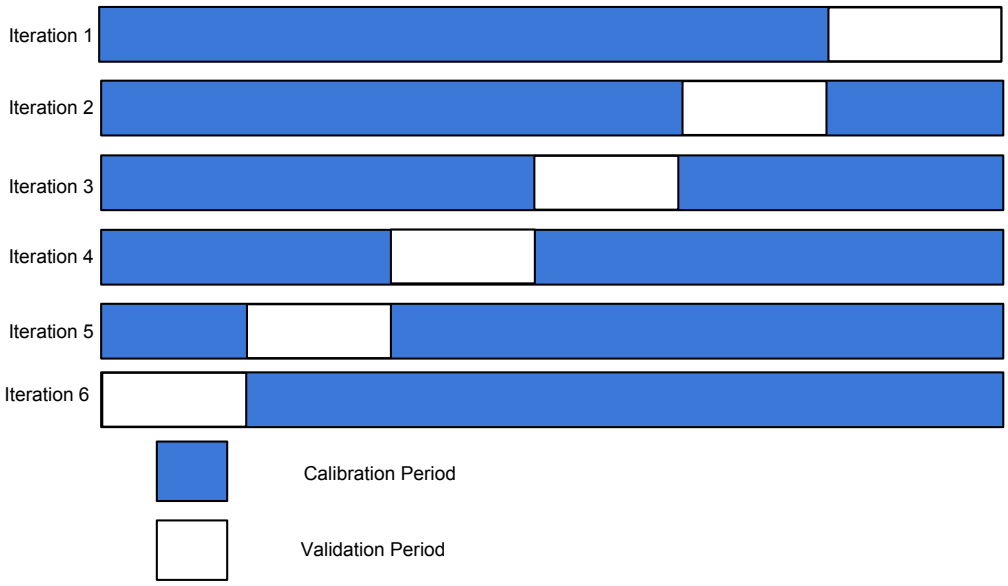

Figure 6.3: K-Folds description

will be used to calculate validation statistics. For this study, I have sequentially used the FSM calibration technique to estimate model parameters for five of the six events. This procedure was performed for each combination of five events. The sixth event was used each time to calculate the predictive error measured in RMSE (m^2).

6.3 Results and Discussion

6.3.1 Simulation Results

We tested the difference between the spatially uniform adjustment method (P=1) and the spatially distributed adjustment method for groups of $P = \{10, 20, 100\}$. Figures 6.4 and 6.5 show the final K-Folds verification hydrographs for the USGS streamflow gauges at Main St. and Gessner respectively. The top three panels of each figure show the results for P=10,20,100 while the bottom panel shows the spatially uniform adjustment method (P=1). The

main observation from the figures is that P=1 consistently over estimates the peak discharge. The cause is due to the restriction that only one multiplier is used for the entire roughness map. The hydrographs for P=1 are unbiased, in the sense that there are an equal amount of residuals greater than and less than the observed hydrograph. However, when the roughness multiplier is overly constrained and not allowed to adjust each group of roughness values then the peak discharge is over estimated.

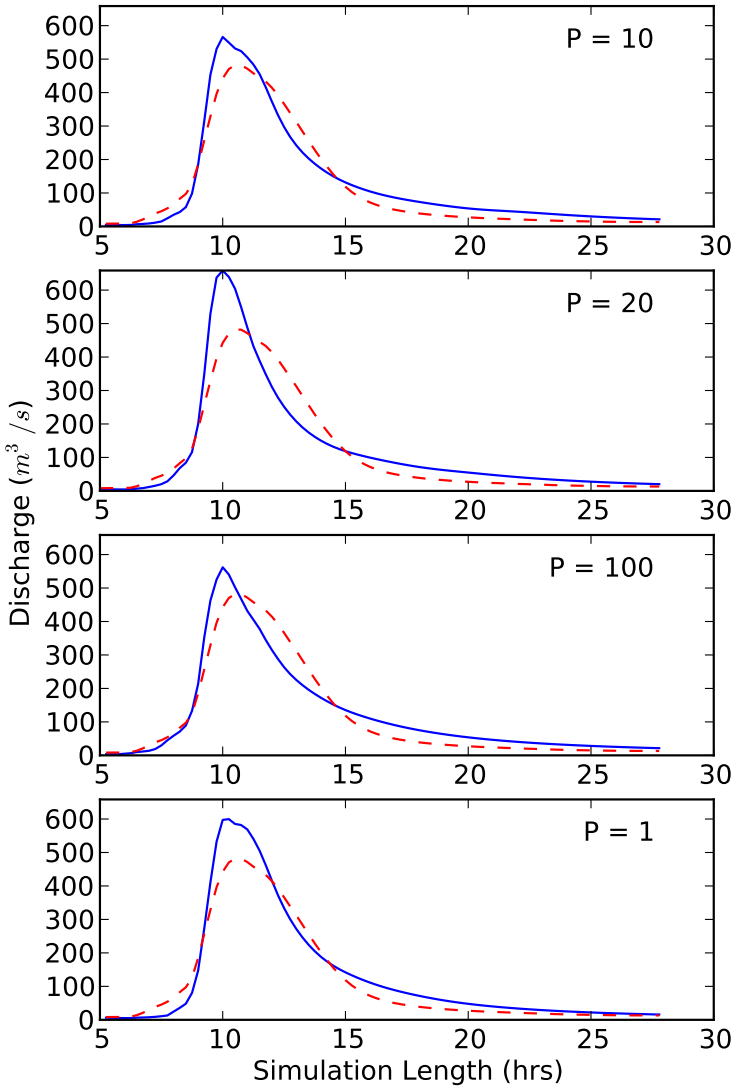

(a)

Figure 6.4: Verification hydrographs for Main St. USGS Gauge a) Tropical Storm Allison (TSA1), b)Tropical Storm Allison (TSA2), c) August 15, 2002, d) Frances, e) January 6, 1998 f) January 21, 1998

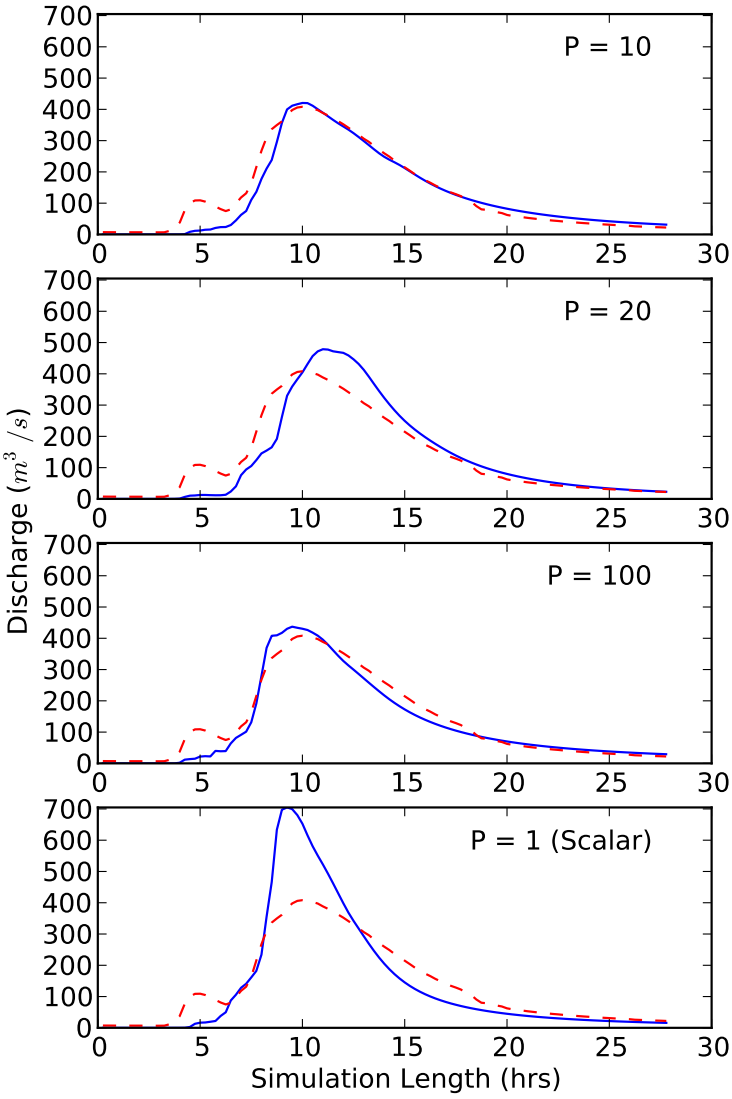

(b)

Figure 6.4: Verification hydrographs for Main St. USGS Gauge a) Tropical Storm Allison (TSA1), b)Tropical Storm Allison (TSA2), c) August 15, 2002, d) Frances, e) January 6, 1998 f) January 21, 1998

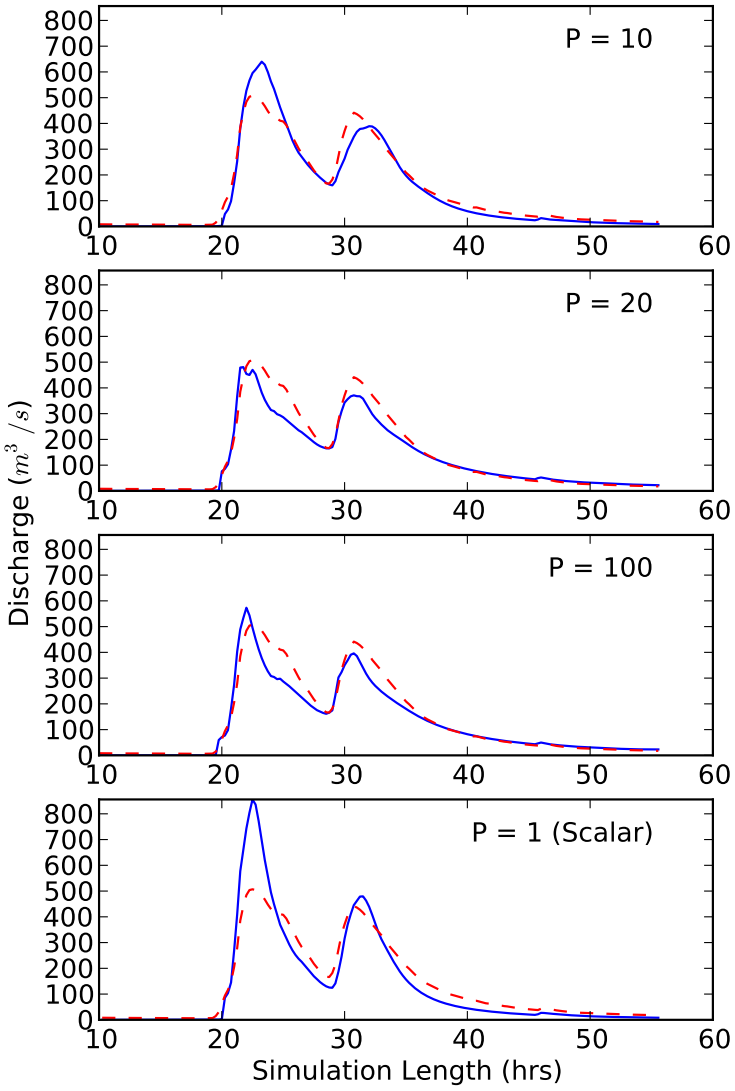

(c)

Figure 6.4: Verification hydrographs for Main St. USGS Gauge a) Tropical Storm Allison (TSA1), b)Tropical Storm Allison (TSA2), c) August 15, 2002, d) Frances, e) January 6, 1998 f) January 21, 1998

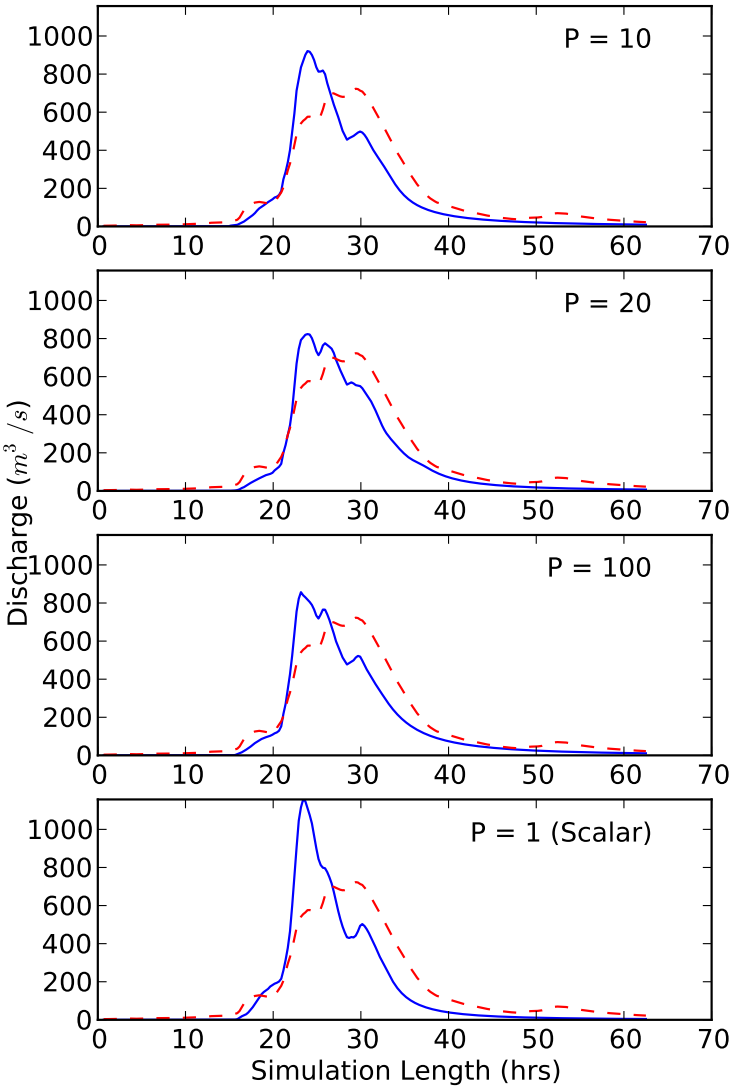

(d)

Figure 6.4: Verification hydrographs for Main St. USGS Gauge a) Tropical Storm Allison (TSA1), b)Tropical Storm Allison (TSA2), c) August 15, 2002, d) Frances, e) January 6, 1998 f) January 21, 1998

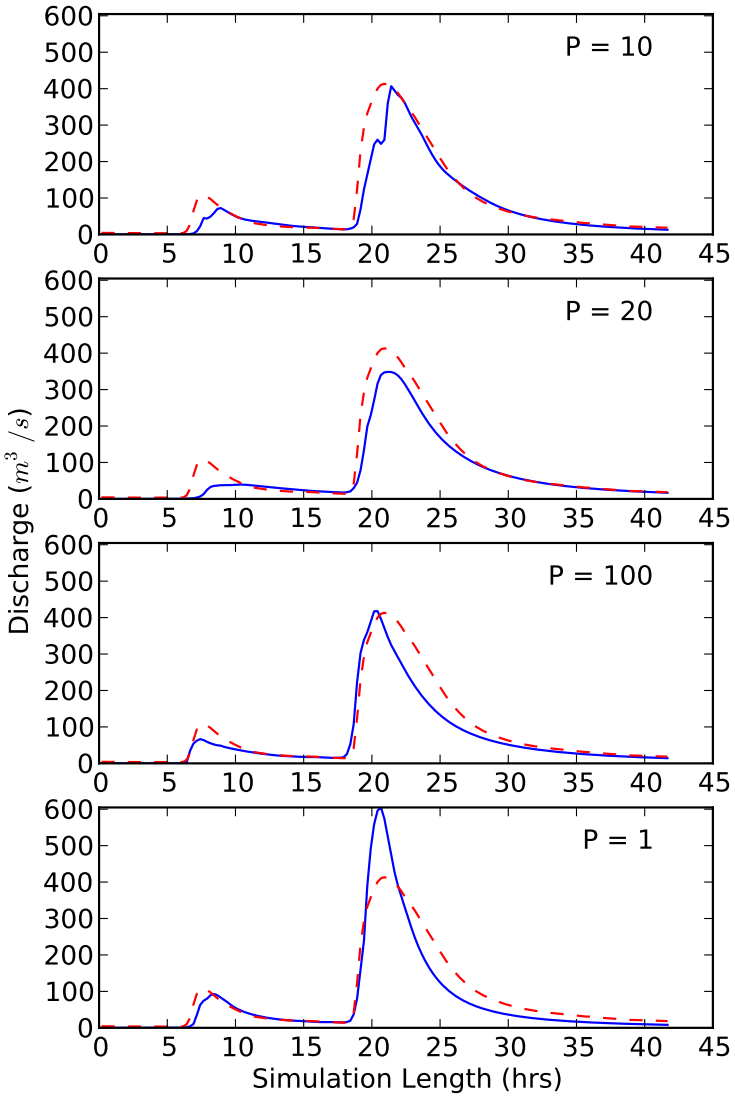

(e)

Figure 6.4: Verification hydrographs for Main St. USGS Gauge a) Tropical Storm Allison (TSA1), b)Tropical Storm Allison (TSA2), c) August 15, 2002, d) Frances, e) January 6, 1998 f) January 21, 1998

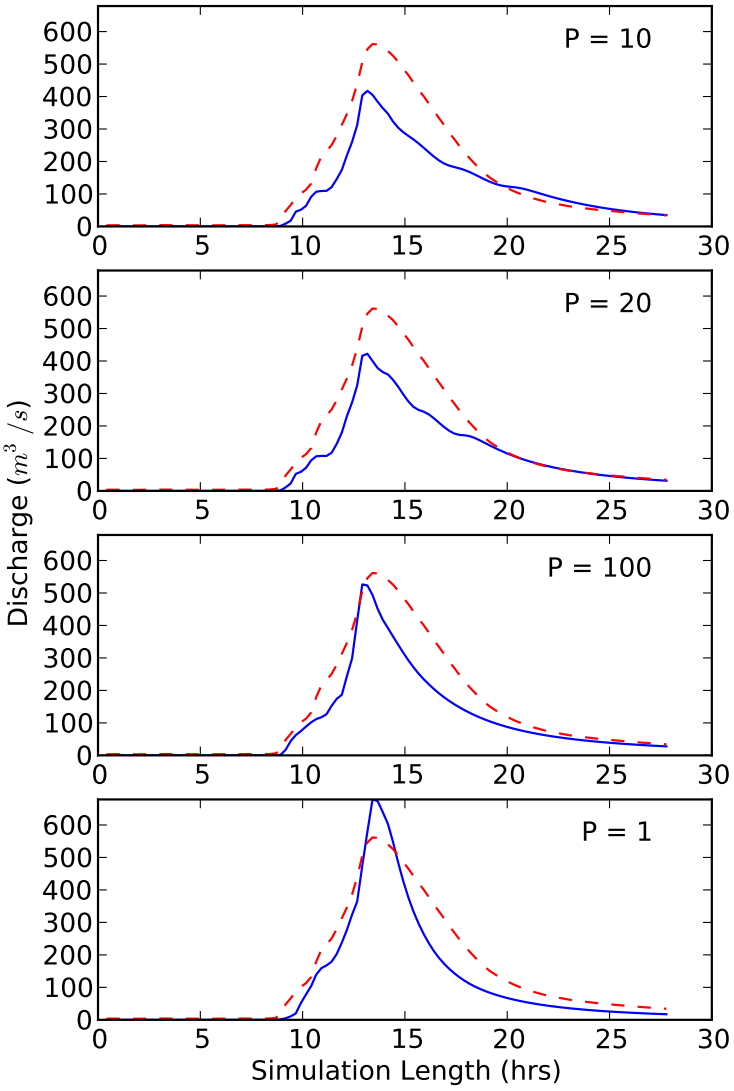

(f)

Figure 6.4: Verification hydrographs for Main St. USGS Gauge a) Tropical Storm Allison (TSA1), b)Tropical Storm Allison (TSA2), c) August 15, 2002, d) Frances, e) January 6, 1998 f) January 21, 1998

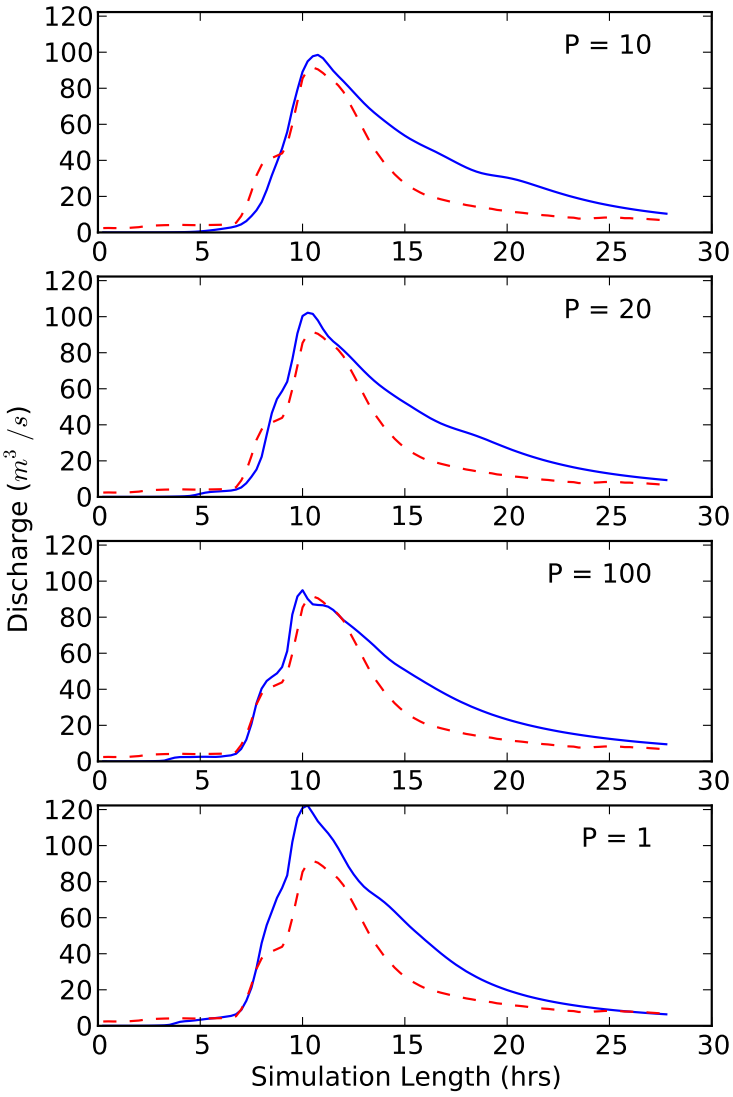

(a)

Figure 6.5: Verification hydrographs for Gessner USGS Gauge a) Tropical Storm Allison (TSA1), b)Tropical Storm Allison (TSA2), c) August 15, 2002, d) Frances, e) January 6, 1998 f) January 21, 1998

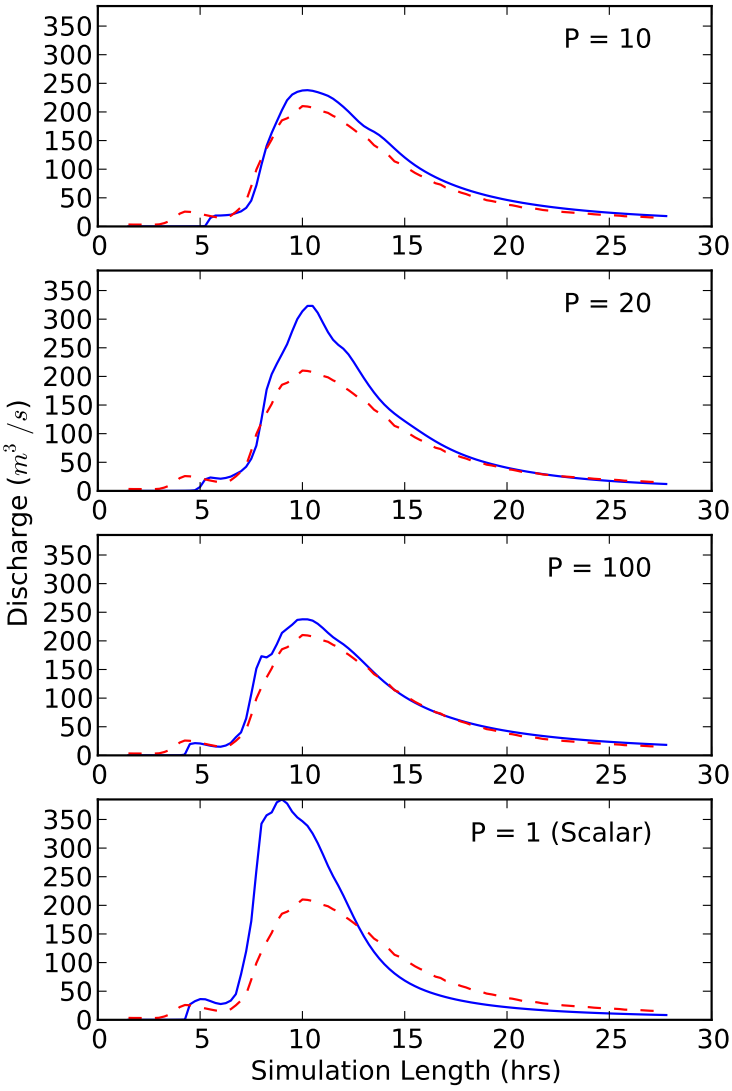

(b)

Figure 6.5: Verification hydrographs for Gessner USGS Gauge a) Tropical Storm Allison (TSA1), b)Tropical Storm Allison (TSA2), c) August 15, 2002, d) Frances, e) January 6, 1998 f) January 21, 1998

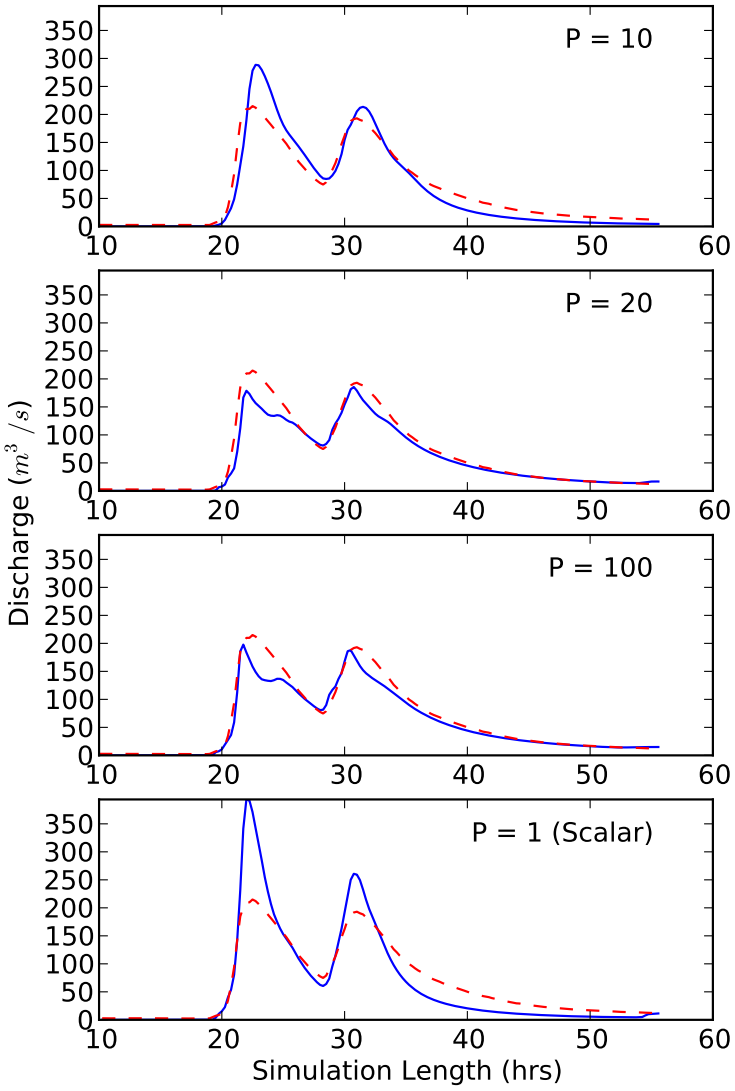

(c)

Figure 6.5: Verification hydrographs for Gessner USGS Gauge a) Tropical Storm Allison (TSA1), b)Tropical Storm Allison (TSA2), c) August 15, 2002, d) Frances, e) January 6, 1998 f) January 21, 1998

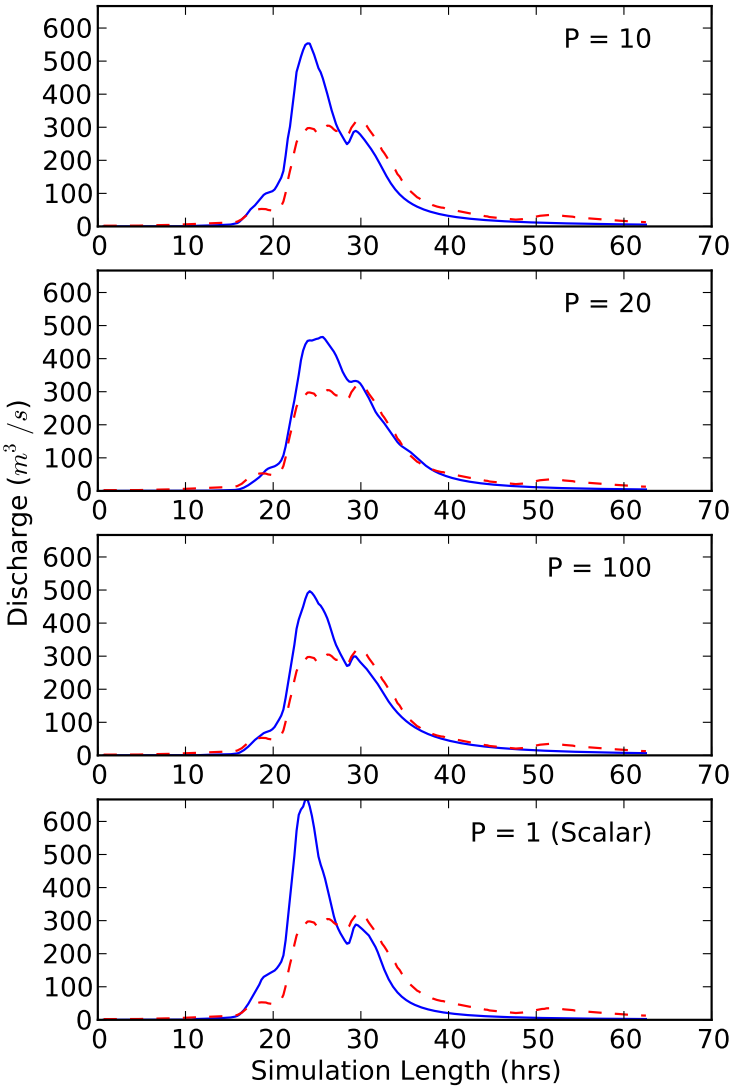

(d)

Figure 6.5: Verification hydrographs for Gessner USGS Gauge a) Tropical Storm Allison (TSA1), b)Tropical Storm Allison (TSA2), c) August 15, 2002, d) Frances, e) January 6, 1998 f) January 21, 1998

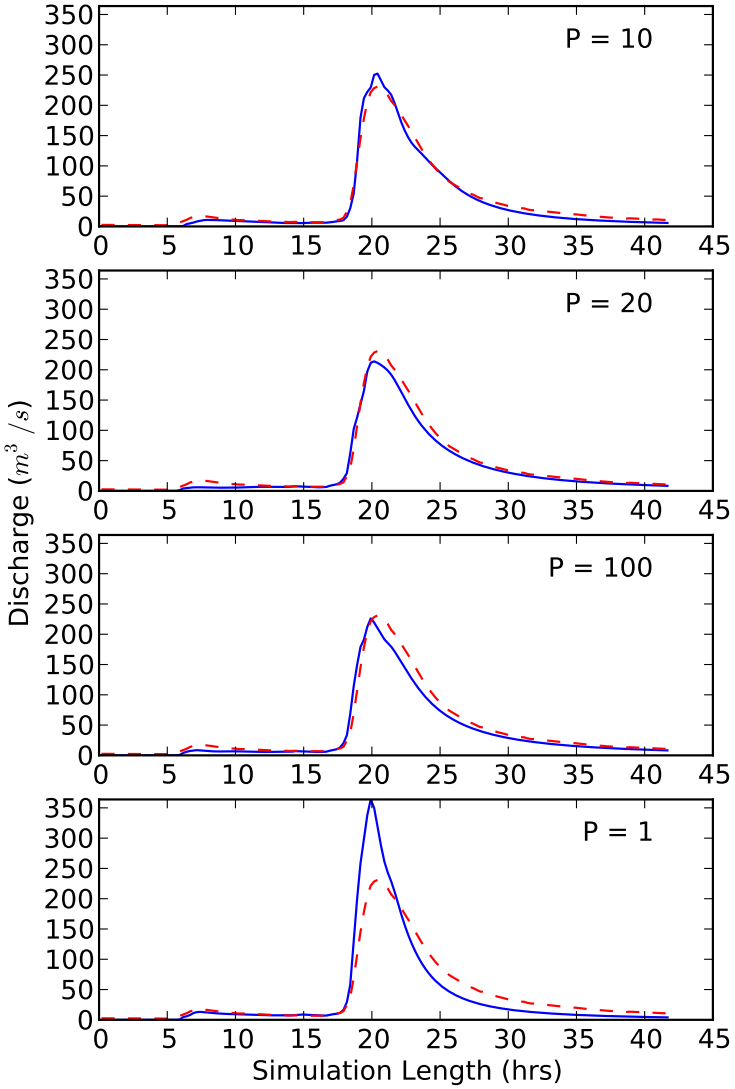

(e)

Figure 6.5: Verification hydrographs for Gessner USGS Gauge a) Tropical Storm Allison (TSA1), b)Tropical Storm Allison (TSA2), c) August 15, 2002, d) Frances, e) January 6, 1998 f) January 21, 1998

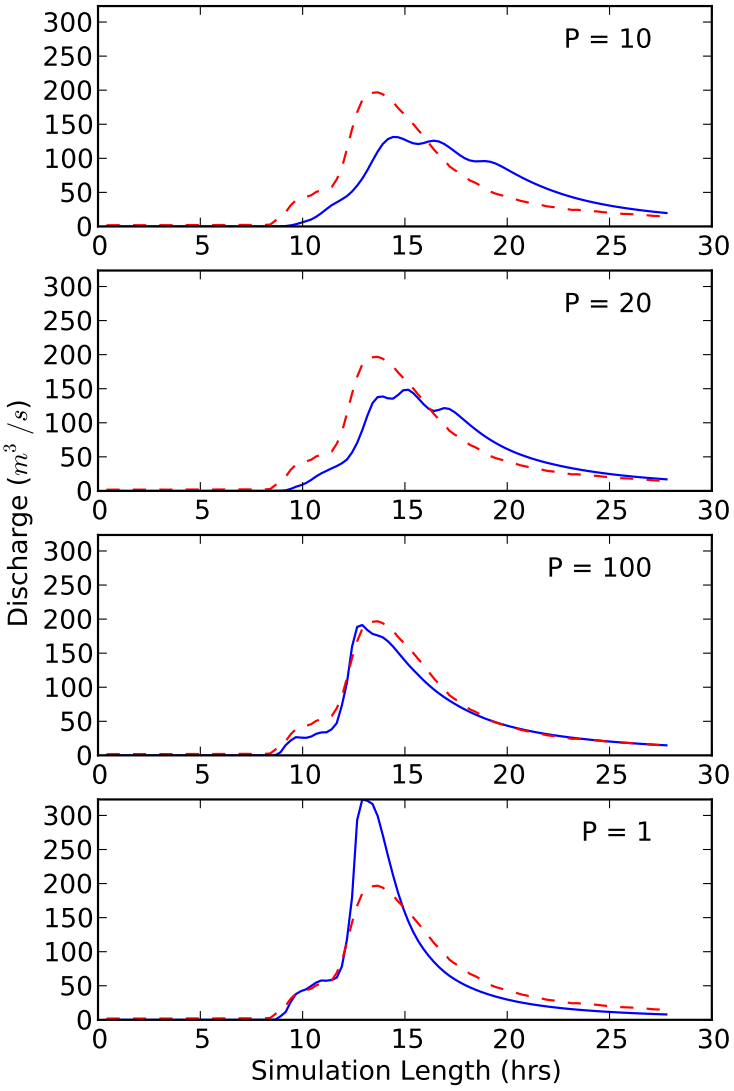

(f)

Figure 6.5: Verification hydrographs for Gessner USGS Gauge a) Tropical Storm Allison (TSA1), b)Tropical Storm Allison (TSA2), c) August 15, 2002, d) Frances, e) January 6, 1998 f) January 21, 1998

6.3.2 Prediction Error

The next step is to test the hypothesis is to estimate the hydraulic roughness parameter for the basin by adjusting a multiplier of hydraulic roughness. Then the runoff at interior gauge location (Gessner) can be used as an independent verification point. The hypothesis test will be performed using the Mann-Whitney-Wilcoxon (MWW) ranksum test with $\alpha = 0.05$. The MWW ranksum test is a nonparametric test that doesn't assume normality.

H_0: Null Hypothesis

The mean prediction error, measured as RMSE, from the model calibrated for $P = 1$ will be equal to or less than the prediction error from the model calibrated for $P > 1$.

H_A: Alternative Hypothesis

The mean prediction error, measured as RMSE, from the model calibrated for $P = 1$ will be greater than the prediction error from the model calibrated for $P > 1$.

The hypothesis test will be performed between P=1 and P = $\{10, 20, 100\}$ for both the Main St. and Gessner gauges.

6.3.2.1 Gessner Hypothesis Tests

Test 1: Comparing P=1 and P=10

Using the Mann-Whitney-Wilcoxon ranksum for a one sided test (1- α), the z-statistic is 2.79 with a p-value of 0.0026. Therefore, the null hypothesis can be rejected between P=1 and P=10.

Test 2: Comparing P=1 and P=20

Using the Mann-Whitney-Wilcoxon ranksum for a one sided test (1- α),

the z-statistic is 3.05 with a p-value of 0.0011. Therefore, the null hypothesis can be rejected between P=1 and P=20.

Test 3: Comparing P=1 and P=100

Using the Mann-Whitney-Wilcoxon ranksum for a one sided test (1- α), the z-statistic is 3.21 with a p-value of 0.0007. Therefore, the null hypothesis can be rejected between P=1 and P=100.

6.3.2.2 Main St. Hypothesis Tests

Test 1: Comparing P=1 and P=10

Using the Mann-Whitney-Wilcoxon ranksum for a one sided test (1- α), the z-statistic is 2.97 with a p-value of 0.00148. Therefore, the null hypothesis can be rejected between P=1 and P=10.

Test 2: Comparing P=1 and P=20

Using the Mann-Whitney-Wilcoxon ranksum for a one sided test (1- α), the z-statistic is 2.88 with a p-value of 0.00197. Therefore, the null hypothesis can be rejected between P=1 and P=20.

Test 3: Comparing P=1 and P=100

Using the Mann-Whitney-Wilcoxon ranksum for a one sided test (1- α), the z-statistic is 3.178 with a p-value of 0.00074. Therefore, the null hypothesis can be rejected between P=1 and P=100.

The null hypothesis is that a scalar adjustment would have a smaller mean prediction error measured by the root mean square error of cross sectional flow area. Therefore, the null hypothesis can be rejected based on the results for both Main St. and Gessner with a significance level of 95%. Also, Tables 6.2 and 6.3 show the confidence intervals on the RMSE prediction error from the model. The RMSE is thus less when $P > 1$. Therefore, these results show

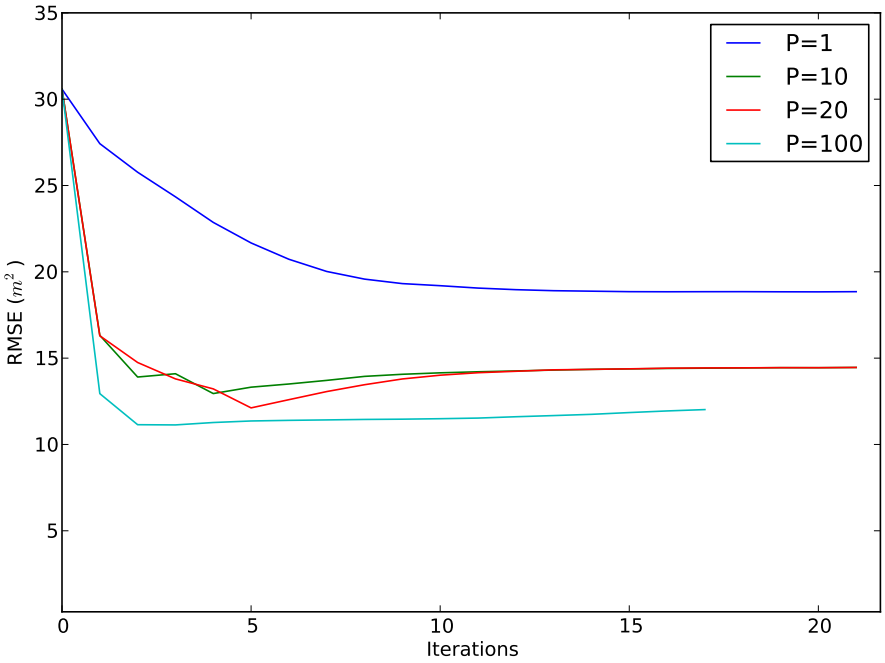

Figure 6.6: RMSE (m^2) convergence speed for Gessner

that a spatially distributed parameter adjustment outperforms the spatially average parameter adjustment (P=1).

Table 6.2: RMSE (m^2) for Gessner predictions of K-Folds Cross Validation Results with bootstrap confidence intervals

Vector Dimension (P)	Mean	Lower CI (95%)	Upper CI (95%)
1 (Scalar)	18.85	16.92	20.91
10	14.56	13.25	16.21
20	14.46	13.28	15.76
100	12.02	11.20	13.03

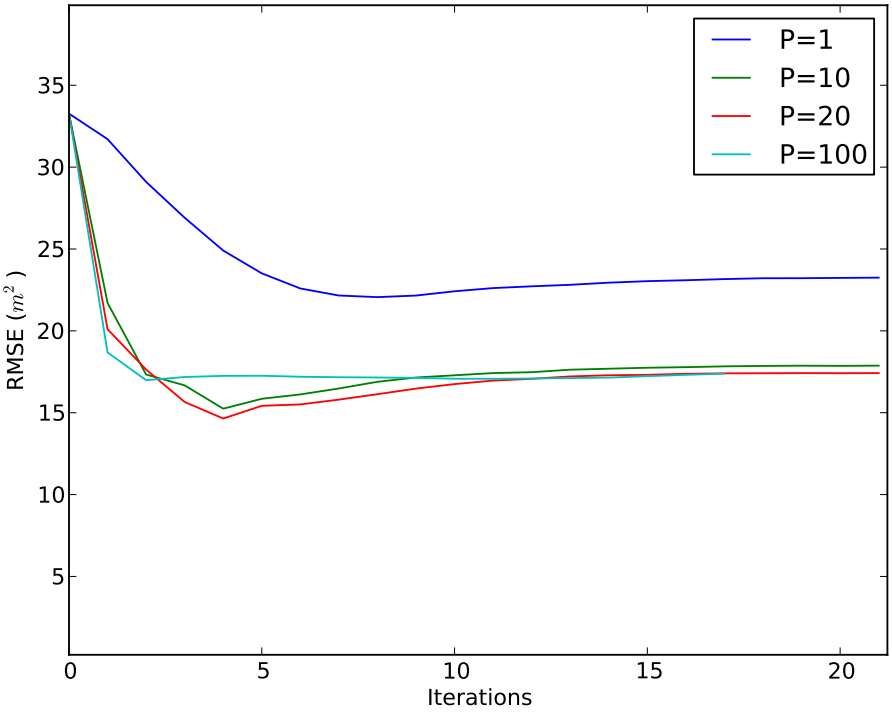

Figure 6.7: RMSE (m^2) convergence speed for Main St.

Table 6.3: RMSE (m^2) for Main St predictions of K-Folds Cross Validation Results with bootstrap confidence intervals

Vector Dimension (P)	Mean	Lower CI (95%)	Upper CI (95%)
1 (Scalar)	23.25	20.76	25.95
10	17.87	15.95	20.24
20	17.84	16.11	19.86
100	17.42	15.68	19.32

Table 6.4: NSE for Gessner predictions of K-Folds Cross Validation Results with bootstrap confidence intervals

Vector Dimension (P)	Mean	Lower CI (95%)	Upper CI (95%)
1 (Scalar)	0.54	0.45	0.59
10	0.70	0.65	0.75
20	0.70	0.64	0.75
100	0.79	0.74	0.83

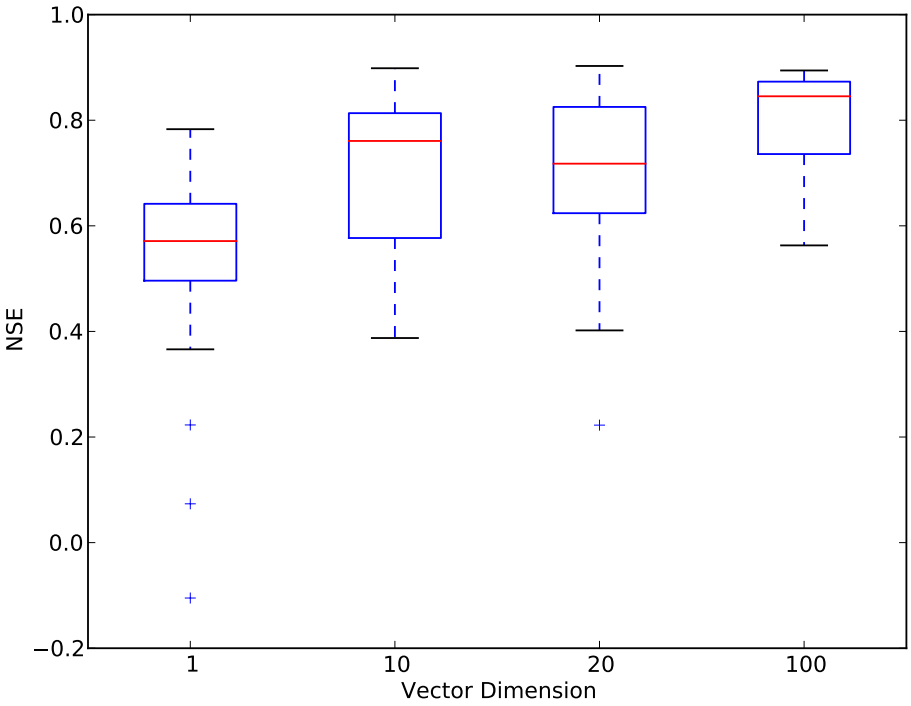

Figure 6.8: Boxplot of verification NSE for Gessner

Table 6.5: NSE for Main St predictions of K-Folds Cross Validation Results with bootstrap confidence intervals

Vector Dimension (P)	Mean	Lower CI (95%)	Upper CI (95%)
1 (Scalar)	0.76	0.71	0.80
10	0.86	0.83	0.88
20	0.86	0.83	0.88
100	0.87	0.86	0.89

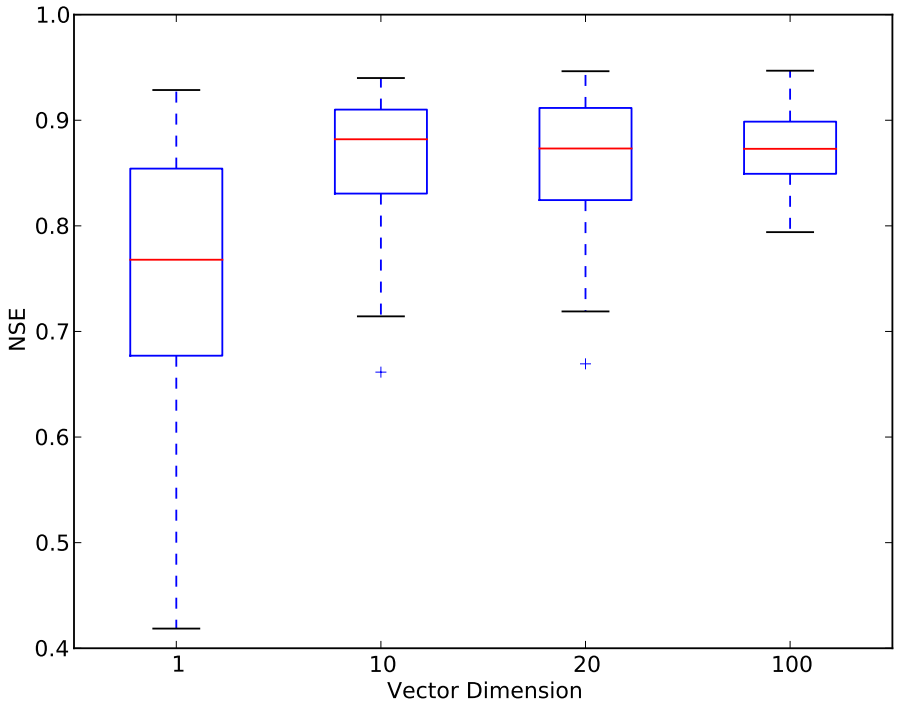

Figure 6.9: Boxplot of verification NSE for Main St.

6.4 Summary

This chapter has focused on testing the hypothesis that a model calibrated using spatially distributed parameter adjustments will have less prediction error than a model calibrated by a spatially averaged parameter adjustment. The model calibrated using spatially distributed parameter adjustments consistently had less prediction error than the model calibrated using a spatially average parameter adjustment. The results of the MWW ranksum hypothesis test showed the mean of RMSE from the model calibrated by spatially distributed adjustments is less than the RMSE from the model calibrated using the spatially average parameter adjustments. Further evidence was seen from the box plots of Nash Sutcliffe Efficiency. The Nash Sutcliffe Efficiency of the spatially distributed model was consistently higher than the spatially averaged model. These results were consistent at both the calibration gauge at Main. Street and at the interior gauge point at Gessner. These results show that the hypothesis is correct. A spatially distributed parameter adjustment technique leads to a reduction in prediction error compared with the spatially averaged parameter adjustment technique.

Chapter 7

Conclusions

The research presented within this dissertation focused on three areas identified as needing research in hydrologic modeling (National Research Council, 2002).

1. The fundamental system dynamics and propagation of perturbations,
2. Adequate characterization of model states, and
3. Procedures for generating model output with expected evolution of model states.

The objectives of this dissertation were to address these needs in hydrologic modeling by,

1. Assessing the influence of rain gauge adjustment of radar rainfall on distributed hydrologic model calibration and operational performance.
2. Developing a technique of propagating uncertainty in radar rainfall through a distributed hydrologic model.
3. Developing a technique for parameter estimation based on the evolution of forward sensitivities through a distributed hydrologic model.

The first objective was accomplished by showing the influence of rain gauge adjustment on operational flood forecasting performance (Ch. 3 and 4). The

results of the analysis showed that considerable improvements in model performance could be achieved by bias correcting operational radar rainfall input. Unbiased forcing input is required to achieve adequate operational flood forecasting performance. Biases in the input will be propagated into the parameter estimation step, and make it difficult to understand the processes occurring within the basin. The second objective focused on the propagation of perturbations in radar rainfall bias correction thru a distributed hydrologic model. This propagation showed that prediction error increases with drainage area at a nonlinear rate. The influence of bias correcting radar rainfall was also showed how the skill of the model, as measured by the Critical Skill Index (CSI), decreased with increasing drainage area. The third objective focused on the application of the Forward Sensitivity Method to understand the impacts of spatially distributed parameter estimation on flood forecasting performance.

The main hypothesis tested using the Forward Sensitivity Method was that a model calibrated using spatially distributed parameter adjustments will have less prediction error than a model calibrated by a spatially averaged parameter adjustment. A Mann-Whitney-Wilcoxon ranksum hypothesis test was used to test the statistical significance. The results of the MWW ranksum hypothesis test showed the mean of RMSE from the model calibrated by spatially distributed adjustments is less than the RMSE from the model calibrated using the spatially average parameter adjustments. Further evidence was seen from the box plots of Nash Sutcliffe Efficiency. The Nash Sutcliffe Efficiency of the spatially distributed model was consistently higher than the spatially averaged model. These results were consistent at both the calibration gauge at Main. Street and at the interior gauge point at Gessner. These results show that the hypothesis is correct. A spatially distributed parameter adjustment technique

leads to a reduction in prediction error compared with the spatially averaged parameter adjustment technique.

7.1 Recommendations

Future research stemming from this dissertation should focus on the use of data assimilation techniques that include both parameter estimation and state estimation. The Forward Sensitivity Method utilized within this dissertation provides a physically based method of estimating both empirical and physical parameters of the flood forecasting problem. Future areas of research for the Forward Sensitivity Method within distributed hydrologic modeling are,

- What advantages would the Forward Sensitivity Method provide for soil moisture state estimation compared with the commonly used Ensemble Kalman Filter?

- How can the parameters be updated automatically for precipitation estimation techniques based on Z-R relationships and dual-pol algorithms using the Forward Sensitivity Method?

- What is the best way to handle on/off switching behaviors within a data assimilation technique? Switching behaviors occur as the soil profile becomes saturated and runoff generation switches from infiltration rate excess to saturation excess.

- How can we best combine data assimilation techniques such as the EnKF with the FSM to provide both a stochastic and deterministic viewpoint on both parameter and state estimation?

References

Abbott, M. B., Bathurst, J. C., Cunge, J. A., O'Connell, P. E., and Rasmussen, J. (1986a). An Introduction to European Hydrological System -Systeme Hydrologique European, "SHE", 1 History and philosophy of a physically-based distributed modeling system. *Journal of Hydrology*, 87:45–59.

Abbott, M. B., Bathurst, J. C., Cunge, J. A., O"Connell, P. E., and Rasmussen, J. (1986b). An Introduction to the European Hydrological System-Systeme Hydrologique European, "SHE", 2: Structure of a Physically-Based Distributed Modeling System. *Journal of Hydrology*, 87:61–77.

Allen, R. G., Smith, M., Pereira, L. S., and Perrier, A. (1994). An update for the calculation of reference evaporation. *ICID Bulletin*, 43:35–92.

Anquetin, S., Braud, I., Vannier, O., Viallet, P., Boudevillain, B., Creutin, J.-D., and Manus, C. (2010). Sensitivity of the hydrological response to the variability of rainfall fields and soils for the gard 2002 flash-flood event. *Journal of Hydrology*, 394(1):134–147.

ASCE Task Committee on Definition of Criteria for Evaluation of Watershed Models of the Watershed Management Committee, Irrigation and Drainage Division (1993). Criteria for evaluation of watershed models. *Journal of Irrigation and Drainage Engineering*, 119(3):429–442.

Atlas, D., Harper, W. G., Ludham, F. H., and Macklin, W. C. (1960). Radar Scatter by Large Hail. *Q. J*, pages 468–482.

Barnes, H. W. (1967). Roughness characteristics of natural channels. *U.S. Geological Survey, Water Supply Paper*, 1849.

Barnes, S. L. (1964). A technique for maximizing details in numerical weather map analysis. *Journal of Applied Meteorology*, 3(4):396–409.

Bedient, P. B., Holder, A., Benavides, J., and Vieux, B. (2003). Radar-Based Flood Warning System Applied to Tropical Storm Allison. *American Society of Civil Engineers, Journal of Hydrologic Engineering*, 8(6):308–318.

Bedient, P. B., Huber, W. C., and Vieux, B. E. (2008). *Hydrology and floodplain analysis*. Prentice Hall.

Beven, K. (2008). *Environmental Modelling: An Uncertain Future?* Taylor & Francis, Routledge.

Borga, M., Anagnostou, E., Blöschl, G., Creutin, J., et al. (2010). Flash floods: Observations and analysis of hydro-meteorological controls. *Journal of Hydrology*, 394:1–3.

Bouilloud, L., Delrieu, G., Boudevillain, B., and Kirstetter, P.-E. (2010). Radar rainfall estimation in the context of post-event analysis of flash-flood events. *Journal of Hydrology*, 394(1):17–27.

Brock, F. V., Crawford, K. C., Elliott, R. L., Cuperus, G. W., Stadler, S. J., Johnson, H. L., and Eilts, M. D. (1995). The oklahoma mesonet: a technical overview. *Journal of Atmospheric and Oceanic Technology*, 12(1):5–19.

Carpenter, T. M. and Georgakakos, K. P. (2004). Impacts of parametric and radar rainfall uncertainty on the ensemble streamflow simulations of a distributed hydrologic model. *Journal of Hydrology*, 298(1):202–221.

Castaings, W., Dartus, D., Le Dimet, F.-X., Saulnier, G.-M., et al. (2009). Sensitivity analysis and parameter estimation for distributed hydrological modeling: potential of variational methods. *Hydrology and Earth System Sciences Discussions*, 13:503–517.

Chow, V. (1959). Open-channel hydraulics. *McGraw-Hill civil engineering series*.

Chumchean, S., Sharma, A., and Seed, A. (2003). Radar rainfall error variance and its impact on radar rainfall calibration. *Physics and Chemistry of the Earth, Parts A/B/C*, 28(1):27–39.

Ciach, G. J., Habib, E., and Krajewski, W. F. (2003). Zero-covariance hypothesis in the error variance separation method of radar rainfall verification. *Advances in Water Resources*, 26(5):573–580.

Ciach, G. J. and Krajewski, W. F. (2006). Analysis and modeling of spatial correlation structure in small-scale rainfall in Central Oklahoma. *Advances in water resources*, 29(10):1450–1463.

Clark, M. P., Rupp, D. E., Woods, R. A., Zheng, X., Ibbitt, R. P., Slater, A. G., Schmidt, J., and Uddstrom, M. J. (2008). Hydrological data assimilation with the ensemble kalman filter: Use of streamflow observations to update states in a distributed hydrological model. *Advances in Water Resources*, 31:1309–1324.

Collier, C. (1986). Accuracy of rainfall estimates by radar, part ii: comparison with raingauge network. *Journal of Hydrology*, 83(3):225–235.

Creutin, J. D., Borga, M., Lutoff, C., Scolobig, A., Ruin, I., and Créton-Cazanave, L. (2009). Catchment dynamics and social response during flash floods: the potential of radar rainfall monitoring for warning procedures. *Meteorological applications*, 16(1):115–125.

Cunge, J. A., Jr., F. M. H., and Verwey, A. (1980). Practical Aspects of Computational River Hydraulics. *Pitman London*, pages 23–24.

Desai, C. S. (1979). Elementary finite element method. *Civil Engineering and Engineering Mechanics Series, Englewood Cliffs: Prentice-Hall, 1979*, 1.

Ding, Y., Jia, Y., and Wang, S. S. (2004). Identification of manning's roughness coefficients in shallow water flows. *Journal of Hydraulic Engineering*, 130(6):501–510.

Dooge, J. C. and O'Kane, J. P. (2003). *Deterministic Methods in Systems Hydrology*. Taylor & Francis Group.

Doviak, R. J. and Zrni, D. S. (1993). *Doppler Radar and Weather Observations*. Dover Publications.

Downer, C. W. and Ogden, F. L. (2004). GSSHA: Model to simulate diverse stream flow producing processes. *Journal of Hydrologic Engineering*, 9(3):161–174.

Einfalt, T., Arnbjerg-Nielsen, K., Golz, C., Jensen, N.-E., Quirmbach, M., Vaes, G., and Vieux, B. (2004). Towards a roadmap for use of radar rainfall data in urban drainage. *Journal of Hydrology*, 299(3):186–202.

Engman, E. T. (1986). Roughness coefficients for routing surface runoff. *Journal of Irrigation and Drainage Engineering*, 112(1):39–53.

Evensen, G. (2003). The ensemble kalman filter: theoretical formulation and practical implementation. *Ocean Dynamics*, 53:343–367.

Evensen, G. (2009). *Data Assimilation: The Ensemble Kalman Filter*. Springer-Verlag New York, Inc.

Fang, X. and Su, D. (2006). An integrated one-dimensional and two-dimensional urban stormwater flood simulation model. *JAWRA Journal of the American Water Resources Association*, 42(3):713–724.

Freeze and Nichols (1994). Dam failure study for upper reaches of illinois river.

Fulton, R. A., Breidenbach, J. P., Seo, D.-J., Miller, D. A., and O'Bannon, T. (1998). The WSR-88D rainfall algorithm. *Weather and Forecasting*, 13(2):377–395.

Garbrecht, J., Liew, M. V., and Brown, G. (2004). Trends in precipitation, streamflow, and evapotranspiration in the Great Plains of the United States. *Journal of Hydrologic Engineering*, 9(5):360–367.

Georgakakos, K. P. (1986). A generalized stochastic hydrometeorological model for flood and flash-flood forecasting. *Water Resources Research*, 22(13):2083–2095.

Gourley, J. J. and Vieux, B. E. (2005). A method for evaluating the accuracy of quantitative precipitation estimates from a hydrologic modeling perspective. *Journal of Hydrometeorology*, 6(2):115–133.

Gourley, J. J. and Vieux, B. E. (2006). A method for identifying sources of model uncertainty in rainfall-runoff simulations. *Journal of Hydrology*, 327(1):68–80.

Gupta, H. V., Kling, H., Yilmaz, K. K., and Martinez, G. F. (2009). Decomposition of the mean squared error and NSE performance criteria: Implications for improving hydrological modelling. *Journal of Hydrology*, 377(1):80–91.

Gupta, H. V., Sorooshian, S., and Yapo, P. O. (1998). Toward improved calibration of hydrologic models: Multiple and noncommensurable measures of information. *Water Resources Research*, 34(4):751–763.

H, W. A., J, S. D., M, W., and J, S. (2010). Operational hydrological ensemble forecasting. In *To appear in Applied uncertainty analysis for flood risk management edited by K Beven and J Hall*.

Habib, E., Aduvala, A. V., and Meselhe, E. A. (2008a). Analysis of radar-rainfall error characteristics and implications for streamflow simulation uncertainty. *Hydrological sciences journal*, 53(3):568–587.

Habib, E., Ciach, G. J., and Krajewski, W. F. (2004). A method for filtering out raingauge representativeness errors from the verification distributions of radar and raingauge rainfall. *Advances in water resources*, 27(10):967–980.

Habib, E., Malakpet, C. G., Tokay, A., and Kucera, P. A. (2008b). Sensitivity of streamflow simulations to temporal variability and estimation of Z–R relationships. *Journal of Hydrologic Engineering*, 13(12):1177–1186.

Harmel, R. D. (1997). *Analysis of bank erosion on the Illinois River in Northeast Oklahoma*. PhD diss, Oklahoma State University.

Honnorat, M., Monnier, J., and Le Dimet, F.-X. (2009). Lagrangian data assimilation for river hydraulics simulations. *Computing and visualization in science*, 12(5):235–246.

James, L. D. and Burges, S. J. (1982). *Selection, calibration, and testing of hydrologic models*. 435-472, Hydrologic modeling of small watersheds 5.

Janek, S., Oswald, G., and Vieux, B. (2006). Real-Time Stormwater Management using Depth, Duration, Frequency Thresholds. In *Proceedings of the Water Environment Federation 2006*, pages 3757–3768. no. 9 :no. 9.

Jayawardena, A. and White, J. (1977). A finite element distributed catchment model, i. analytical basis. *Journal of Hydrology*, 34(3):269–286.

Julien, P. Y. and Saghafian, B. (1991). *CASC2D user's manual: A two-dimensional watershed rainfall-runoff model*. Colorado State University, Center for Geosciences, Hydrologic Modeling Group.

Koren, V., Reed, S., Smith, M., Zhang, Z., and Seo, D.-J. (2004). Hydrology laboratory research modeling system (HL-RMS) of the US national weather service. *Journal of Hydrology*, 291(3):297–318.

Koren, V., Schaake, J., Duan, Q., Smith, M., and Cong, S. (1998). PET upgrades to NWSRFS Project Plan. Washington, DC, unpublished report.

Lakshmivarahan, S. and Lewis, J. (2010). Forward sensitivity approach to dynamic data assimilation. *Advances in Meteorology*.

Le Dimet, F. and Talagrand, O. (1986). Variational algorithms for analysis and assimilation of meteorological observations: theoretical aspects. *Tellus A*, 38(2):97–110.

Looper, J. P. and Vieux, B. E. (2012). An assessment of distributed flash flood forecasting accuracy using radar and rain gauge input for a physics-based distributed hydrologic model. *Journal of Hydrology*, 412:114–132.

Looper, J. P. and Vieux, B. E. (2013). Distributed Hydrologic Forecast Reliability Using Next-Generation Radar. *Journal of Hydrologic Engineering*, 18(2):260–268.

Looper, J. P., Vieux, B. E., and Moreno, M. A. (2012). Assessing the impacts of precipitation bias on distributed hydrologic model calibration and prediction accuracy. *Journal of Hydrology*, 418:110–122.

Mandapaka, P. V., Krajewski, W. F., Ciach, G. J., Villarini, G., and Smith, J. A. (2009). Estimation of radar-rainfall error spatial correlation. *Advances in Water Resources*, 32(7):1020–1030.

Marshall, J. S. and Palmer, W. M. K. (1948). The distribution of raindrops with size. *Journal of Meteorology*, 5(4):165–166.

Marzen, J. and Fuelberg, H. (2005). Developing a high resolution precipitation dataset for Florida hydrologic studies. In *19th Conference on Hydrology*.

Mimikou, M. and Baltas, E. (1996). Flood forecasting based on radar rainfall measurements. *Journal of Water Resources Planning and Management*, 122(3):151–156.

Moll, J. R. (1986). Short range flood forecasting on the river rhine. *River Flow Modelling and Forecasting*, pages 287–297.

Morin, J., Rosenfeld, D., and Amitai, E. (1995). Radar rain field evaluation and possible use of its high temporal and spatial resolution for hydrological purposes. *Journal of Hydrology*, 172(1):275–292.

National Research Council (2002). *Report of a Workshop on Predictability and Limits-To-Prediction in Hydrologic Systems*. The National Academies Press.

Norbiato, D., Borga, M., Degli Esposti, S., Gaume, E., and Anquetin, S. (2008). Flash flood warning based on rainfall thresholds and soil moisture conditions: An assessment for gauged and ungauged basins. *Journal of Hydrology*, 362(3):274–290.

Ogden, F. L. and Julien, P. Y. (1993). Runoff sensitivity to temporal and spatial rainfall variability at runoff plane and small basin scales. *Water resources research*, 29(8):2589–2597.

Ogden, F. L. and Julien, P. Y. (1994). Runoff model sensitivity to radar rainfall resolution. *Journal of Hydrology*, 158(1):1–18.

Olivera, F. and Maidment, D. R. (2000). GIS tools for HMS modeling support. In *19th Annual ESRI International User Conference. Julho*, pages 26–30.

Oudin, L., Perrin, C., Mathevet, T., Andrassian, V., and Michel, C. (2006). Impact of biased and randomly corrupted inputs on the efficiency and the parameters of watershed models. *Journal of Hydrology*, 320(1):62–83.

Pappenberger, F., Beven, K., Frodsham, K., Romanowicz, R., and Matgen, P. (2007). Grasping the unavoidable subjectivity in calibration of flood inundation models: a vulnerability weighted approach. *Journal of Hydrology*, 333(2):275–287.

Pauwels, V. and Lannoy, G. J. D. (2009). Ensemblebased assimilation of discharge into rainfallrunoff models: A comparison of approaches to mapping observational information to state space. *Water Resources Research*, 45(8).

Rawls, W. J., Brakensiek, D. L., and Miller, N. (1983a). Green-Ampt infiltration parameters from soils data. *Journal of Hydraulic Engineering*, 109(1):62–70.

Rawls, W. J., Brakensiek, D. L., and Soni, B. (1983b). Agricultural Management Effects on Soil Water Processes; Part I: Soil Water Retention and Green and Ampt Infiltration Parameters. *Transactions of the American Society of Agricultural Engineers*, 26(6).

Refsgaard, J. C. (1997). Validation and intercomparison of different updating procedures for real-time forecasting. *Nordic Hydrology*, 28.2:65–84.

Reichle, R. H. (2008). Data assimilation methods in the earth sciences. *Advances in Water Resources*, 31(11):1411–1418.

Rosenblueth, A. and Wiener, N. (1945). The role of models in science. *Philosophy of Science*, pages 316–321.

Rosenfeld, D., Wolff, D. B., and Amitai, E. (1994). The Window Probability Matching Method for Rainfall Measurements with Radar. *Journal of Applied Meteorology*, 33:682–693.

Rosenfeld, D., Wolff, D. B., and Atlas, D. (1993). General probability-matched relations between radar reflectivity and rain rate. *Journal of Applied Meteorology*, 32:50–50.

Rutledge, A. T. (1998). Computer programs for describing the recession of ground-water discharge and for estimating mean ground-water recharge and discharge from streamflow records. Technical report, US Department of the Interior, US Geological Survey.

Ryzhkov, A. V., Giangrande, S. E., and Schuur, T. J. (2005). Rainfall estimation with a polarimetric prototype of wsr-88d. *Journal of applied meteorology*, 44(4):502–515.

Salamon, P. and Feyen, L. (2009). Assessing parameter, precipitation, and predictive uncertainty in a distributed hydrological model using sequential data assimilation with the particle filter. *Journal of Hydrology*, 376.3:428–442.

Sánchez-Diezma, R., Sempere-Torres, D., Creutin, J., Zawadzki, I., and Delrieu, G. (2001). Factors affecting the precision of radar measurement of rain. In *An assesment from a hydrological perspective. 30th Int. Conf. on Radar Meteor., Munich (Germany)*, pages 573–575.

Seo, D.-J. and Breidenbach, J. (2002). Real-time correction of spatially nonuniform bias in radar rainfall data using rain gauge measurements. *Journal of Hydrometeorology*, 3(2):93–111.

Seo, D.-J., Breidenbach, J., and Johnson, E. (1999). Real-time estimation of mean field bias in radar rainfall data. *Journal of Hydrology*, 223(3):131–147.

Seo, D.-J., Cajina, L., Corby, R., and Howieson, T. (2009). Automatic state updating for operational streamflow forecasting via variational data assimilation. *Journal of Hydrology*, 367(3):255–275.

Seo, D.-J., Koren, V., and Cajina, N. (2003). Real-time variational assimilation of hydrologic and hydrometeorological data into operational hydrologic forecasting. *Journal of Hydrometeorology*, 4.3:627–641.

Serban, P. and Askew, A. J. (1991). *Hydrological forecasting and updating procedures*. 357-369, IAHS Publ 201.

Singh, V. P. (1995). *Computer models of watershed hydrology*. Water Resources Publications.

Singh, V. P. (1996). *Kinematic wave modeling in water resources: Surface-water hydrology*. Wiley New York.

Smith, J. A., Baeck, M. L., Meierdiercks, K. L., Miller, A. J., and Krajewski, W. F. (2007). Radar rainfall estimation for flash flood forecasting in small urban watersheds. *Advances in Water Resources*, 30(10):2087–2097.

Smith, J. A., Seo, D. J., Baeck, M. L., and Hudlow, M. D. (1996). An intercomparison study of NEXRAD precipitation estimates. *Water Resources Research*, 32(7):2035–2045.

Smith, M. B., Koren, V., Reed, S., Zhang, Z., Zhang, Y., Moreda, F., Cui, Z., Mizukami, N., Anderson, E. A., and Cosgrove, B. A. (2012). The distributed model intercomparison project-Phase 2: Motivation and design of the Oklahoma experiments. *Journal of Hydrology*, 418:3–16.

Steiner, M., Smith, J. A., Burges, S. J., Alonso, C. V., and Darden, R. W. (1999). Effect of bias adjustment and rain gauge data quality control on radar rainfall estimation. *Water Resources Research*, 35(8):2487–2503.

Todini, E. (1999). An operational decision support system for flood risk mapping, forecasting and management. *Urban Water*, 1(2):131–143.

Todini, E. (2007). Hydrological catchment modelling: Past, present and future. *Hydrology and Earth System Sciences*, 11(1):468–482.

Vieux, B. E. (1988). *Finite-element analysis of hydrological response areas using geographical information systems*. PhD thesis, Michigan State University.

Vieux, B. E. (2004a). Distributed Hydrologic Modeling using GIS. *Kluwer Academic Publishing*, 48.

Vieux, B. E. (2004b). Distributed hydrologic modelling for flood forecasting. *IAHS Publications-Series of Proceedings and Reports*, 289:1–10.

Vieux, B. E. and Bedient, P. B. (1998). Estimation of Rainfall for Flood Prediction from WSR-88D Reflectivity: A Case Study, 17-18 October 1994. *Weather and Forecasting*, 13(2):407–415.

Vieux, B. E. and Bedient, P. B. (2004). Assessing urban hydrologic prediction accuracy through event reconstruction. *Journal of Hydrology*, 299(3):217–236.

Vieux, B. E., Bralts, V. F., Segerlind, L. J., and Wallace, R. B. (1990). Finite element watershed modeling: One-dimensional elements. *Journal of Water Resources Planning and Management*, 116(6):803–819.

Vieux, B. E., Cui, Z., and Gaur, A. (2004). Evaluation of a physics-based distributed hydrologic model for flood forecasting. *Journal of Hydrology*, 298(1):155–177.

Vieux, B. E. and Gauer, N. (1994). Finite Element Modeling of Storm Water Runoff Using GRASS GIS. *ComputerAided Civil and Infrastructure Engineering*, 9(4):263–270.

Vieux, B. E., LeDimet, F., and Armand, D. (1998). Inverse problem formulation for spatially distributed river basin model calibration using the adjoint method. *EGS, Annales Geophysicae, Part II, Hydrology, Oceans and Atmosphere, Supplement II to 16*.

Vieux, B. E. and Moreda, F. G. (2003). Ordered physics-based parameter adjustment of a distributed model. *Water Science and Application*, pages 267–281.

Vieux, B. E., Park, J.-H., and Kang, B. (2009). Distributed hydrologic prediction: Sensitivity to accuracy of initial soil moisture conditions and radar rainfall input. *Journal of Hydrologic Engineering*, 14(7):671–689.

Vieux, B. E. and Vieux, J. E. (2002). Vflo: A real-time distributed hydrologic model. In *Proceedings of the 2nd Federal Interagency Hydrologic Modeling Conference*.

Vieux, B. E. and Vieux, J. E. (2005a). Rainfall accuracy considerations using radar and rain gauge networks for rainfall-runoff monitoring. *Effective modeling of urban water systems, Monograph*, 13.

Vieux, B. E. and Vieux, J. E. (2005b). Statistical evaluation of a radar rainfall system for sewer system management. *Atmospheric research*, 77(1):322–336.

Vieux, B. E., Vieux, J. E., Chen, C., and Howard, K. W. (2003). Operational deployment of a physics-based distributed rainfall-runoff model for flood forecasting in Taiwan. *International Association of Hydrological Sciences, Publication*, 282:251–257.

Wagener, T., Wheater, H. S., and Gupta, H. V. (2004). *Rainfall-runoff modelling in gauged and ungauged catchments*. Imperial College Pr.

Weerts, A. H. and BECKERS, J. (2009). 2009. 06.01 Uncertainty Framework for Operational and Storm Surge Forecasting, Deltares / FC2015 Research Report, 1200379.001.

Weerts, A. H. and Serafy, G. Y. E. (2006). Particle filtering and ensemble kalman filtering for state updating with hydrological conceptual rainfall-runoff models. *Water Resources Research*, 42(9).

White, L. W., Vieux, B. E., and Armand, D. (2002). Surface flow model: inverse problems and predictions. *Advances in water resources*, 25(3):317–324.

White, L. W., Vieux, B. E., Armand, D., and LeDimet, F. X. (2003). Estimation of optimal parameters for a surface hydrology model. *Advances in Water Resources*, 26(3):337–348.

Wigmosta, M. S. and Burges, S. J. (1997). An adaptive modeling and monitoring approach to describe the hydrologic behavior of small catchments. *Journal of Hydrology*, 202(1-4):48–77.

Willems, P. (2002). Stochastic description of the rainfall input errors in lumped hydrological models. *Stochastic environmental research and risk assessment*, 15(2):132–152.

Wilson, J. W. and Brandes, E. A. (1979). Radar measurement of rainfall a summary. *Bulletin of the American Meteorological Society*, 60(9):1048–1058.

Winchell, M., Gupta, H. V., and Sorooshian, S. (1998). On the simulation of infiltration-and saturation-excess runoff using radar-based rainfall estimates: Effects of algorithm uncertainty and pixel aggregation. *Water Resources Research*, 34(10):2655–2670.

Woolhiser, D. A. and Liggett, J. A. (1967). Unsteady, one-dimensional flow over a planethe rising hydrograph. *Water Resources Research*, 3(3):753–771.

Yen, B. C. (1995). Criteria for evaluation of watershed models. *Journal of Irrigation and Drainage Engineering*, 121(1):130–132.

Young, C. B., Bradley, A. A., Krajewski, W. F., Kruger, A., and Morrissey, M. L. (2000). Evaluating NEXRAD multisensor precipitation estimates for operational hydrologic forecasting. *Journal of Hydrometeorology*, 1(3):241–254.

Appendix A

Appendix

A.1 Forward Sensitivity Method Derivation for Simple Model

The following derivation shows the structure of the forward sensitivities with respect to roughness at each grid point using a simple 5 grid point plane model. The 5-point grid is shown in the following figure with the depth of flow indicated in blue. The cross sectional area, A, is the depth of flow, h, multiplied by the width, w, of a grid point. The conservation equation that is solved by the kinematic wave model,

$$\frac{\partial A}{\partial t} + \frac{\partial Q}{\partial x} = rw \tag{A.1}$$

where A is cross sectional flow area, Q is the flow rate, r is the rainfall rate, and w is the plane width. The boundary condition is $A(0,t) = 0$, and initial condition is $A(x,0) = 0$. Manning's equation is a simplified form of the momentum equation that relates discharge, Q, to cross sectional flow area, A.

$$Q = VA = \frac{G}{\eta}A^m \tag{A.2}$$

where $m = \frac{5}{3}$ for Manning's equation.

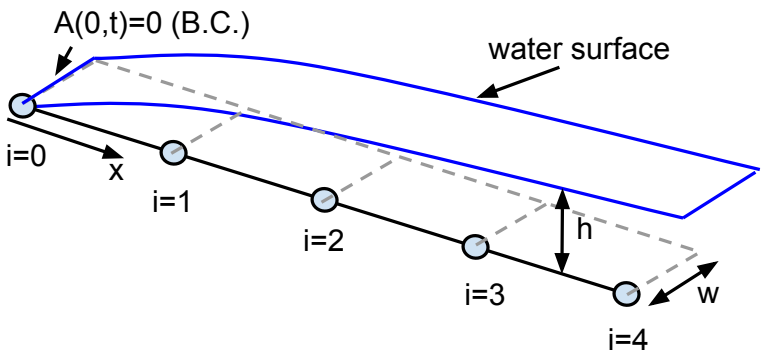

Figure A.1: Grid for 5-point example

The kinematic wave equation is discretized using the forward time backward difference finite difference form is,

$$A_{i,k+1} = A_{i,k} - \frac{\Delta t}{\Delta x}\left(\frac{G_i}{\eta_i}A^m_{i,k} - \frac{G_{i-1}}{\eta_{i-1}}A^m_{i-1,k}\right) + r_{i,k+1}w_i\Delta t \tag{A.3}$$

For $i = 1$,

$$A_{1,k+1} = A_{1,k} - \frac{\Delta t}{\Delta x}\left(\frac{G_1}{\eta_1}A^m_{1,k} - \frac{G_0}{\eta_0}A^m_{0,k}\right) + r_{1,k+1}w_1\Delta t \tag{A.4}$$

With the boundary condition $A(0,t) = 0$ therefore $A_{0,k} = 0$ and eq. A.4 reduces to,

$$A_{1,k+1} = A_{1,k} - \frac{\Delta t}{\Delta x}\left(\frac{G_1}{\eta_1}A^m_{1,k}\right) + r_{1,k+1}w_1\Delta t \tag{A.5}$$

Next, we will calculate the forward sensitivity, $\frac{\partial A}{\partial \eta}$ for A_1 with respect to the roughness at each grid point, j. For $i = 1$ and $j = 0$, $\frac{\partial A_{1,k+1}}{\partial \eta_0} = 0$ because η_0 has no influence on $A_{1,k+1}$ due to the boundary condition of $A(0,t) = 0$.

For $i = 1$ and $j = 1$

$$\frac{\partial A_{1,k+1}}{\partial \eta_1} = \frac{\partial A_{1,k}}{\partial \eta_1} - \frac{\Delta t}{\Delta x}\left(\frac{G_1}{\eta_1} m A_{1,k}^{m-1} \frac{\partial A_{1,k}}{\partial \eta_1} - \frac{G_1}{\eta_1^2} A_{1,k}^m\right) \tag{A.6}$$

Or

$$\frac{\partial A_{1,k+1}}{\partial \eta_1} = \left(1 - \frac{\Delta t}{\Delta x}\frac{G_1}{\eta_1} m A_{1,k}^{m-1}\right)\frac{\partial A_{1,k}}{\partial \eta_1} + \frac{\Delta t}{\Delta x}\frac{G_1}{\eta_1^2} A_{1,k}^m \tag{A.7}$$

For $i = 1$ and $j > 1$

$$\frac{\partial A_{1,k+1}}{\partial \eta_j} = 0 \tag{A.8}$$

because η_j has no influence on $A_{1,k+1}$

For $i = 2$

$$A_{2,k+1} = A_{2,k} - \frac{\Delta t}{\Delta x}\left(\frac{G_2}{\eta_2} A_{2,k}^m - \frac{G_1}{\eta_1} A_{1,k}^m\right) + r_{2,k+1} w_2 \Delta t \tag{A.9}$$

For $i = 2$ and $j = 0$

$$\frac{\partial A_{2,k+1}}{\partial \eta_0} = 0 \tag{A.10}$$

because η_0 has no influence on $A_{2,k+1}$ due to boundary condition of $A(0,t) = 0$

For $i = 2$ and $j = 1$

$$\begin{aligned}\frac{\partial A_{2,k+1}}{\partial \eta_1} = \frac{\partial A_{2,k}}{\partial \eta_1} - \frac{\Delta t}{\Delta x}\Big(&\frac{G_2}{\eta_2} m A_{2,k}^{m-1}\frac{\partial A_{2,k}}{\partial \eta_1} - \frac{G_1}{\eta_1} m A_{1,k}^{m-1}\frac{\partial A_{1,k}}{\partial \eta_1} \\ &+ \frac{G_1}{\eta_1 2} A_{1,k}^m\Big)\end{aligned} \tag{A.11}$$

Or

$$\frac{\partial A_{2,k+1}}{\partial \eta_1} = \begin{bmatrix} \frac{\Delta t}{\Delta x}\frac{G_1}{\eta_1} m A_{1,k}^{m-1} & 1 - \frac{\Delta t}{\Delta x}\frac{G_2}{\eta_2} m A_{2,k}^{m-1} \end{bmatrix} \begin{bmatrix} \frac{\partial A_{1,k}}{\partial \eta_1} \\ \frac{\partial A_{2,k}}{\partial \eta_1} \end{bmatrix} - \frac{\Delta t}{\Delta x}\frac{G_1}{\eta_1} 2 A_{1,k}^{m} \tag{A.12}$$

For $i = 2$ and $j = 2$

$$\frac{\partial A_{2,k+1}}{\partial \eta_2} = \frac{\partial A_{2,k}}{\partial \eta_2} - \frac{\Delta t}{\Delta x}\Big(\frac{G_2}{\eta_2} m A_{2,k}^{m-1}\frac{\partial A_{2,k}}{\partial \eta_2} - \frac{G_2}{\eta_2^2} A_{2,k}^{m} - \frac{G_1}{\eta_1} m A_{1,k}^{m-1}\frac{\partial A_{1,k}}{\partial \eta_2}\Big) \tag{A.13}$$

or

$$\frac{\partial A_{2,k+1}}{\partial \eta_2} = \frac{\partial A_{2,k}}{\partial \eta_2} - \frac{\Delta t}{\Delta x}\left(\frac{G_2}{\eta_2} m A_{2,k}^{m-1}\frac{\partial A_{2,k}}{\partial \eta_2} - \frac{G_2}{\eta_2^2} A_{2,k}^{m}\right) \tag{A.14}$$

or

$$\frac{\partial A_{2,k+1}}{\partial \eta_2} = \left[1 - \frac{\Delta t}{\Delta x}\frac{G_2}{\eta_2} m A_{2,k}^{m-1}\right]\left[\frac{\partial A_{2,k}}{\partial \eta_2}\right] + \frac{\Delta t}{\Delta x}\frac{G_2}{\eta_2^2} A_{2,k}^{m} \tag{A.15}$$

For $i = 2$ and $j > 2$

$$\frac{\partial A_{2,k+1}}{\partial \eta_j} = 0 \tag{A.16}$$

because η_j has no influence on $A_{2,k+1}$.

For $i = 3$

$$A_{3,k+1} = A_{3,k} - \frac{\Delta t}{\Delta x}\left(\frac{G_3}{\eta_3} A_{3,k}^{m} - \frac{G_2}{\eta_2} A_{2,k}^{m}\right) + r_{3,k+1} w_3 \Delta t \tag{A.17}$$

For $i = 3$ and $j = 0$

$$\frac{\partial A_{3,k+1}}{\partial \eta_0} = 0 \tag{A.18}$$

because η_0 has no influence on $A_{3,k+1}$ due to boundary condition of $A(0,t) = 0$.

For $i = 3$ and $j = 1$

$$\frac{\partial A_{3,k+1}}{\partial \eta_1} = \frac{\partial A_{3,k}}{\partial \eta_1} - \frac{\Delta t}{\Delta x}\left(\frac{G_3}{\eta_3} m A_{3,k}^{m-1} \frac{\partial A_{3,k}}{\partial \eta_1} - \frac{G_2}{\eta_2} m A_{2,k}^{m-1} \frac{\partial A_{2,k}}{\partial \eta_1}\right) \tag{A.19}$$

or

$$\frac{\partial A_{2,k+1}}{\partial \eta_1} = \begin{bmatrix} 0 & \frac{\Delta t}{\Delta x}\frac{G_2}{\eta_2} m A_{2,k}^{m-1} & 1 - \frac{\Delta t}{\Delta x}\frac{G_3}{\eta_3} m A_{3,k}^{m-1} \end{bmatrix} \begin{bmatrix} \frac{\partial A_{1,k}}{\partial \eta_1} \\ \frac{\partial A_{2,k}}{\partial \eta_1} \\ \frac{\partial A_{3,k}}{\partial \eta_1} \end{bmatrix} \tag{A.20}$$

For $i = 3$ and $j = 2$

$$\frac{\partial A_{3,k+1}}{\partial \eta_2} = \frac{\partial A_{3,k}}{\partial \eta_2} - \frac{\Delta t}{\Delta x}\Big(\frac{G_3}{\eta_3} m A_{3,k}^{m-1} \frac{\partial A_{3,k}}{\partial \eta_2} - \frac{G_2}{\eta_2} m A_{2,k}^{m-1} \frac{\partial A_{2,k}}{\partial \eta_2} + \frac{G_2}{\eta_2^2} A_{2,k}^{m}\Big) \tag{A.21}$$

or in matrix form

$$\frac{\partial A_{3,k+1}}{\partial \eta_2} = \begin{bmatrix} 0 & \frac{\Delta t}{\Delta x}\frac{G_2}{\eta_2} m A_{2,k}^{m-1} & 1 - \frac{\Delta t}{\Delta x}\frac{G_3}{\eta_3} m A_{3,k}^{m-1} \end{bmatrix} \begin{bmatrix} \frac{\partial A_{1,k}}{\partial \eta_2} \\ \frac{\partial A_{2,k}}{\partial \eta_2} \\ \frac{\partial A_{3,k}}{\partial \eta_2} \end{bmatrix} - \frac{\Delta t}{\Delta x}\frac{G_2}{\eta_2^2} A_{2,k}^{m} \tag{A.22}$$

For $i = 3$ and $j = 3$

$$\frac{\partial A_{3,k+1}}{\partial \eta_3} = \begin{bmatrix} 0 & \frac{\Delta t}{\Delta x}\frac{G_2}{\eta_2} m A_{2,k}^{m-1} & 1 - \frac{\Delta t}{\Delta x}\frac{G_3}{\eta_3} m A_{3,k}^{m-1} \end{bmatrix} \begin{bmatrix} \frac{\partial A_{1,k}}{\partial \eta_3} \\ \frac{\partial A_{2,k}}{\partial \eta_3} \\ \frac{\partial A_{3,k}}{\partial \eta_3} \end{bmatrix} + \frac{\Delta t}{\Delta x}\frac{G_3}{\eta_3^2} A_{3,k}^{m} \tag{A.23}$$

For $i = 3$ and $j > 3$

$$\frac{\partial A_{3,k+1}}{\partial \eta_j} = 0 \tag{A.24}$$

because η_j has no influence on $A_{3,k+1} = 0$.

For $i = 4$

$$A_{4,k+1} = A_{4,k} - \frac{\Delta t}{\Delta x}\left(\frac{G_4}{\eta_4}A_{4,k}^m - \frac{G_3}{\eta_3}A_{3,k}^m\right) + r_{4,k+1}w_4\Delta t \tag{A.25}$$

For $i = 4$ and $j = 0$

$$\frac{\partial A_{4,k+1}}{\partial \eta_0} = 0 \tag{A.26}$$

because η_0 has no influence on $A_{4,k+1}$ due to boundary condition of $A(0,t) = 0$.

For $i = 4$ and $j = 1$

$$\frac{\partial A_{4,k+1}}{\partial \eta_1} = \begin{bmatrix} 0 & 0 & \frac{\Delta t}{\Delta x}\frac{G_3}{\eta_3}mA_{3,k}^{m-1} & 1 - \frac{\Delta t}{\Delta x}\frac{G_4}{\eta_4}mA_{4,k}^{m-1} \end{bmatrix} \begin{bmatrix} \frac{\partial A_{1,k}}{\partial \eta_1} \\ \frac{\partial A_{2,k}}{\partial \eta_1} \\ \frac{\partial A_{3,k}}{\partial \eta_1} \\ \frac{\partial A_{4,k}}{\partial \eta_1} \end{bmatrix} \tag{A.27}$$

For $i = 4$ and $j = 2$

$$\frac{\partial A_{4,k+1}}{\partial \eta_2} = \begin{bmatrix} 0 & 0 & \frac{\Delta t}{\Delta x}\frac{G_3}{\eta_3}mA_{3,k}^{m-1} & 1 - \frac{\Delta t}{\Delta x}\frac{G_4}{\eta_4}mA_{4,k}^{m-1} \end{bmatrix} \begin{bmatrix} \frac{\partial A_{1,k}}{\partial \eta_2} \\ \frac{\partial A_{2,k}}{\partial \eta_2} \\ \frac{\partial A_{3,k}}{\partial \eta_2} \\ \frac{\partial A_{4,k}}{\partial \eta_2} \end{bmatrix} \tag{A.28}$$

For $i = 4$ and $j = 3$

$$\frac{\partial A_{4,k+1}}{\partial \eta_3} = \begin{bmatrix} 0 & 0 & \frac{\Delta t}{\Delta x}\frac{G_3}{\eta_3} m A_{3,k}^{m-1} & 1 - \frac{\Delta t}{\Delta x}\frac{G_4}{\eta_4} m A_{4,k}^{m-1} \end{bmatrix} \begin{bmatrix} \frac{\partial A_{1,k}}{\partial \eta_3} \\ \frac{\partial A_{2,k}}{\partial \eta_3} \\ \frac{\partial A_{3,k}}{\partial \eta_3} \\ \frac{\partial A_{4,k}}{\partial \eta_3} \end{bmatrix} - \frac{\Delta t}{\Delta x}\frac{G_3}{\eta_3^2} A_{3,k}^m \tag{A.29}$$

For $i = 4$ and $j = 4$

$$\frac{\partial A_{4,k+1}}{\partial \eta_4} = \begin{bmatrix} 0 & 0 & \frac{\Delta t}{\Delta x}\frac{G_3}{\eta_3} m A_{3,k}^{m-1} & 1 - \frac{\Delta t}{\Delta x}\frac{G_4}{\eta_4} m A_{4,k}^{m-1} \end{bmatrix} \begin{bmatrix} \frac{\partial A_{1,k}}{\partial \eta_4} \\ \frac{\partial A_{2,k}}{\partial \eta_4} \\ \frac{\partial A_{3,k}}{\partial \eta_4} \\ \frac{\partial A_{4,k}}{\partial \eta_4} \end{bmatrix} + \frac{\Delta t}{\Delta x}\frac{G_4}{\eta_4^2} A_{4,k}^m \tag{A.30}$$

Generalization of matrix form $D_\eta(A_{k+1}) = D_A(M_k)D_\eta(A_k) + D_\eta(M_k)$ where,

$$D_A(M_k) = \begin{bmatrix} 0 & 0 & 0 & 0 & 0 \\ 0 & 1 & 0 & 0 & 0 \\ 0 & 0 & 1 & 0 & 0 \\ 0 & 0 & 0 & 1 & 0 \\ 0 & 0 & 0 & 0 & 1 \end{bmatrix}$$

$$- \frac{\Delta t}{\Delta x} m \begin{bmatrix} \frac{G_0}{\eta_0} & 0 & 0 & 0 & 0 \\ -\frac{G_0}{\eta_0} & \frac{G_1}{\eta_1} & 0 & 0 & 0 \\ 0 & -\frac{G_1}{\eta_1} & \frac{G_2}{\eta_2} & 0 & 0 \\ 0 & 0 & -\frac{G_2}{\eta_2} & \frac{G_3}{\eta_3} & 0 \\ 0 & 0 & 0 & -\frac{G_3}{\eta_3} & \frac{G_4}{\eta_4} \end{bmatrix} \circ \begin{bmatrix} A_0^{m-1} & 0 & 0 & 0 & 0 \\ A_0^{m-1} & A_1^{m-1} & 0 & 0 & 0 \\ 0 & A_1^{m-1} & A_2^{m-1} & 0 & 0 \\ 0 & 0 & A_2^{m-1} & A_3^{m-1} & 0 \\ 0 & 0 & 0 & A_3^{m-1} & A_4^{m-1} \end{bmatrix}_k \tag{A.31}$$

$$D_\eta(A_k) = \begin{bmatrix} \frac{\partial A_0}{\partial \eta_0} & \frac{\partial A_0}{\partial \eta_1} & \frac{\partial A_0}{\partial \eta_2} & \frac{\partial A_0}{\partial \eta_3} & \frac{\partial A_0}{\partial \eta_4} \\ \frac{\partial A_1}{\partial \eta_0} & \frac{\partial A_1}{\partial \eta_1} & \frac{\partial A_1}{\partial \eta_2} & \frac{\partial A_1}{\partial \eta_3} & \frac{\partial A_1}{\partial \eta_4} \\ \frac{\partial A_2}{\partial \eta_0} & \frac{\partial A_2}{\partial \eta_1} & \frac{\partial A_2}{\partial \eta_2} & \frac{\partial A_2}{\partial \eta_3} & \frac{\partial A_2}{\partial \eta_4} \\ \frac{\partial A_3}{\partial \eta_0} & \frac{\partial A_3}{\partial \eta_1} & \frac{\partial A_3}{\partial \eta_2} & \frac{\partial A_3}{\partial \eta_3} & \frac{\partial A_3}{\partial \eta_4} \\ \frac{\partial A_4}{\partial \eta_0} & \frac{\partial A_4}{\partial \eta_1} & \frac{\partial A_4}{\partial \eta_2} & \frac{\partial A_4}{\partial \eta_3} & \frac{\partial A_4}{\partial \eta_4} \end{bmatrix}_k = \begin{bmatrix} \frac{\partial A_0}{\partial \eta_0} & 0 & 0 & 0 & 0 \\ \frac{\partial A_1}{\partial \eta_0} & \frac{\partial A_1}{\partial \eta_1} & 0 & 0 & 0 \\ \frac{\partial A_2}{\partial \eta_0} & \frac{\partial A_2}{\partial \eta_1} & \frac{\partial A_2}{\partial \eta_2} & 0 & 0 \\ \frac{\partial A_3}{\partial \eta_0} & \frac{\partial A_3}{\partial \eta_1} & \frac{\partial A_3}{\partial \eta_2} & \frac{\partial A_3}{\partial \eta_3} & 0 \\ \frac{\partial A_4}{\partial \eta_0} & \frac{\partial A_4}{\partial \eta_1} & \frac{\partial A_4}{\partial \eta_2} & \frac{\partial A_4}{\partial \eta_3} & \frac{\partial A_4}{\partial \eta_4} \end{bmatrix}_k \tag{A.32}$$

$$D_\eta(M_k) = \frac{\Delta t}{\Delta x} \begin{bmatrix} \frac{G_0}{{\eta_0}^2} & 0 & 0 & 0 & 0 \\ -\frac{G_0}{{\eta_0}^2} & \frac{G_1}{{\eta_1}^2} & 0 & 0 & 0 \\ 0 & -\frac{G_1}{{\eta_1}^2} & \frac{G_2}{{\eta_2}^2} & 0 & 0 \\ 0 & 0 & -\frac{G_2}{{\eta_2}^2} & \frac{G_3}{{\eta_3}^2} & 0 \\ 0 & 0 & 0 & -\frac{G_3}{{\eta_3}^2} & \frac{G_4}{{\eta_4}^2} \end{bmatrix} \circ \begin{bmatrix} A_0^m & 0 & 0 & 0 & 0 \\ A_0^m & A_1^m & 0 & 0 & 0 \\ 0 & A_1^m & A_2^m & 0 & 0 \\ 0 & 0 & A_2^m & A_3^m & 0 \\ 0 & 0 & 0 & A_3^m & A_4^m \end{bmatrix}_k \tag{A.33}$$